Accretion Cycles, Structural Evolution, and Thrust Activity in Accretionary Wedges With Various Décollement Configurations: Insights From Sandbox Analog Modeling

Atsushi Noda, Fabien Graveleau, Cesar Witt, Frank Chanier, Bruno Vendeville

To cite this version:

Atsushi Noda, Fabien Graveleau, Cesar Witt, Frank Chanier, Bruno Vendeville. Accretion Cycles, Structural Evolution, and Thrust Activity in Accretionary Wedges With Various Décollement Configurations: Insights From Sandbox Analog Modeling. Journal of Geophysical Research : Solid Earth, 2023, 128 (12), 10.1029/2023JB027131 . hal-04332072

HAL Id: hal-04332072
https://hal.science/hal-04332072

Submitted on 11 Dec 2023

Accretion cycle, structural evolution, and thrust activity in accretionary wedges with various décollement configurations: Insights from sandbox analog modeling

Atsushi Noda[1,2], **Fabien Graveleau**[2], **Cesar Witt**[2], **Frank Chanier**[2], **and Bruno Vendeville**[2*]

[1]Geological Survey of Japan, National Institute of Advanced Industrial Science and Technology (AIST), Central 7, Higashi 1-1-1, Tsukuba, Ibaraki 305-8567, Japan

[2]University of Lille, CNRS, ULCO, IRD, UMR 8187, Laboratory of Oceanology and Geosciences (LOG), Lille, 59000, France

Key Points:

- Interbedded weak layer reduced the effective internal friction angle of the wedge, which weakened the wedge and made a dense fault network
- Subduction of a frictional barrier in the basal decollement lasted the out-of-sequence activity and facilitated the sediment underplating
- Our results can contribute to understanding of the growth processes, architectural evolution, and kinematics in natural accretionary wedges

---

[*] Deceased.

Corresponding author: Atsushi Noda, `a.noda@aist.go.jp`

Abstract

The architecture (geometry, fault network, stacking pattern of accreted thrust sheets, etc.) is an important component of accretionary wedges that have developed through the subduction zone processes. However, it remains challenging to constrain the processes of the architectural evolution in natural accretionary wedges over the geological timescale. In this study, we undertook sandbox analogue modeling with quantitative analysis of the wedge geometry and the digital image correlation-based kinematics to delineate the wedge growth process under four basic types of the décollement settings. In the case of continuous single décollement model, the episodic frontal accretion with a constant cycle (i.e., accretion cycle) was dominant where degree of coupling between the wedge base and the plate interface may rely on the relative strengths of the wedge and the detachment, and the wedge progressively reached its critical state through multiple accretion cycles. The interbedded décollement layer facilitated the wedge segmentation and the rearrangement of the internal fault network, which weakened the wedge strength. A combination of a detachable high-friction patch in the basal décollement and the continuous interbedded weak layer enabled underplating of the underthrusted sediment beneath the inner wedge with a low-angle, long-lived, deeply rooted forethrust and multiple cycles of frontal accretions by using shallowly rooted, short-lived forethrusts at the deformation front. Our findings suggest that the décollement configuration is a key factor on accretion processes including the accretion cycle, fault network, and wedge strength in the time scale of $\sim 10^5$ years of natural accretionary systems.

Plain Language Summary

Accretionary wedges are one of the key components of plate subduction zones. In this study, we tested variations of the wedge deformation during its growth to improve our knowledge of how accretionary wedges grow. Here, we conducted sandbox analogue experiments to characterize the wedge geometry and spatiotemporal changes in deformation during the accretionary wedge growth by using simplified models with various conditions (single/double or continuous/discontinuous) of weak layers in subducting sediment. The results show that the wedge growth was basically achieved by repetition of a frontal accretion cycle, but the details of the cycle depend on condition of the weak layer. For example, in the model with a discontinuous basal weak layer and a continuous interbedded weak layer, basal accretion of the subducted sediment beneath the inner part of the wedge were promoted by a low-angle, long-lived, deeply rooted underthrusting and also multiple frontal accretion is made by shallowly rooted, short-lived frontal thrusts branched from the interbedded weak layer. Our findings suggest that the conditions of the weak layers in subducting sediment change the accretion process, the strain distribution, and fault activity in the time scale of $\sim 10^5$ years of natural accretionary wedges.

1 Introduction

Accretionary wedges are deformed sedimentary bodies which develop on the forearc side of subduction zones. Recent geophysical surveys have revealed details of the geological and geophysical structures in the accretionary wedge and at the plate boundary of modern subduction zones (Arnulf et al., 2021, 2022; Egbert et al., 2022; Kirkpatrick et al., 2020), including P-wave velocity structure (Han et al., 2017), magnetotelluric images of electrical resistivity (Chesley et al., 2021), teleseismic profiles (Calvert et al., 2011), and the slip tendency (Hashimoto et al., 2022). On the other hand, GPS/GNSS observations also record the interseismic coupling or slip rate at the subduction interface on timescales of 10^0 to 10^2 yr (Lindsey et al., 2021; Lv et al., 2022; Métois et al., 2012; Newton & Thomas, 2020; Wallace et al., 2012; Weiss et al., 2015; Yáñez-Cuadra et al., 2022; Yokota et al., 2016), which have successfully captured present-day snapshots of the stress and strain state in accretionary wedges. However, the modern conditions of these wedges (i.e., rigidity, heterogeneity, strain state) may be affected by their architecture (i.e., wedge geometry, fault network, and stacking pattern of accreted thrust sheets) that has developed through long-term interactions between the upper and lower plates in subduction zones. Therefore, the architecture of accretionary wedges is important factor to understand the recent snapshots of geological and geophysical structures in natural subduction zones.

Based on the long-term equilibrium geometry of accretionary wedges formed in response to accretion, the critical taper theory (Dahlen, 1990; Davis et al., 1983) has been applied to many natural accretionary wedges in foreland/forearc thrust belts to link the effective frictional properties to the surface topography and basal slope of the detachment (Cubas et al., 2022; Kukowski et al., 2010; Lallemand et al., 1994; Maksymowicz, 2015; Schwarze & Kukowski, 2022). The key physical assumption is that the wedge can undergo internal failure in order to maintain its critical mechanical state. However, natural examples of accretionary wedges are not uniformly deformed and they exhibit a wide range of architectures (Figure 1). For example, the Colombian–Caribbean margin (Rodríguez et al., 2021) is dominated by frontal accretion of thick thrust sheets in a piggy-back style where the Paleocene shale acts as a basal detachment (single-décollement wedge in Figure 1a). This type can be seen at the Sumatra (Singh et al., 2011) or Colombian–Caribbean (Mantilla-Pimiento et al., 2009; Rodríguez et al., 2021) margins. On the other hand, some of the accretionary wedges are characterized by a combination of frontal and basal accretions, which are related with landward stepping down of the décollement level at the bottom of the wedge (double-décollement wedge in Figure 1b). In this case, the interbedded weak layer(s) in the incoming sediment, such as clay mineral-rich horizons, can work as a intermediate décollement. The examples of this type can be seen in the Makran (Burg, 2018; Haberland et al., 2020; C. Kopp et al., 2000; Parvaiz et al., 2022; Schlüter et al., 2002; Smith et al., 2012), Barbados (Behrmann et al., 1988; Deng & Underwood, 2001; Dileonardo et al., 2002; J. C. Moore et al., 1998), Cascadia (Han et al., 2017), Nankai (Kopf, 2013), and Alaskan (Frederik et al., 2020; Gulick et al., 2015; Reece et al., 2011) margins.

In addition, topographic features on the subducting oceanic plate, such as seamounts, ridges, horsts, and grabens, may affect the strength and continuity of the basal décollement, and modify the internal structures and stacking patterns of accreted sediments (Collot et al., 2001; Pedley et al., 2010; Ruh, 2016) (discontinuous décollement wedge in Figure 1c). The décollement heterogeneity may also cause geometrical or kinematic segmentation in the wedge (Collot et al., 2008; Cook et al., 2014; Smith et al., 2012; Wang & Hu, 2006). For example, a large-scale out-of-sequence thrust is recognized as "mega-splay fault" that separates relatively rigid inner wedge and deformable outer wedge (Bangs et al., 2009; H. Kopp & Kukowski, 2003; Krabbenhoeft et al., 2021; G. F. Moore et al., 2007; Strasser et al., 2009) (discontinuous multiple-décollement wedge in Figure 1d). In the Nankai Trough, southwestern Japan, the interbedded clay-rich layer between the upper sandy turbidite unit and lower ash-bearing mud unit in the incoming sediment layer is weak, and can act as a décollement to propagate deformation seaward (Kopf, 2013).

All these examples show us that the décollement settings (heterogeneity or complexity at the plate interface and in the subducting sediment) are important for developing the architecture of accretionary wedges. However, it remains challenging to explain various processes related to the architectural evolution in natural accretionary wedges over the geological timescale. The key questions are how the décollement settings, including the number (i.e., single/double) and the continuity (i.e., continuous/discontinuous) of the décollement layer(s), affect (1) the architecture (i.e., fault network, stacking patterns of the thrust sheets) of accretionary wedges and (2) the spatio-temporal changes of the strain state and the thrust activities in the wedges during their growth. Our approach is an analog sandbox experiment involving quantitative geometric and digital image correlation (DIC)-based kinematic analysis of the experimental data. Answering to these questions can contribute to understand the present-day snapshots of natural accretionary wedges and subduction zones.

2 Previous modeling studies of accretionary wedges

Previous modeling studies of accretionary wedges include physical analog modeling (e.g., Bigi et al., 2010; Mulugeta & Koyi, 1992; Ghosh et al., 2020; Gutscher et al., 1996; Koyi, 1995; Lohrmann et al., 2003; Roy et al., 2020; Saha et al., 2016), work optimization or mechanical approaches to predict the wedge geometry and faulting (Burbidge & Braun, 2002; Cooke & Madden, 2014; Cubas et al., 2008; Del Castello & Cooke, 2007; Gutscher et al., 1998a; Hardy et al., 1998; Leroy & Maillot, 2016; Maillot & Koyi, 2006; Mary et al., 2013; McBeck et al., 2017; Platt, 1986, 1988; Souloumiac et al., 2010, 2009; Yagupsky et al., 2014), and numerical simulations (del Castillo et al., 2021; Ito & Moore, 2021; Naylor & Sinclair, 2007; Ruh et al., 2012; Ruh, 2020; Simpson, 2010, 2011; Stockmal et al., 2007). Early analog modeling studies revealed that the accretion process was episodic rather than steady (Mulugeta & Koyi, 1992), meaning the wedge did not keep its original shape during the growth (i.e., self-similar growth) but oscillated the surface slope angle of the wedge as a new material was accreted at the toe and then compressed inward.

Early studies also indicated that the process of accretion was characterized by a combination of initiation of a new frontal thrust at the deformation front and backward rotation of older pre-existing thrust sheets in the wedge (Koyi, 1995). Gutscher et al. (1998a) called the episodic accretion as “accretionary cycle” or “cyclical accretion” which comprised alternating the first phase of frontal accretion of a short imbricate thrust slice and the second phase of underthrusting of a long, undeformed sedimentary sheet. In the first phase, the surface slope was decreased by an increase in wedge length due to initiation of a new frontal thrust seaward at the toe. Whereas in the second phase, the surface slope was increased up to the critical taper angle by thickening and narrowing the wedge due to progressive compression in association with reactivation of the pre-existing thrusts. Hoffmann-Rothe et al. (2004) also classified the episodic behaviour of an accretionary cycle into (1) the thrust-initiation phase in which a new forethrust and pop-up structure were formed at the deformation front and (2) the underthrusting phase in which trench-fill sediment was subducted beneath the accretionary wedge. The underthrusting phase started when the deformation front segmented into the upper and lower parts and the lower part began to be underthrusted beneath the upper part (Hoffmann-Rothe et al., 2004).

In the late 2000s, based on advances in DIC techniques, the accretion cycle was examined in terms of the strain-dependent deformation similar to natural deformation processes in brittle rocks (Adam et al., 2005). They showed that (1) accumulation of pre-failure strain caused strain hardening in the wedge and then (2) strain localization by initiating the new frontal thrust led to post-failure strain softening. The strain hardening and softening were accompanied by a compaction–decompaction cycle of the material, which controled the evolution of the frictional strength during progressive deformation (Adam et al., 2005). Hoth et al. (2007) also applied the DIC technique to their sandbox experiments and identified three phases (thrust initiation, underthrusting, and reactivation) in the accretion cycle, depending on the location, timing, and magnitude of deformation within thrust wedges. Dotare et al. (2016) further proposed four stages, which include stage 0 (concentration of all deformation onto the existing thrusts in the wedge), stage 1 (propagation of deformation ahead of the deformation front), stage 2 (strain localization within the diffused deformation zone in front of the wedge and reduction of activity on the existing thrusts), and stage 3 (activation of a new frontal thrust and cessation of activity on the existing thrusts). Ritter et al. (2018) indicated that the strain localization phase (stage 2 of Dotare et al., 2016) was associated with the compaction and hardening of the wedge and a new frontal thrust appeared ahead of the deformation front after the wedge was compacted and hardened enough (stage 3 of Dotare et al., 2016) based on their force measurements.

In addition to the basal décollement at the plate interface, the presence of an intermediate weak layer (i.e., pelagic or clayey sediment with a low effective friction coefficient in nature) in the incoming sediment (i.e., trench-fill sediment) can enhance underthrusting in the accretion cycle (Bonnet et al., 2007; Dal Zilio et al., 2020; Konstantinovskaia & Malavieille, 2005; Konstantinovskaya & Malavieille, 2011; Malavieille et al., 2019; Pajang et al., 2022; Perrin et al., 2013; Ruh et al., 2012; Ruh, 2020; Stockmal et al., 2007), which makes a different architecture from a single décollement case in nature and laboratory (Farzipour-Saein & Koyi, 2016; Ghanadian et al., 2017; Massoli et al., 2006; Meng & Hodgetts, 2019; C. Sun et al., 2021; Zhang et al., 2019). For example, decoupling of the incoming sediment at the intermediate décollement horizon generates two sets of structures with different geometrical characteristics in the models (Farzipour-Saein & Koyi, 2016; Massoli et al., 2006).

In terms of the continuity of the décollement layer, previous studies have investigated the subduction of a rough plate interface or a high-friction patch interrupting the basal décollement layer (Bangs et al., 2004, 2006; Dominguez et al., 1998, 2000; Koge et al., 2018; Kukowski et al., 1994; Lallemand & Le Pichon, 1987; Lallemand et al., 1992, 1994; Miyakawa et al., 2022; Morgan & Bangs, 2017; Noda et al., 2020; Okuma et al., 2022; Ruh et al., 2013; T. Sun et al., 2020). When a high-friction patch on the plate interface works as a barrier to stress transmission within the basal décollement, the wedge deformation includes indentation or slope failure on the surface topography, widening the brittle damaged zone at the plate interface, or promotion of underthrusting of the subducting sediments beneath the wedge (Dominguez et al., 2000; Miyakawa et al., 2022; Morgan & Bangs, 2017; Noda et al., 2020; Okuma et al., 2022; Wang & Bilek, 2011).

We learned from these previous studies that the accretion was a cyclic process including frontal accretion and underthrusting, and the décollement configurations affected the wedge architecture. However, our knowledge is still limited about how variation of the décollement conditions control the accretion cycle and the spatio-temporal changes of the kinematics on the wedge growth, especially in the cases of multiple or discontinuous décollement settings.

3 Methods

3.1 Model types

As we introduced in the Introduction section, there are several variations of décollement configurations in natural accretionary wedges (Figure 1). We here assumed that the typical configurations of the décollement settings could be classified into 4 types (Figure 2) in order to simplify the natural examples and facilitate interpretation of the modeling results. A total of eight experiments were run to examine the architecture and the spatio-temporal change of strain distribution.

Type 1 is the simplest model, having a continuous single-detachment layer at the base (Figure 2b) to represent the basic accretion cycle for the reference to other type. Type 2 has continuous double-décollement layer at the base and in the middle of the incoming sedimentary succession (Figure 2c). The models of this type are intended to replicate an interbedded detachment layer representing major lithological boundaries or unconformities in nature (e.g., Smith et al., 2012; Dileonardo et al., 2002; Frederik et al., 2020).

Type 3 and 4 models are variations of types 1 and 2, respectively, where a 90-mm-wide interval of the basal microbead layer is replaced with a sand mound (see Section 3.2 for the materials we used), which interrupts the continuity of the frictional weakness at the plate interface (Figure 2d, e). Type 3 and 4 models are used to evaluate the architecture and fault activities related to the subduction of a frictional discontinuity with or without an interbedded weak layer, respectively. The deformable and detachable sand mound acts as a high-friction patch in the décollement, and thus is different from previous studies that have used rigid and fixed ridges (e.g., Noda et al., 2020).

3.2 Materials

Granular materials have been widely used to simulate geological structures (Klinkmüller et al., 2016). They exhibit a similar behavior to brittle rocks, because they respond to elastic–frictional plastic deformation by pre-failure strain hardening and post-failure strain softening until a dynamically constant shear is reached (e.g., Klinkmüller et al., 2016; Lohrmann et al., 2003; Ritter et al., 2016). Dry quartz sand (GA39; produced by Sibelco, France) and glass microbeads (CVP70-110) were used to simulate the sediment in this study. The sand was used for the incoming sediment, the proto-wedge, and the sand mound, which correspond to trench-fill turbidites, pre-existing accretionary wedge, and high-friction patch on the plate interface in nature, respectively. The glass microbeads were used for the basal and interbedded weak layers (i.e., pelagic or clayey sediment). The physical properties of the sand and glass microbeads are summarized in Table 1.

The peak friction angles of the basal plastic sheet to the sand and to the glass microbeads were estimated from measurements of the angles of sliding friction (cf., van Burkalow, 1945), which were 51.3±1.9° ($n = 15$) and 41.0±3.1° ($n = 13$), respectively. These values are much higher than the peak internal friction angles of the sand (GA39) and microbeads (CVP70-110), indicating that basal shear occurs within the sediment layer (i.e., mainly within the microbeads) rather than on the surface of the underlying basal plastic sheet.

The theoretical taper (i.e., surface slope) angles and stability fields of the wedge were calculated according to the critical taper theory (Dahlen, 1984; Davis et al., 1983). The theoretical surface slope angles for the cases of the peak ($\alpha_{\phi_{\text{peak}}}$) and dynamic ($\alpha_{\phi_{\text{dynamic}}}$) friction angles of the sand are 7.5° and 9.6°, respectively, when glass microbeads are used for the basal décollement (Supporting Information S1 and Figure S1). We also calculated the theoretical width and height of the wedge for given theoretical surface slope angles (Supporting Information S1 and Figure S2).

3.3 Experimental setup

The apparatus used in this study was a glass-sided, rectangular deformation rig with internal dimensions of 1890 mm × 300 mm × 315 mm deep (Figure 2a). A wooden plate was vertically positioned at one end as a fixed and rigid backstop. The lateral glass walls were lubricated before each run to reduce the side-wall friction (cf., Souloumiac et al., 2012). A plastic (Mylar®) sheet was placed over the basal plastic plate of the rig and fixed to a stepping motor (left side of Figure 2a). The stepping motor pulled the plastic sheet beneath the incoming sediment at increments of 5.558 mm for each motor activation. The final amount of horizontal shortening L_s (successive increment) was ∼1000 mm, and the final wedge length was about 800 mm, corresponding ca. 60–120 km and 48–96 km in nature (see Section 3.4 for scaling).

The sand and glass microbeads were sprinkled into the rig from a height of ∼200 mm above the basal plastic sheet to ensure they were well-compacted (cf., Maillot, 2013). The total thickness of the layer was 35 mm (Figure 2). Thinly alternating colored sand layers and/or small triangles along the glass walls were used to visualize the cross-sectional structure. A proto-wedge, which was a wedge prepared in advance before the experiment to save experimental space and time (Graveleau et al., 2012), was made of the same sand as that used in the model and was placed next to the vertical wooden backstop (Figure 2). The proto-wedge had a basal length of 135±11.4 mm and surface slope of 31±2°.

3.4 Scaling

The mechanical properties of the materials must be properly scaled to obtain dynamic processes similar to those in nature. This condition can be satisfied if the ratio of the forces acting on the system in the experiments to those in nature is constant (Hubbert, 1937; Ramberg, 1981). Scaling rules indicate that the model-to-nature ratio for stress σ is as follows:

$$\frac{\sigma_{\mathrm{model}}}{\sigma_{\mathrm{nature}}} = \frac{\rho_{\mathrm{model}}}{\rho_{\mathrm{nature}}} \times \frac{g_{\mathrm{model}}}{g_{\mathrm{nature}}} \times \frac{L_{\mathrm{model}}}{L_{\mathrm{nature}}}, \tag{1}$$

where ρ, g, and L are density, acceleration due to gravity, and length of model or nature. The cohesion C can be substituted for stress σ (Graveleau et al., 2012; Schellart, 2000), and the experiments were performed under normal gravity ($g_{\mathrm{model}}/g_{\mathrm{nature}} = 1$), which yields:

$$\frac{L_{\mathrm{nature}}}{L_{\mathrm{model}}} = \frac{C_{\mathrm{nature}}}{C_{\mathrm{model}}} \times \frac{\rho_{\mathrm{model}}}{\rho_{\mathrm{nature}}}. \tag{2}$$

Although cohesion is stress-dependent (i.e., depth-dependent; Ikari & Kopf, 2011), we used reported values for the cohesion C and density ρ for sedimentary rocks in a natural accretionary wedge, which are 5 MPa and 2400 kg m^{-3}, respectively (Schumann et al., 2014). For the case of dry sand (C = 24–54 Pa; Table 1) used as the internal material in the models, the scaling factor $L_{\mathrm{nature}}/L_{\mathrm{model}}$ ranges between 0.6 × 10^5 and 1.2 × 10^5, indicating that 10 mm in the model corresponds to 0.6–1.2 km in nature. Therefore, the 35-mm-thick layer of incoming sediment is equivalent to a thickness of 2.1–4.2 km in nature, which is comparable to the thickness of trench-fill sediments at modern accretionary margins (Clift & Vannucchi, 2004; Noda, 2016). The total amount of shortening ($L_s \sim 1000$ mm) in this study corresponds to 60–120 km in nature, which occurs over 1.2–2.4 Myr for a plate convergence rate of 50 mm yr^{-1}. This duration corresponds to the timescale for the formation of the modern Nankai accretionary wedge that formed during the Quaternary (G. F. Moore et al., 2015).

3.5 DIC analysis

Time-lapse digital images were taken with a digital camera (Canon EOS 70D) at 5.558 mm displacement increments using a PC-based controller. The image sensor of the

CMOS APS-C has a resolution of 20.2 million pixels (5472 horizontal and 3648 vertical) and a dynamic range (DR) of 11.6. The absolute spatial resolution is ≈0.16 mm per pixel. The DIC technique was used to quantify the velocity field and strain rate from pairs of time-lapse digital images by matching the patterns of pixel color values. This enabled us to visualize spatial and temporal patterns in the horizontal and vertical displacements, and thus characterize strain localization or thrust activity within the deforming wedge. We used open-source subset-based 2D DIC software, Ncorr (Blaber et al., 2015), for the analysis to track the relative displacements of material points between a reference (pre-deformed) and target (post-deformed) image. This software can be used in MATLAB®.

The DIC analysis includes two calculation steps: (1) incremental displacement vectors of the 2-D deformation; and (2) strain. The displacement field in the region of interest is calculated with a subset radius of 20 pixels and subset spacing of 2 pixels. To obtain the displacement vectors for all subsets, Ncorr uses the Reliability Guided (RG–DIC) method (Pan, 2009). A smaller window radius (4 pixels) was used for the strain window algorithm (Pan et al., 2009) to calculate the displacement gradients and subsequent strains. The analytical resolution for both displacement and strain is ∼0.5 mm.

The maximum amount of shear strain ($\varepsilon_{\max}$) and its orientation (θ_s) were calculated from the maximum (ε_1) and minimum (ε_2) principal strains as follows:

$$\begin{aligned}
\varepsilon_{\max} &= \varepsilon_1 - \varepsilon_2 \\
\theta_s &= \frac{1}{2}\tan^{-1}\left(\frac{\varepsilon_{xx}-\varepsilon_{yy}}{2\varepsilon_{xy}}\right) \\
&\text{with} \\
\varepsilon_1 &= \frac{1}{2}(\varepsilon_{xx}+\varepsilon_{yy}) + \sqrt{\left(\frac{\varepsilon_{xx}-\varepsilon_{yy}}{2}\right)^2 + \varepsilon_{xy}^2} \\
\varepsilon_2 &= \frac{1}{2}(\varepsilon_{xx}+\varepsilon_{yy}) - \sqrt{\left(\frac{\varepsilon_{xx}-\varepsilon_{yy}}{2}\right)^2 + \varepsilon_{xy}^2} \\
\varepsilon_{xx} &= \frac{1}{2}\left(2\frac{\partial u}{\partial x} + \left(\frac{\partial u}{\partial x}\right)^2 + \left(\frac{\partial v}{\partial x}\right)^2\right) \\
\varepsilon_{xy} &= \frac{1}{2}\left(\frac{\partial u}{\partial y} + \frac{\partial v}{\partial x} + \frac{\partial u}{\partial x}\frac{\partial u}{\partial y} + \frac{\partial v}{\partial x}\frac{\partial v}{\partial y}\right) \\
\varepsilon_{yy} &= \frac{1}{2}\left(2\frac{\partial v}{\partial y} + \left(\frac{\partial u}{\partial y}\right)^2 + \left(\frac{\partial v}{\partial y}\right)^2\right),
\end{aligned}$$

where u and v are the horizontal (x) and vertical (y) displacements, respectively.

3.6 Measured parameters

We measured several geometric and kinematic parameters to quantify the deformation of the experimental wedge. The geometrical parameters include the width, height, and slope (α) (Figure 3). The slope is defined as the average dip between the highest point (P_1) and the deformation front (P_0) of the wedge (Figure 3b).

The kinematic parameters were extracted from the results of the DIC analysis. One-dimensional horizontal displacement vectors were measured in bottom and top measurement zones (Figure 3c). The bottom measurement zone was set at 15% of the wedge height above the base of the region of interest, and the top measurement zone was set below the surface at 85% of the wedge height, to exclude erroneous values near the boundary. The height for each measurement zone was ~2.4 mm. To calculate the normalized horizontal displacements at the top ($\hat{u}_{\mathrm{top}}$) and at the bottom ($\hat{u}_{\mathrm{bottom}}$), the average of the five displacement vectors within each zone at each x coordinate was divided by the maximum value (i.e., 95% of the highest value to avoid errors) of the horizontal displacement vector within the zone.

The normalized vertical displacement $\hat{v}$ was also obtained by averaging the values of the vertical displacement vectors between the bottom and top measurement zones at each x coordinate, and then dividing by the maximum value of the horizontal displacement in the bottom measurement zone. The normalized maximum shear strain in the bottom measurement zone $\hat{\varepsilon}_{\mathrm{max(bottom)}}$ and that in the top measurement zone $\hat{\varepsilon}_{\mathrm{max(top)}}$ were calculated in the same way as the normalized horizontal displacement (Figure 3d). The denominator of the normalization was the maximum shear strain in the measurement zone at each time step. The orientation of the maximum shear strain (θ_s) was used to determine whether the shear strain was negative or positive. In this study, backthrusting (inward-vergent fault) and forethrusting (outward-vergent fault) represent negative and positive strains, respectively (bluish and reddish colors in Figure 3d). The dip angles of the forethrusts ($\delta_{\mathrm{f(init)}}$ and $\delta_{\mathrm{f(final)}}$) and backthrusts ($\delta_{\mathrm{b}}$) were measured on the cross-sectional images to estimate the effective friction angles of the incoming sediment (ϕ') and the effective slope angles (α') at the deformation front when a new thrust was initiated (Figure 3e; see Supporting Information S2).

3.7 Model limitations

Sandbox modeling has several limitations and cannot replicate some processes that occur in natural accretionary wedges. The experiments are basically performed under dry and (mostly) non-cohesive conditions and, therefore, can only consider brittle deformation. In nature, elevated pore fluid pressures within the wedge and décollement likely contribute to significant weakening of the strength (Hubbert & Rubey, 1959). In addition, our models do not account for dewatering, diagenetic alteration and presence of phyllosilicates, which may change the material properties or the mechanical strength in a natural forearc (Hyndman et al., 1997, 1995; J. C. Moore & Saffer, 2001; Morrow et al., 1992). Inner or deeper part of the wedge tends to be more strong due to the progressive dewatering and compaction than the outer or shallower part of the wedge. This likely increases the strength contrast in the wedge between the inner and outer parts as the wedge grows, leading to promote segmentation between them (H. Kopp & Kukowski, 2003; Lohrmann et al., 2003).

The backstop and basal plastic plate are rigid and fixed, meaning that neither flexural changes nor isostatic compensation are incorporated in our models (cf., Schellart & Strak, 2016). In addition, the fixed backstop prevents deformation or rotation of the boundary between the accretionary wedge and arc massif (i.e., the backstop), and does not allow sediment outflux, which can be an important factor during subduction erosion and shrinkage of the accretionary wedge (Gutscher et al., 1998b; Kukowski & Oncken, 2006; Lohrmann et al., 2006). This study does not consider syn-tectonic sedimentation or surface erosion, which can thicken the thrust sheet and result in exhumation of the underplated sediment, respectively (Konstantinovskaya & Malavieille, 2011; Malavieille et al., 2019; Perrin et al., 2013). These potential limitations should be carefully evaluated when applying the results of this study to natural accretionary wedges.

4 Results

4.1 Geometric parameters

The wedge width data and taper angles show that the wedge growth pattern is cyclical for the type 1 and 2 models (Figures 4 and S3). When a new thrust propagates, the wedge widens abruptly and the slope angle instantly decreases. This cyclical behavior has been previously described as episodic accretion (Koyi, 1995; Mulugeta & Koyi, 1992), accretionary cycle (Gutscher et al., 1998a), cyclic frontal accretion (Hoth et al., 2007), or punctuated thrust activity (Naylor & Sinclair, 2007). In contrast to this episodic evolution, the wedge height evolves nearly linearly without cyclical fluctuations, especially in the latter half of the experiments ($L_s > 400$ mm), for both the type 1 and 2 models (Figure 4b and S3b).

The geometric parameters from the type 1 and 2 models basically follow the trends of the theoretical width, height, and slope. However, the slope angle decreases linearly throughout the experiments, whereas the theoretical slope angle is constant (Figure 4c). A comparison of wedge geometry in terms of the number of weak layers (type 1 versus 2) shows magnitude of amplitude of the width and slope fluctuation is higher for the type 1 model (Figures 4 and S3). In addition, the height and slope of the type 2 model are lower than the theoretical values (Figures 4b, c and S3).

For the models with the discontinuous basal décollement (types 3 and 4), their geometric patterns of cyclicity are significantly different from the type 1 and 2 models after the onset of sand mound subduction. The slope increases as the width decreases in the type 3 model (M08; L_s = 440–590 mm in Figure 4), while the width and slope are nearly constant through the same interval in the type 4 model (M10; L_s = 405–610 mm). The width, height, and slope of the type 3 and 4 models deviate from the theoretical values following subduction of the sand mound. In the type 3 model, the width is narrower than the theoretical one, and the maximum slope α is close to the theoretical angle of $\alpha_{\text{case3}} = 11.3°$ (Figure 4). In the type 4 model, the height is higher than the theoretical one in the latter half of the experiment. The magnitude of amplitude of the width change for the type 4 model is much smaller than those of the type 3 model.

4.2 Structures

The structural patterns of the wedges vary depending on the presence of an interbedded weak layer and a frictional barrier in the basal décollement (Figures 5 and S4). The internal structure of the type 1 model (single décollement) is characterized by thick imbricate thrust sheets bounded by deeply rooted forethrusts, which shows that a piggyback style of frontal accretion is dominant for this wedge. Some minor backthrusts are developed as a set of conjugate faults when the frontal forethrust pops up a ramp (Figure 5a). The thrust spacing is nearly even, but it is narrower in the inner part than in the outer part of the wedge. The density of fault network is sparse.

In contrast, the internal structure of the type 2 model (double décollement) is characterized by frontal accretion involving deeply and shallowly rooted thrusts; the latter are almost totally coinciding with the weak interbedded layer of microbeads (Figures 5b and S4b, c). The final dip angles of the deeply rooted forethrusts in the type 2 model are gentler than those of the type 1 model (Figure 5b). The resultant fault network is more complicated and has higher connectivity between the faults than in the type 1 model.

The cross-section geometries of the type 3 and 4 models (discontinuous basal décollement) have a steeply sloping inner wedge and gently sloping outer wedge (Figures 5c, d and S4d-h). The thrust (F_5 in M08 or F_4 in M10) is associated with the sand mound subduction and underthrusting of a long thrust sheet in the wake of the sand mound (i.e., "shadow zone" of Dominguez et al., 1998). The sediment underthrusting is accompanied by compression, as depicted by the narrow spacing of the older thrust sheets. The wedge structure is represented by a vertical stack of underthrusted sediment in the wake of the sand mound. For example, the thrust sheet between F_5 and F_6 in the type 3 model (M08) is completely underthrusted beneath the previously formed thrust sheet.

As a major difference between the type 3 and 4 model, the type 4 mode has a considerably higher amount of underthrusting than the type 3 model (Figure 5d). The lower part of the incoming sediment is underplated by the underthrusting sand mound which has finally reached the bottom of the proto-wedge. Another difference in the type 4 model is that the shallower thrusts form a thin-skinned duplex structure where the upper part of the incoming sediment is detached from the lower part being underthrusted beneath the wedge front (Figure 5d).

4.3 Kinematic parameters

4.3.1 Visualization

We use several different parameters to show how the wedge deforms during the accretion. The horizontal displacements in the top and bottom measurement zones ($\hat{u}_{\text{top}}$ and $\hat{u}_{\text{bottom}}$) are used as indicators of the degree to which the overlying sediment layer is coupled or decoupled as compared with the moving basal sheet (Figure S5). For example, the accreted or incoming sediment is fully coupled with the basal plastic sheet when $\hat{u} = 1$; partially coupled/decoupled when $0 < \hat{u} < 1$; and fully decoupled when $\hat{u} = 0$. We also use the ratio of the top to bottom horizontal displacement $\hat{u}_{\mathrm{top}}/\hat{u}_{\mathrm{bottom}}$ as an indicator of intra-wedge segmentation (coupling/decoupling between the upper and lower parts of the wedge). When $\hat{u}_{\mathrm{top}}/\hat{u}_{\mathrm{bottom}} \sim 0$, the basal part of the wedge is decoupled from the upper part and underthrusted, whereas the basal part of the wedge moves together (coupled) with the upper part when $\hat{u}_{\mathrm{top}}/\hat{u}_{\mathrm{bottom}}$ is close to 1. In addition, we use normalized vertical displacement $\hat{v}$ to visualize the places where the wedge is uplifting/subsiding during the deformation (Figure S6). The normalized maximum shear strains in the top and bottom measurement zones ($\hat{\varepsilon}_{\mathrm{max(top)}}$ and $\hat{\varepsilon}_{\mathrm{max(bottom)}}$) show the strain-concentration zones, meaning which thrusts are actively displacing (Figure S7).

The resultant diagrams for those parameters are shown in Supporting Information (Figures S5, S6, S7). In each diagram, the horizontal and vertical axes indicate the distance from backstop (D_b) and shortening (L_s, equivalent to time), respectively. The accretionary wedge width is defined by the length from the backstop ($D_b = 0$) to the deformation front (thick solid line in Figures S5, S6, S7), which gradually widens as the shortening increases while the deformation front repeats back and forth cyclically. In the following sections, we focus on the cyclic accretion process in different model types. Each accretion cycle can be decomposed into four successive phases (Figure 6), which are basically followed by the previous studies (Adam et al., 2005; Dotare et al., 2016; Hoth et al., 2007; Marshak et al., 2019; Ritter et al., 2018).

4.3.2 Continuous single-décollement model (Type 1)

The accretion cycle begins with the preparation phase (phase 1) before the nucleation of a new frontal forethrust (Figure 6a and original DIC images without interpretations are shown in Figure S8). The outer part of the wedge has slightly reduced $\hat{u}_{\mathrm{bottom}}$ (D_b = 500–600 mm; Figure 7a) as compared with the previous phase, and several thrusts (F_2 and F_4–F_7) are active simultaneously (Figures 6a and 7i). The uplift ($\hat{v} > 0.05$) is observed mainly between F_4 and F_6 (D_b = 400–520 mm; Figures 6a and 7g), but small-scale uplift ($\hat{v} < 0.05$) also occurs ahead of the deformation front (D_b = 640–700 mm in Figures 6a and 7g), which can be correlated with the proto-thrust zone (cf., Barnes et al., 2018; MacKay, 1995). This phase corresponds to stage 1 of the strain-hardening phase (Ritter et al., 2018), stage 1 of the deformation propagation phase (Dotare et al., 2016), or the reactivation phase (Hoth et al., 2007).

The following phase (phase 2) is the first phase in the lifespan of a new frontal thrust (Figure 6a). In this phase, the strain is localized between the new frontal forethrust (F_8) and its conjugate backthrust where a new ramp pops up (Figures 6a and 7g). The strain localization at the outermost part of the wedge causes basal decoupling ($\hat{u}_{\text{bottom}} < 0.1$), strong intra-wedge coupling (high $\hat{u}_{\text{top}}/\hat{u}_{\text{bottom}}$), and no uplift (low $\hat{v}$) in the most part of the wedge ($D_b < 700$ mm; Figure 7c, e, g). Older thrusts (F_4–F_7) become inactive, resulting in F_8 being the only active forethrust (Figures 6a and 7i). This phase corresponds to stage 2 of the strain weakening phase (Ritter et al., 2018), stages 2 and 3 of the thrust initiation to active frontal thrusting phase (Dotare et al., 2016), and the thrust initiation phase (Hoth et al., 2007).

Phase 3 is characterized by the accretion of a new thrust sheet to the wedge in association with reactivation of the previous frontal thrust (F_7 in Figures 6a and 7i). This accretion increases $\hat{u}_{\text{top}}$ (D_b = 600–700 mm) and $\hat{u}_{\text{bottom}}$ (D_b = 250–650 mm) in the middle part of the wedge (Figure 7a, c). The location of the uplifted area migrates inward (D_b = 600–680 mm; Figure 7g). This phase can be correlated to stage 3 (Ritter et al., 2018) or the underthrusting phase (Hoth et al., 2007).

Frontal accretion during phase 4 results in inward propagation of the coupled area at the base of the wedge ($\hat{u}_{\text{bottom}} > 0.9$ in D_b = 550–680 mm; Figure 7c). The uplifted area also migrates inward (D_b = 500–600 mm; Figure 7g), and the pre-existing thrusts are reactivated in the order F_6 to F_4 (Figure 7i). In addition, diffuse uplift in the proto-thrust zone starts during this phase ($D_b > 700$ mm in Figure 7g). This phase can be compared with Stage 3/0 (Ritter et al., 2018) or the reactivation phase (Hoth et al., 2007).

The final phase in the lifespan of F_8 is the preparation phase (phase 1) for the next frontal thrust F_9 (Figure 6a). Multiple pre-existing thrusts (F_2 and F_4–F_8) are active simultaneously (Figure 7i) and the proto-thrust zone continues to undergo diffuse uplift (Figure 7g). This phase can be correlated with the reactivation phase (Hoth et al., 2007).

4.3.3 Continuous double-décollement model (Type 2)

The accretion cycles observed in the type 2 model are similar to those in the type 1 model, but with several differences (Figure 6b and original DIC images without interpretations are shown in Figure S9). These include: (1) propagation of a new shallowly rooted frontal forethrust at the deformation front and (2) use of the interbedded weak layer for rearrangement of pre-existing thrusts when they are reactivated (Figure 6b).

The first difference is evident in phase 3 where a new frontal shallowly rooted forethrust F_{6a} results in outward migration of the deformation front (Figures 6b and 7b). The low $\hat{u}_{\mathrm{top}}/\hat{u}_{\mathrm{bottom}}$ value in the frontal part of the wedge (D_b = 450–500 mm; Figure 7f) during phases 2 and 3 shows intra-wedge decoupling between the upper and lower parts of the wedge. This is evident from the underthrusting of the lower part of the incoming sediment beneath the wedge front (Figure 6b).

The second difference is evident from the multiple deeply and shallowly rooted thrusts that are simultaneously active, especially in phases 1 and 4 (Figures 6b and 7j). Low $\hat{u}_{\mathrm{top}}/\hat{u}_{\mathrm{bottom}}$ values (<0.3) in the inner part of the wedge (D_b = 230–320 mm) are indicative of intra-wedge decoupling due to out-of-sequence thrusting of the shallowly rooted forethrust F_{3d} (Figure 7j). The reactivated thrusts of F_{5a} and F_{5b} in phase 4 are associated with a localized uplift in the outer part of the wedge (D_b = 460–500 mm; Figure 7h).

4.3.4 Discontinuous décollement models (Types 3 and 4)

Subduction of the sand mound (type 3 and 4 models) has a significant effect on the accretion cycle. One of the important effects on wedge deformation is sediment underthrusting (Figure 8 and original DIC images without interpretations are shown in Figures S10 and S11). In the type 3 model, a thrust sheet including the sand mound is underthrusted beneath the wedge and associated with a long-lived forethrust F_5 at the inward flank of the sand mound (Figure 8a). Underthrusting is much more conspicuous in the type 4 model (Figure 8b), where the basal part of the wedge is coupled to the subducting plate (high $\hat{u}_{\mathrm{bottom}}$, red zone in Figure 9d) and the upper wedge is completely decoupled from the lower wedge (low $\hat{u}_{\mathrm{top}}/\hat{u}_{\mathrm{bottom}}$, blue zone in Figure 9f). At the same time, several shallowly rooted thrusts are formed at the deformation front (L_s = 500–745 mm in Figure 8b and F_{4a}–F_{4g} in Figure 9b) with the long-lived displacements of F_4 in the type 4 model (Figure 9j).

Another effect in the type 3 and 4 models is that the uplifted area propagates farther inward than in the type 1 and 2 models while the sand mound is being subducted (Figures 8 and 9). However, the uplifting patterns between the type 3 and 4 models are different each other. The uplift in the type 3 model (L_s = 400–800 mm) is widespread between the backstop and subducting sand mound (Figure 9g), while that in the type 4 model (L_s = 400–750 mm) is narrower and more concentrated along the pathway of the mound than in the type 3 model (Figure 9h). In addition, the type 4 model exhibits a negative vertical displacement (i.e., subsidence) mostly in the wake of the sand mound (Figure 9h).

5 Discussion

5.1 Accretion cycles in single-décollement wedges

Repetition of episodic frontal accretion allows an accretionary wedge to maintain a critical taper angle (Del Castello & Cooke, 2007; Gutscher et al., 1996; Hoth et al., 2007; Stockmal et al., 2007; Storti et al., 2000). The nature of each accretion cycle has been discussed from the viewpoint of mechanical equilibrium or work budget (e.g., Cubas et al., 2008; Del Castello & Cooke, 2007; Gutscher et al., 1998a; Herbert et al., 2015; McBeck et al., 2017; Platt, 1988). Here we propose another simple conceptual model of an accretion cycle for normal frontal accretion, and explain the cycle based on the relative strengths of the wedge and basal detachment (cf., Bonini, 2018; Oncken et al., 2012; Suppe, 2007; von Hagke et al., 2014).

5.1.1 Conceptual model of the accretion cycle

An accretion cycle, from the preparation phase for new frontal thrust initiation (phase 1) to the reactivation of pre-existing thrusts (phase 4), can be discussed in terms of the inward increases in horizontal and vertical displacements during the cycle ($\hat{u}$ and $\hat{v}$ in Figure 7). The accretion cycle may start when the internal friction angles of the inner (ϕ_{in}) and outer (ϕ_{out}) parts of the wedge approach their peak values (Figure 10a). Maximization of the internal friction results in the internal domain being resistant to deformation, which may further play a role in the strain-concentration zone jump to the protothrust zone represented by a diffuse uplift ahead of the deformation front.

At the critical point in terms of the force balance or work optimization (cf., Cubas et al., 2008; Del Castello & Cooke, 2007; Gutscher et al., 1998a; McBeck et al., 2017), a new frontal thrust initiates ahead of the deformation front as multiple pre-existing faults in the wedge cease to be active (phase 2 in Figure 10b). This may be related with that the frictional resistance of the basal detachment becomes weaker than the internal wedge strength as the internal wedge hardens, leading to failure of the basal coupling at the plate interface and creep of the wedge on the basal detachment.

As the new frontal thrust sheet is accreted, the coupled zone gradually propagates inward in association with reactivation of the previous frontal thrust (F_2 in Figure 10c). This inward migration of the strain-concentration zone assists step-by-step reactivation of the pre-existing thrusts by tilting of the thrust dips in an inward direction (phases 3 and 4 in Figure 10d, e). Therefore, accretionary wedges are likely to experience repeated strain hardening and softening cycle (cf., Lohrmann et al., 2003; Nieuwland et al., 2000; Ritter et al., 2018), corresponding to strain hardening in the wedge (phase 1), strain localization in the outer wedge and dilation (strain softening) in the inner wedge (phase 2), and renewed hardening as the strain propagates inward (phases 3–4).

5.1.2 Wedge strength versus detachment strength

From the perspective of the relative strength of the wedge and basal detachment (Davis et al., 1983; Suppe, 2007), we consider the strain hardening and weakening cycle to represent variations in the effective internal friction angle of the wedge. When the wedge strength is sufficient to prevent failure, the wedge is decoupled and creeps on the basal detachment without any deformation. However, when the frictional shear strength of the detachment is strong enough to deform the wedge, the basal interface is locked and the wedge is deformed. The wedge strength (W_s) and basal detachment strength (F_s) can be obtained from the differential and basal shear stresses for a given wedge height H (Davis et al., 1983; Suppe, 2007):

$$W_s = \frac{\sigma_1 - \sigma_3}{\rho g H} \tag{3}$$

$$F_s = \frac{\tau_b}{\rho g H} \tag{4}$$

with

$$
\begin{aligned}
\sigma_1 - \sigma_3 &= \frac{2\rho g H \cos\alpha \sec 2\psi_0}{\csc\phi' \sec 2\psi_0 - 1} \\
\tau_b &= -\sigma_n \tan\phi'_{\mathrm{b}} \\
\sigma_1 &= \sigma_z - \frac{1}{2}(\sigma_z - \sigma_x)(1 + \sec 2\psi_0) \\
\sigma_3 &= \sigma_z - \frac{1}{2}(\sigma_z - \sigma_x)(1 - \sec 2\psi_0) \\
\sigma_n &= \sigma_z - \tau_{xz} \sin 2\alpha - \frac{1}{2}(\sigma_z - \sigma_x)(1 - \cos 2\alpha) \\
\sigma_z &= -\rho g H \cos\alpha \\
\tau_{xz} &= \frac{1}{2}(\sigma_z - \sigma_x) \tan 2\psi_0 \\
\frac{1}{2}(\sigma_z - \sigma_x) &= \frac{-\sigma_z}{\csc\phi' \cdot \sec 2\psi_0 - 1}
\end{aligned}
$$

where ϕ' and ϕ'_b are the effective friction angle of the wedge and the detachment, respectively. ψ_0 is derived from Eq. S3 (Supporting information S2).

We calculated W_s and F_s acting on the inner and outer parts of a given wedge (Figure 11a). For the initial conditions, we used an inner wedge length L_{in} of 600 mm and a thickness of the incoming sediment $H_0 = 35$ mm. We also assumed that the effective friction angle ϕ' and inner wedge slope α_{in} vary within the range of the critical values between the peak ($\alpha_{\phi_{\mathrm{peak}}}$) and dynamic ($\alpha_{\phi_{\mathrm{dynamic}}}$) friction angles (Figure 11b). In addition, the baseline of the internal friction angle in the inner wedge may be higher than that in the outer wedge, because the inner wedge could have accumulated more strain and undergone greater compaction than the outer wedge. The initial length of the outer wedge (L_{out}) is as a function of the dip angles of a conjugate forethrust and backthrust is as follows:

$$L_{\mathrm{out}} = H_0 \left(\frac{1}{\tan\delta_{\mathrm{f}}} + \frac{1}{\tan\delta_{\mathrm{b}}} \right)$$

where δ_{f} and δ_{b} are the dip angles of the frontal forethrust and backthrust, which were derived from Eqs S1 and S2 (Supporting Information S2). By using these assumptions, we calculated W_s and F_s with Eqs 3 and 4.

The resultant trends of the wedge and detachment strengths for the above conditions (Figure 11) show that both the inner and outer wedges experience strengthening/weakening and decoupling/coupling during an accretion cycle (Figures 11f and 12). The wedge strength depends on the variations of the internal friction angles related to strain hardening and softening (Figure 11b, f). In the preparation phase for a new frontal thrust, both the inner and outer wedge are strengthened and approach the critical state (point a in Figure 12). After the new thrust emerges, the outer wedge is strong enough to be decoupled from the basal detachment and the reduction of the detachment strength in the inner wedge may also cause creeping of the wedge on the basal detachment (point b in Figure 12). Then the outer wedge gradually weakens, leading to basal coupling with the detachment (point c in Figure 12). The degree of coupling or decoupling may be determined by the degree to which the wedge weakens or the detachment strengthens. An important point is that the wedge strength is approaching the critical line of $\alpha_{\phi_{\mathrm{peak}}}$, with a reduction in the amplitude of the wedge strength as the wedge experience multiple cycles (Figure 12). This may explain the trends in the wedge slope angle approaches to the critical value $\alpha_{\phi_{\mathrm{peak}}}$ (Figure 4c).

An implication from our study for understanding natural accretionary wedges is that the wedge increases its strength and approaches to its critical state during the accretion cycles. However, our experiments have some limitations. For example, realignment of frictionally weak minerals (phyllosilicates like talc or smectite) in fault zones due to repeated slips could weaken both the wedge and the detachment strengths (cf., Bedford et al., 2022; Collettini et al., 2009). In addition, pore fluid pressure in the basal décollement zone reduces the detachment strength, which facilitates the wedge is decoupled and creeps on the plate interface. On the other hand, the wedge and detachment strengths in the inner and deeper part may increase due to compaction associated with progressive dewatering (Hyndman et al., 1995, 1997; J. C. Moore & Saffer, 2001; Morrow et al., 1992) and due to diagenetic alteration including the smectite–illite transition (Okuda et al., 2023; Saffer et al., 2012). Geometric heterogeneity of the subducting plate interface may also affect the frictional property and the detachment strength. As the wedge grows, this depth-dependent alteration of the material properties may promote segmentation between the inner and outer parts not only in the wedge but also in the décollement zone, leading to differentiate the wedge strength (H. Kopp & Kukowski, 2003; Lohrmann et al., 2003) and the detachment strength (Wang & Hu, 2006).

5.1.3 Time scaling

Hoth et al. (2007) noted that the accretion cycle represents an internal clock of wedge-scale deformation in the time scale of 10^5 years. In our study, the intervals of each accretion cycle are nearly constant (120–140 mm of the shortening length for a new thrust propagation) in the type 1 model (Figures S12a and S13). Because the timescale of the accretion cycle depends on the plate convergence rate (Naylor & Sinclair, 2007), when we assume the convergence rate V_c is 50 mm yr^{-1}, about 120–140-mm of shortening ($\sim$12–14 km in nature, if the length scale is 10^5) is equivalent to 0.24–0.28 Myr. This duration is comparable with the minimum time (t_c) required for the completion of a frontal accretion cycle, based on the following empirical equation (Hoth et al., 2007):

$$t_c = 4D/V_c, \tag{5}$$

where D is the thickness of the trench-fill sediment (m). Equation 5 yields $t_c = 0.28$ Myr in the case of $D = 3.5$ km and $v = 50$ mm yr^{-1}, which is similar to the values for the Nankai, Cascadia, Makran margins (figure 10 in Hoth et al., 2007).

An insight from our study in understanding modern (10^0–10^2 years) snapshots of natural subduction zones is that the degree of coupling/decoupling and also the size/locus of the strain at the plate boundary depend on the phase of accretion cycle ($\sim 10^5$ years). Although the time scale of the accretion cycle is longer than earthquake recurrence intervals, this could be comparable with a sudden stress drop on the subduction interface when a mega-thrust earthquake occurs, which changes the subduction zone from a quasi-steady state loading mode (i.e., stick) to a temporarily non-stationary (i.e., transient) relaxation mode. In our case, accretionary wedges in phase 2 tend to be relatively weakly coupled, and thus may exhibit higher levels of creep (i.e., low seismic coupling) than in the other phases. In contrast, the wedge in phase 4 would be more strongly coupled to the lower plate than in the other phases, suggesting some asperities drag the wedge base and accumulated strain would be released during a large earthquake. We speculate that the stress distribution on the plate interface in natural subduction zones may be affected by the accretion cycle over the long-time scale.

5.2 Role of the interbedded weak layers

In this section, we discuss the differences in the effective friction angles from its peak (ϕ'_{peak}) to stable sliding (ϕ'_{stable}) condition between the single- and double-décollement models by using Mohr diagrams (Figure 13) with observations of the thrust dip angle of a new forethrust ($\delta_{\text{f(init)}}$) and that of the trailing previously formed frontal thrust ($\delta_{\text{f(final)}}$)

when the new forethrust initiates in addition to estimated effective slope angles α' (Figures S12b and S13d–e; Supporting Information S2).

For the single-décollement model (type 1 in Figure 13a), the estimated effective basal friction angle ($\phi'_{\text{base}} = 24.5°$) almost coincides with the measured friction angle of the glass microbeads ($\phi_{\text{dynamic}} = 24.0°$; Table 1) when the wedge taper angle is equal to $\alpha_{\phi_{\text{case2}}}$ ($\alpha_{\phi_{\text{dynamic}}} = 9.6°$ in Figure S1). The effective internal friction angle (ϕ') ranges from ϕ'_{peak} $= 31.4°$ for the peak to $\phi'_{\text{stable}} = 29.0^{+0.7°}_{-0.9°}$ for the stable sliding, and is much larger than ϕ'_{base}. This suggests that the basal weak layer always works as a décollement. Smaller angles of ϕ'_{peak} and ϕ'_{stable} than the measured friction angles of sand ($\phi_{\text{peak}} = 35.5°$ and $\phi_{\text{dynamic}} = 30.8°$ in Table 1) may be caused by: (1) the incoming sediment layer that consists of sand and glass microbead layers; or (2) microbead grains that penetrate the shear zone at the frontal thrust.

For the type 2 model, the effective internal friction angle ($\phi'_{\text{peak}} = 27.6°$ and ϕ'_{static} $= 23.4^{+1.9°}_{-1.5°}$) and basal friction angle ($\phi'_{\text{base}} = 21.0°$ when $\alpha_{\phi_{\text{case2}}} = 9.6$) are smaller than those for the type 1 model (Figure 13b), suggesting that the internal strength of the type 2 model is smaller than that of the type 1 model. The similar value of the lower limit of $\phi'_{\text{stable}} = 21.9°$ to $\phi'_{\text{base}} = 21.5°$ may reduce the relative strength of the wedge to the detachment, implying more intense deformation than the type 1 model.

5.3 Role of discontinuity in the basal décollement

The discontinuous basal décollement in the type 3 and 4 models produced similar features in geometries and kinematics as those caused by seamount/ridge subduction, although our sand mound was neither rigid nor fixed to the base (cf., Dominguez et al., 2000; Lallemand et al., 1992; Miyakawa et al., 2022; Noda et al., 2020; Okuma et al., 2022; Ruh et al., 2016). For the type 3 model, when the sand mound starts to be subducted at the deformation front, the wedge enters a compressively unstable regime in order to adjust to the higher basal friction until the wedge reaches a new equilibrium with a higher taper angle (Figure 14a). A high-friction sandy mound behaves as a physical barrier to the basal décollement and prevents outward propagation of displacement, which promotes outward stepping up of the décollement and the sediment underthrusting (Figure 14a). The resultant geometry is comparable to that of a single wedge composed of two or more critical taper segments, comprising the strongly compacted inner wedge and weakly compacted outer wedge (cf., Lohrmann et al., 2003). This strengthened part of the inner wedge is capable to work as a "dynamic" backstop for the younger frontal accretion, which produces a middle-wedge slope break and middle-slope ramp (e.g., H. Kopp & Kukowski, 2003; Miyakawa et al., 2010).

The double-décollement model (type 4) is characterized by sediment underthrusting with a large displacement along the interbedded weak layer, which produces a duplex structure in the lower part of the inner wedge and a flat ramp in the middle wedge (Figure 14b). Our type 4 model suggests that the continuous interbedded weak layer can work as a plate boundary fault while the sand mound is subducting and produce a longer, shallower dipping, and smoother plate interface than the type 3 model (Figure 14a, b).

The detachable sand mound used in this study might have produced the persistent difference between the type 3 and 4 models. In the type 3 model, the uplift continued for longer in the inner part of the wedge than in the double-décollement model (type 4), even after the sand mound slowed the convergence rate (L_s = 600–800 mm in Figure 9g). In the type 4 model, the uplift in the inner wedge ceased abruptly after the sand mound stopped the subduction ($L_s \approx 730$ mm in Figure 9h). This difference suggests that the patterns of inner wedge uplift may depend on the heterogeneity in the frictional property on the plate interface or presence of the interbedded weak layer.

As compared with previous models of subduction of partially buried seamounts (Dominguez et al., 2000), our models reproduced neither backthrusts in the inward flank of the seamount nor normal faults in the wake of the seamount (Figure 14a–c). Recent numerical models (Pajang et al., 2022) indicate that subduction of a topographically large-scale seamount is necessary for the emergence of crustal-scale normal faults. Therefore, wedge-scale backthrusts and normal faults might be caused by the topographic effect of an exposed seamount rather than the subduction of a buried high-friction interval.

5.4 Comparison with natural accretionary wedges

The architecture (e.g., fault network and thrust spacing) of the Sinu Fold Belt, which is an accretionary wedge where the Caribbean Plate subducts beneath the South American Plate, is comparable with our type 1 (continuous single-décollement) model (Figure 1a). The common features between them are that most thrusts emanate from the basal detachment forming an imbricate thrust system. The thrust spacing is relatively homogeneous but narrower in the inner wedge than the outer wedge (Rodríguez et al., 2021). The major difference in the Sinu Fold Belt from our model is the presence of normal faults on the continental shelf. This may be caused by gravitational tectonics due to a very weak friction in the basal detachment associated with mud diapirs or local extension due to transtensional rotation of the inner wedge relative to the outer wedge (Rodríguez et al., 2021). Because our experiments are completely under the dry setting, we cannot produce excess pore fluid pressure in the décollement, which can make the wedge unstable to maintain the wedge taper. In addition, the subduction direction is perpendicular to the backstop in our model, meaning transpressional/transtensional deformation cannot be examined.

The Makran margin is shown as an example for the double décollement model (Figure 1b). In this margin, an unconformity within the incoming trench-fill sediment separates the lower sequence of mud-prone deep-sea sediment from the upper sequence of clastic sediment (Schlüter et al., 2002; Smith et al., 2012). This unconformity likely makes a property boundary between the two sequences and can be used as the main décollement when the lower sequence is underthrusted beneath the wedge and the upper sequence is accreted at the deformation front (Smith et al., 2012). The large stack of underplated sediment beneath the inner Makran margin (Burg, 2018) implies that the underthrusted sediment is decoupled from the subducting oceanic plate beneath the inner wedge (cf., Dal Zilio et al., 2020). This is the case for our type 4 model, which shows the high-friction interval (highly coupled area) on the plate interface enabled sediment underthrusting and underplating beneath the inner wedge (Figure 14b). The localized uplift at the inner wedge may provide an insight to the non-linear uplift rates at some marine terraces over $\sim 10^5$ to 10^6-yr timescales (e.g., Bishop et al., 2019; Melnick, 2016; Saillard et al., 2017). The temporal changes of the coastal uplifting rates in nature may reflect a spatial variation in frictional property along the subduction interface or a pulse of subduction of a discontinuous basal décollement.

Frederik et al. (2020) proposed a structural evolution model based on subduction of buried seamounts off Alaska, which includes: (1) shortening in the proto-thrust zone prior to subduction of a buried seamount; (2) a significant seaward jump of the deformation front due to the formation of the proto-thrust zone; and (3) steepening of the inner wedge and backthrusting with a potential décollement step-down beneath the middle wedge (Figure 14d). In their studied area, the incoming trench-fill sedimentary succession contains a major lithological boundary (Frederik et al., 2020; Gulick et al., 2015; Reece et al., 2011), which may act as a structural detachment that promotes underthrusting of the lower sequence of the trench-fill sediment. Frederik et al. (2020) speculated that underplating preferentially occurred on the wake side of the subducted seamounts, similar to our models in which the underthrusted sediments were underplated beneath the inner wedge. In our case, a combination of the presence of the interbedded weak layer and a detachable high-friction interval in the basal weak layer facilitates not only the décollement step-up to accommodate the subduction channel and underthrust the sediment but also the décollement step-down to underplate the sediment.

6 Conclusions

We employed four types of sandbox models by changing the décollement configurations, in order to investigate the effects of décollement conditions on growing accretionary wedges. The geometrical and DIC-based kinematic data yield the following conclusions.

The continuous single-décollement model is characterized by multiple cycles of frontal accretion associated with deeply rooted forethrusts. Each accretion cycle comprises four phases: the preparation (phase 1), initiation (phase 2), accretion (phase 3), and reactivation (phase 4) phases. The time scale of the cycle depends on the plate subduction rate and the sediment thickness, but the type 1 model can be scaled to the order of 10^5 years in nature. Through the accretion cycle, the wedge undergoes: (1) an inward shift of the strain locus with a stepwise inward propagation of the basal coupling area, and reactivation of pre-existing thrusts in the wedge; and (2) a sudden loss of the basal coupling under the wedge at the time of initiation of a new frontal forethrust. The accretion cycles is a fundamental process to make the wedge its critical state with hardening/weakening the relative strength of the wedge to the detachment associated with widening/narrowing the area of the basal coupling on the plate interface.

The presence of an interbedded weak layer enables the frontal forethrusts to exchange the detachment between the intermediate and basal levels, and enhances sediment underthrusting in the frontal part of the wedge during the phases 3–4 of the accretion cycle. The interbedded weak layer also has a role in rearrangement of the pre-existing fault network by reconnecting the deeply rooted thrusts with shallowly rooted thrusts when they are reactivated, leading to intra-wedge segmentation and additional underthrusting in the middle part of the wedge. The intermediate weak layer can also weaken the wedge strength and make denser fault network in the wedge than the type 1 model.

An interruption in the frictional weakness of the basal décollement increases the surface slope angle of the wedge and stimulates the out-of-sequence thrust activity. A combination of a frictional barrier in the basal décollement layer and the continuous interbedded décollement layer enables underplating of the underthrusted sediment beneath the inner wedge with a low-angle, long-lived, deeply rooted underthrusting and multiple frontal accretion with short-lived, shallowly rooted forethrusts by using the interbedded weak layer.

Our results highlight the décollement configuration is a critical factor to determine the accretionary process, the architecture, and the thrust activity in accretionary wedges. We think our detailed observation of the wedge geometry and the kinematics can be useful when we interpret natural accretionary wedges.

Data Availability Statement

Relevant multimedia data files and supporting figures are available for open access at https://figshare.com/s/efb13bc30c1a76d937a7 (Noda et al., 2023b). The data set and script files used in this contribution are archived following the FAIR principle at https://doi.org/10.5281/zenodo.7397374 (Noda et al., 2023a).

Acknowledgments

This research was undertaken while the first author was a visiting researcher at the Laboratoire d'Océanologie et de Géosciences, Université de Lille. The first author thanks all the faculty, staff, and students for their support in Lille. The frictional angles and cohesion of the used materials were measured at the Helmholtz Centre Potsdam, German Research Centre for Geosciences GFZ. We thank Tabito Matsu'ura for useful information regarding recent studies of coastal uplift. We are also grateful to Ayumu Miyakawa for numerous valuable comments on an early version of this manuscript. This study was partly funded by JSPS KAKENHI Grants 19KK0356, 21K03731, and JP21H05202. This manuscript is benefited greatly from many critical and constructive comments from Isabelle Manighetti, Editor-in-Chief, and anonymous reviewers. Finally, the last author Bruno Vendeville passed away while the first author was staying in Lille. Bruno made an indispensable contribution to the development of the laboratory in which this research was conducted, and was an avid educator, researcher, and mentor and friend to all authors of this paper.

References

Adam, J., Urai, J., Wieneke, B., Oncken, O., Pfeiffer, K., Kukowski, N., ... Schmatz, J. (2005). Shear localisation and strain distribution during tectonic faulting—new insights from granular-flow experiments and high-resolution optical image correlation techniques. *Journal of Structural Geology*, *27*(2), 283–301. doi: 10.1016/j.jsg.2004.08.008

Arnulf, A. F., Bassett, D., Harding, A. J., Kodaira, S., Nakanishi, A., & Moore, G. F. (2022). Upper-plate controls on subduction zone geometry, hydration and earthquake behaviour. *Nature Geoscience*, *15*(2), 143–148. doi: 10.1038/s41561-021-00879-x

Arnulf, A. F., Biemiller, J., Lavier, L., Wallace, L. M., Bassett, D., Henrys, S., ... Plaza Faverola, A. (2021). Physical conditions and frictional properties in the source region of a slow-slip event. *Nature Geoscience*, *14*(5), 334–340. doi: 10.1038/s41561-021-00741-0

Bangs, N. L., Gulick, S. P. S., & Shipley, T. H. (2006). Seamount subduction erosion in the Nankai Trough and its potential impact on the seismogenic zone. *Geology*, *34*(8), 701–704. doi: 10.1130/G22451.1

Bangs, N. L., Moore, G. F., Gulick, S. P. S., Pangborn, E. M., Tobin, H. J., Kuramoto, S., & Taira, A. (2009). Broad, weak regions of the Nankai Megathrust and implications for shallow coseismic slip. *Earth and Planetary Science Letters*, *284*(1–2), 44–49. doi: 10.1016/j.epsl.2009.04.026

Bangs, N. L., Shipley, T. H., Gulick, S. P. S., Moore, G. F., Kuromoto, S., & Nakamura, Y. (2004). Evolution of the Nankai Trough décollement from the trench into the seismogenic zone: Inferences from three-dimensional seismic reflection imaging. *Geology*, *32*(4), 273–276. doi: 10.1130/G20211.2

Barnes, P. M., Ghisetti, F. C., Ellis, S., & Morgan, J. K. (2018). The role of protothrusts in frontal accretion and accommodation of plate convergence, Hikurangi subduction margin, New Zealand. *Geosphere*, *14*(2), 440–468. doi: 10.1130/GES01552.1

Barnes, P. M., Lamarche, G., Bialas, J., Henrys, S., Pecher, I., Netzeband, G. L., ... Crutchley, G. (2010). Tectonic and geological framework for gas hydrates and cold seeps on the Hikurangi subduction margin, New Zealand. *Marine Geology*, *272*(1–4), 26–48. doi: 10.1016/j.margeo.2009.03.012

Barnes, P. M., Nicol, A., & Harrison, T. (2002). Late Cenozoic evolution and earthquake potential of an active listric thrust complex above the Hikurangi subduction zone, New Zealand. *Geological Society of America Bulletin*, *114*(11), 1379–1405. doi: 10.1130/0016-7606(2002)114<1379:LCEAEP>2.0.CO;2

Bedford, J. D., Faulkner, D. R., & Lapusta, N. (2022). Fault rock heterogeneity can produce fault weakness and reduce fault stability. *Nature Communications*, *13*(1), 326. doi: 10.1038/s41467-022-27998-2

Behrmann, J. H., Brown, K., Moore, J. C., Mascle, A., Taylor, E., Alvarez, F., ... Williams, C. (1988). Evolution of structures and fabrics in the Barbados Accretionary Prism. Insights from leg 110 of the Ocean Drilling Program. *Journal of Structural Geology*, *10*(6), 577–591. doi: 10.1016/0191-8141(88)90025-9

Bigi, S., Di Paolo, L., Vadacca, L., & Gambardella, G. (2010). Load and unload as interference factors on cyclical behavior and kinematics of Coulomb wedges: Insights from sandbox experiments. *Journal of Structural Geology*, *32*(1), 28–44. doi: 10.1016/j.jsg.2009.06.018

Bishop, B. T., Beck, S. L., & Zandt, G. (2019). Segmentation in continental forearcs: Links between large-scale overriding plate structure and seismogenic behavior associated with the 2010 Mw 8.8 Maule, Chile earthquake. *Tectonophysics*, *767*, 228164. doi: 10.1016/j.tecto.2019.228164

Blaber, J., Adair, B., & Antoniou, A. (2015). Ncorr: open-source 2D digital image correlation matlab software. *Experimental Mechanics*, *55*(6), 1105-1122. doi: 10.1007/s11340-015-0009-1

Bonini, M. (2018). Orogen-parallel variation in exhumation and its influence on critical taper evolution: The case of the Emilia-Romagna Apennine (Italy). *Tectonophysics*, *727*, 41–55. doi: 10.1016/j.tecto.2018.01.029

Bonnet, C., Malavieille, J., & Mosar, J. (2007). Interactions between tectonics, erosion, and sedimentation during the recent evolution of the Alpine orogen: Analogue modeling insights. *Tectonics*, *26*, TC6016. doi: 10.1029/2006TC002048

Burbidge, D. R., & Braun, J. (2002). Numerical models of the evolution of accretionary wedges and fold-and-thrust belts using the distinct-element method. *Geophysical Journal International*, *148*(3), 542–561. doi: 10.1046/j.1365-246x.2002.01579.x

Burg, J.-P. (2018). Geology of the onshore Makran accretionary wedge: Synthesis and tectonic interpretation. *Earth-Science Reviews*, *185*, 1210–1231. doi: 10.1016/j.earscirev.2018.09.011

Burg, J.-P., Dolati, A., Bernoulli, D., & Smit, J. (2013). Structural style of the Makran Tertiary accretionary complex in SE-Iran. In K. Al Hosani, F. Roure, R. Ellison, & S. Lokier (Eds.), *Lithosphere Dynamics and Sedimentary Basins: The Arabian Plate and Analogues* (pp. 239–259). Berlin, Heidelberg: Springer. doi: 10.1007/978-3-642-30609-9_12

Calvert, A. J., Preston, L. A., & Farahbod, A. M. (2011). Sedimentary underplating at the Cascadia mantle-wedge corner revealed by seismic imaging. *Nature Geoscience*, *4*(8), 545–548. doi: 10.1038/ngeo1195

Chesley, C., Naif, S., Key, K., & Bassett, D. (2021). Fluid-rich subducting topography generates anomalous forearc porosity. *Nature*, *595*(7866), 255–260. doi: 10.1038/s41586-021-03619-8

Clift, P. D., & Vannucchi, P. (2004). Controls on tectonic accretion versus erosion in subduction zones: Implications for the origin and recycling of the continental crust. *Reviews of Geophysics*, *42*, RG2001. doi: 10.1029/2003RG000127

Collettini, C., Niemeijer, A., Viti, C., & Marone, C. (2009). Fault zone fabric and fault weakness. *Nature*, *462*(7275), 907–910. doi: 10.1038/nature08585

Collot, J.-Y., Agudelo, W., Ribodetti, A., & Marcaillou, B. (2008). Origin of a crustal splay fault and its relation to the seismogenic zone and underplating at the erosional north Ecuador–south Colombia oceanic margin. *Journal of Geophysical Research*, *113*, B12102. doi: 10.1029/2008JB005691

Collot, J.-Y., Lewis, K. B., Lamarche, G., & Lallemand, S. (2001). The giant Ruatoria debris avalanche on the northern Hikurangi margin, New Zealand: Result of oblique seamount subduction. *Journal of Geophysical Research*, *106*, 19271–19297. doi: 10.1029/2001JB900004

Cook, B. J., Henstock, T. J., McNeill, L. C., & Bull, J. M. (2014). Controls on spatial and temporal evolution of prism faulting and relationships to plate boundary slip offshore north-central Sumatra. *Journal of Geophysical Research: Solid Earth*(7), 5594–5612. doi: 10.1002/2013JB010834

Cooke, M. L., & Madden, E. H. (2014). Is the Earth Lazy? A review of work minimization in fault evolution. *Journal of Structural Geology*, *66*, 334–346. doi: 10.1016/j.jsg.2014.05.004

Cubas, N., Agard, P., & Tissandier, R. (2022). Earthquake ruptures and topography of the Chilean margin controlled by plate interface deformation. *Solid Earth*, *13*(3), 779–792. doi: 10.5194/se-13-779-2022

Cubas, N., Leroy, Y. M., & Maillot, B. (2008). Prediction of thrusting sequences in accretionary wedges. *Journal of Geophysical Research*, *113*, B12412. doi: 10.1029/2008JB005717

Dahlen, F. A. (1984). Noncohesive critical Coulomb wedges: An exact solution. *Journal of Geophysical Research*, *89*(B12), 10125–10133. doi: 10.1029/JB089iB12p10125

Dahlen, F. A. (1990). Critical taper model of fold-and-thrust belts and accretionary wedges. *Annual Review of Earth and Planetary Sciences*, *18*(1), 55–99. doi: 10.1146/annurev.ea.18.050190.000415

Dal Zilio, L., Ruh, J., & Avouac, J.-P. (2020). Structural evolution of orogenic wedges: Interplay between erosion and weak décollements. *Tectonics*, *39*(10), e2020TC006210. doi: 10.1029/2020TC006210

Davis, D., Suppe, J., & Dahlen, F. A. (1983). Mechanics of fold-and-thrust belts and accretionary wedges. *Journal of Geophysical Research*, *88*(B2), 1153–1172. doi: 10.1029/JB088iB02p01153

Del Castello, M., & Cooke, M. L. (2007). Underthrusting-accretion cycle: Work budget as revealed by the boundary element method. *Journal of Geophysical Research*, *112*, B12404. doi: 10.1029/2007JB004997

del Castillo, E. M., Fávero Neto, A. H., & Borja, R. I. (2021). A continuum meshfree method for sandbox-style numerical modeling of accretionary and doubly vergent wedges. *Journal of Structural Geology*, *153*, 104466. doi: 10.1016/j.jsg.2021.104466

Deng, X., & Underwood, M. B. (2001). Abundance of smectite and the location of a plate-boundary fault, Barbados accretionary prism. *Geological Society of America Bulletin*, *113*(4), 495–507. doi: 10.1130/0016-7606(2001)113<0495:AOSATL>2.0.CO;2

Dileonardo, C. G., Moore, J. C., Nissen, S., & Bangs, N. (2002). Control of internal structure and fluid-migration pathways within the Barbados Ridge décollement zone by strike-slip faulting: Evidence from coherence and three-dimensional seismic amplitude imaging. *Geological Society of America Bulletin*, *114*(1), 51–63. doi: 10.1130/0016-7606(2002)114<0051:COISAF>2.0.CO;2

Dominguez, S., Lallemand, S., Malavieille, J., & von Huene, R. (1998). Upper plate deformation associated with seamount subduction. *Tectonophysics*, *293*(3), 207–224. doi: 10.1016/S0040-1951(98)00086-9

Dominguez, S., Malavieille, J., & Lallemand, S. (2000). Deformation of accretionary wedges in response to seamount subduction: Insights from sandbox experiments. *Tectonics*, *19*(1), 182–196. doi: 10.1029/1999TC900055

Dotare, T., Yamada, Y., Adam, J., Hori, T., & Sakaguchi, H. (2016). Initiation of a thrust fault revealed by analog experiments. *Tectonophysics*, *684*, 148–156. doi: 10.1016/j.tecto.2015.12.023

Egbert, G. D., Yang, B., Bedrosian, P. A., Key, K., Livelybrooks, D. W., Schultz, A., … Parris, B. (2022). Fluid transport and storage in the Cascadia forearc influenced by overriding plate lithology. *Nature Geoscience*, *15*(8), 677–682. doi: 10.1038/s41561-022-00981-8

Farzipour-Saein, A., & Koyi, H. (2016). Intermediate decollement activation in response to the basal friction variation and its effect on folding style in the Zagros fold-thrust belt, an analogue modeling approach. *Tectonophysics*, *687*, 56–65. doi: 10.1016/j.tecto.2016.09.006

Frederik, M. C. G., Gulick, S. P. S., & Miller, J. J. (2020). Effect on subduction of deeply buried seamounts offshore of Kodiak Island. *Tectonics*, *39*(7), e2019TC005710. doi: 10.1029/2019TC005710

Ghanadian, M., Faghih, A., Grasemann, B., Fard, I. A., & Maleki, M. (2017). Analogue modeling of the role of multi-level decollement layers on the geometry of orogenic wedge: an application to the Zagros Fold–Thrust Belt, SW Iran. *International Journal of Earth Science*, *106*(8), 2837–2853. doi: 10.1007/s00531-017-1462-0

Ghosh, S., Bose, S., Mandal, N., & Laik, A. (2020). Mid-crustal ramping of the Main Himalayan Thrust in Nepal to Bhutan Himalaya: New insights from analogue and numerical experiments. *Tectonophysics*, *782-783*, 228425. doi: 10.1016/j.tecto.2020.228425

Grando, G., & McClay, K. (2007). Morphotectonics domains and structural styles in the Makran accretionary prism, offshore Iran. *Sedimentary Geology*, *196*, 157–179. doi: 10.1016/j.sedgeo.2006.05.030

Graveleau, F., Malavieille, J., & Dominguez, S. (2012). Experimental modelling of orogenic wedges: A review. *Tectonophysics*, *538–540*, 1–66. doi: 10.1016/j.tecto.2012.01.027

Gulick, S. P. S., Jaeger, J. M., Mix, A. C., Asahi, H., Bahlburg, H., Belanger, C. L., . . . Swartz, J. M. (2015). Mid-Pleistocene climate transition drives net mass loss from rapidly uplifting St. Elias Mountains, Alaska. *Proceedings of the National Academy of Sciences*, *112*(49), 15042–15047. doi: 10.1073/pnas.1512549112

Gutscher, M.-A., Kukowski, N., Malavieille, J., & Lallemand, S. (1996). Cyclical behavior of thrust wedges: Insights from high basal friction sandbox experiments. *Geology*, *24*(2), 135–138. doi: 10.1130/0091-7613(1996)024<0135:CBOTWI>2.3.CO;2

Gutscher, M.-A., Kukowski, N., Malavieille, J., & Lallemand, S. (1998a). Episodic imbricate thrusting and underthrusting: Analog experiments and mechanical analysis applied to the Alaskan accretionary wedge. *Journal of Geophysical Research*, *103*, 10161–10176. doi: 10.1029/97JB03541

Gutscher, M.-A., Kukowski, N., Malavieille, J., & Lallemand, S. (1998b). Material transfer in accretionary wedges from analysis of a systematic series of analog experiments. *Journal of Structural Geology*, *20*(4), 407–416. doi: 10.1016/S0191-8141(97)00096-5

Haberland, C., Mokhtari, M., Babaei, H. A., Ryberg, T., Masoodi, M., Partabian, A., & Lauterjung, J. (2020). Anatomy of a crustal-scale accretionary complex: Insights from deep seismic sounding of the onshore western Makran subduction zone, Iran. *Geology*, *49*(1), 3–7. doi: 10.1130/G47700.1

Han, S., Bangs, N. L., Carbotte, S. M., Saffer, D. M., & Gibson, J. C. (2017). Links between sediment consolidation and Cascadia megathrust slip behaviour. *Nature Geoscience*, *10*(12), 954–959. doi: 10.1038/s41561-017-0007-2

Hardy, S., Duncan, C., Masek, J., & Brown, D. (1998). Minimum work, fault activity and the growth of critical wedges in fold and thrust belts. *Basin Research*, *10*(3), 365–373. doi: 10.1046/j.1365-2117.1998.00073.x

Hashimoto, Y., Sato, S., Kimura, G., Kinoshita, M., Miyakawa, A., Moore, G. F., . . . Yamada, Y. (2022). Décollement geometry controls on shallow very low frequency earthquakes. *Scientific Reports*, *12*(1), 2677. doi: 10.1038/s41598-

022-06645-2

Herbert, J. W., Cooke, M. L., Souloumiac, P., Madden, E. H., Mary, B. C. L., & Maillot, B. (2015). The work of fault growth in laboratory sandbox experiments. *Earth and Planetary Science Letters*, *432*, 95–102. doi: 10.1016/j.epsl.2015.09.046

Hoffmann-Rothe, A., Kukowski, N., & Oncken, O. (2004). Phase dependent strain partitioning in obliquely convergent settings. *Bollettino di Geofisica Teorica ed Applicata*, *45*(Suppl. 1), 93–97.

Hoth, S., Hoffmann-Rothe, A., & Kukowski, N. (2007). Frontal accretion: An internal clock for bivergent wedge deformation and surface uplift. *Journal of Geophysical Research*, *112*, B06408. doi: 10.1029/2006JB004357

Hubbert, M. K. (1937). Theory of scale models as applied to the study of geologic structures. *Geological Society of America Bulletin*, *48*(10), 1459–1519. doi: 10.1130/GSAB-48-1459

Hubbert, M. K., & Rubey, W. W. (1959). Role of fluid pressure in mechanics of overthrust faulting: I. Mechanics of fluid-filled porous solids and its application to overthrust faulting. *Geological Society of America Bulletin*, *70*(2), 115–166. doi: 10.1130/0016-7606(1959)70[115:ROFPIM]2.0.CO;2

Hyndman, R. D., Wang, K., & Yamano, M. (1995). Thermal constraints on the seismogenic portion of the southwestern Japan subduction thrust. *Journal of Geophysical Research*, *100*(B8), 15373–15392. doi: 10.1029/95JB00153

Hyndman, R. D., Yamano, M., & Oleskevich, D. A. (1997). The seismogenic zone of subduction thrust faults. *Island Arc*, *6*(3), 244–260. doi: 10.1111/j.1440-1738.1997.tb00175.x

Ikari, M. J., & Kopf, A. J. (2011). Cohesive strength of clay-rich sediment. *Geophysical Research Letters*, *38*, L16309. doi: 10.1029/2011GL047918

Ito, G., & Moore, G. F. (2021). Widths of imbricate thrust blocks and the strength of the front of accretionary wedges and fold-and-thrust belts. *Tectonophysics*, *799*, 228704. doi: 10.1016/j.tecto.2020.228704

Kirkpatrick, J. D., Edwards, J. H., Verdecchia, A., Kluesner, J. W., Harrington, R. M., & Silver, E. A. (2020). Subduction megathrust heterogeneity characterized from 3D seismic data. *Nature Geoscience*, *13*(5), 369–374. doi: 10.1038/s41561-020-0562-9

Klinkmüller, M., Schreurs, G., Rosenau, M., & Kemnitz, H. (2016). Properties of granular analogue model materials: A community wide survey. *Tectonophysics*, *684*, 23–38. doi: 10.1016/j.tecto.2016.01.017

Koge, H., Yamada, Y., Ohde, A., Bauville, A., Yamaguchi, A., & Ashi, J. (2018). Dynamic formation process of thick deformation zone on the shallow plate boundary fault of the Japan Trench: insight from analog experiments of half-graben subduction. *Progress in Earth and Planetary Science*, *5*(1), 69. doi: 10.1186/s40645-018-0230-5

Konstantinovskaia, E., & Malavieille, J. (2005). Erosion and exhumation in accretionary orogens: Experimental and geological approaches. *Geochemistry, Geophysics, Geosystems*, *6*, Q02006. doi: 10.1029/2004GC000794

Konstantinovskaya, E., & Malavieille, J. (2011). Thrust wedges with décollement levels and syntectonic erosion: A view from analog models. *Tectonophysics*, *502*(3–4), 336–350. doi: 10.1016/j.tecto.2011.01.020

Kopf, A. (2013). Effective strength of incoming sediments and its implications for plate boundary propagation: Nankai and Costa Rica as type examples of accreting vs. erosive convergent margins. *Tectonophysics*, *608*, 958–969. doi: 10.1016/j.tecto.2013.07.023

Kopp, C., Fruehn, J., Flueh, E., Reichert, C., Kukowski, N., Bialas, J., & Klaeschen, D. (2000). Structure of the Makran subduction zone from wide-angle and reflection seismic data. *Tectonophysics*, *329*, 171–191. doi: 10.1016/S0040-1951(00)00195-5

Kopp, H., & Kukowski, N. (2003). Backstop geometry and accretionary mechanics of the Sunda margin. *Tectonics*, *22*(6), 1072. doi: 10.1029/2002TC001420

Koyi, H. (1995). Mode of internal deformation in sand wedges. *Journal of Structural Geology*, *17*(2), 293–300. doi: 10.1016/0191-8141(94)00050-A

Krabbenhoeft, A., von Huene, R., Miller, J. J., & Klaeschen, D. (2021). Subducting oceanic basement roughness impacts on upper-plate tectonic structure and a backstop splay fault zone activated in the southern Kodiak aftershock region of the Mw 9.2, 1964 megathrust rupture, Alaska. *Geosphere*, *17*(2), 409–437. doi: 10.1130/GES02275.1

Kukowski, N., Greinert, J., & Henrys, S. (2010). Morphometric and critical taper analysis of the Rock Garden region, Hikurangi Margin, New Zealand: Implications for slope stability and potential tsunami generation. *Marine Geology*, *272*(1), 141–153. doi: 10.1016/j.margeo.2009.06.004

Kukowski, N., & Oncken, O. (2006). Subduction erosion: The "normal" mode of fore-arc material transfer along the Chilean margin? In O. Oncken et al. (Eds.), *The Andes: Active Subduction Orogeny* (pp. 217–236). Berlin, Heidelberg: Springer. doi: 10.1007/978-3-540-48684-8_10

Kukowski, N., von Huene, R., Malavieille, J., & Lallemand, S. (1994). Sediment accretion against a buttress beneath the Peruvian continental margin at 12° S as simulated with sandbox modeling. *Geologische Rundschau*, *83*(4), 822–831. doi: 10.1007/BF00251079

Lallemand, S., & Le Pichon, X. (1987). Coulomb wedge model applied to the subduction of seamounts in the Japan Trench. *Geology*, *15*(11), 1065–1069. doi: 10.1130/0091-7613(1987)15<1065:CWMATT>2.0.CO;2

Lallemand, S., Malavieille, J., & Calassou, S. (1992). Effects of oceanic ridge subduction on accretionary wedges: Experimental modeling and marine observations. *Tectonics*, *11*(6), 1301–1313. doi: 10.1029/92TC00637

Lallemand, S., Schnürle, P., & Malavieille, J. (1994). Coulomb theory applied to accretionary and nonaccretionary wedges: Possible causes for tectonic erosion and/or frontal accretion. *Journal of Geophysical Research*, *99*(B6), 12033–12055. doi: 10.1029/94JB00124

Lehner, F. K. (1986). Comments on "Noncohesive critical Coulomb wedges: An exact solution" by F. A. Dahlen. *Journal of Geophysical Research*, *91*(B1), 793–796. doi: 10.1029/JB091iB01p00793

Leroy, Y. M., & Maillot, B. (2016). Mechanics of accretionary prisms and fold-and-thrust belts based on limit analysis. *Advances in Geophysics*, *57*, 1–50. doi: 10.1016/bs.agph.2016.09.002

Lindsey, E. O., Mallick, R., Hubbard, J. A., Bradley, K. E., Almeida, R. V., Moore, J. D. P., ... Hill, E. M. (2021). Slip rate deficit and earthquake potential on shallow megathrusts. *Nature Geoscience*, *14*(5), 321–326. doi: 10.1038/s41561-021-00736-x

Lohrmann, J., Kukowski, N., Adam, J., & Oncken, O. (2003). The impact of analogue material properties on the geometry, kinematics, and dynamics of convergent sand wedges. *Journal of Structural Geology*, *25*(10), 1691–1711.

doi: 10.1016/S0191-8141(03)00005-1

Lohrmann, J., Kukowski, N., Krawczyk, C. M., Oncken, O., Sick, C., Sobiesiak, M., & Rietbro, A. (2006). Subduction channel evolution in brittle fore-arc wedges: A combined study with scaled sandbox experiments, seismological and reflection seismic data and geological field evidence. In O. Oncken et al. (Eds.), *The Andes: Active Subduction Orogeny* (pp. 237–262). Berlin, Heidelberg: Springer. doi: 10.1007/978-3-540-48684-8_11

Lv, X., Amelung, F., & Shao, Y. (2022). Widespread aseismic slip along the Makran megathrust triggered by the 2013 Mw 7.7 Balochistan Earthquake. *Geophysical Research Letters*, *49*(6), e2021GL097411. doi: 10.1029/2021GL097411

MacKay, M. E. (1995). Structural variation and landward vergence at the toe of the Oregon accretionary prism. *Tectonics*, *14*. doi: 10.1029/95TC02320

Maillot, B. (2013). A sedimentation device to produce uniform sand packs. *Tectonophysics*, *593*, 85–94. doi: 10.1016/j.tecto.2013.02.028

Maillot, B., & Koyi, H. (2006). Thrust dip and thrust refraction in fault-bend folds: analogue models and theoretical predictions. *Journal of Structural Geology*, *28*(1), 36–49. doi: 10.1016/j.jsg.2005.10.001

Maksymowicz, A. (2015). The geometry of the Chilean continental wedge: Tectonic segmentation of subduction processes off Chile. *Tectonophysics*, *659*, 183–196. doi: 10.1016/j.tecto.2015.08.007

Malavieille, J., Dominguez, S., Lu, C.-Y., Chen, C.-T., & Konstantinovskaya, E. (2019). Deformation partitioning in mountain belts: insights from analogue modelling experiments and the Taiwan collisional orogen. *Geological Magazine*, *158*(1), 84–103. doi: 10.1017/S0016756819000645

Mantilla-Pimiento, A. M., Jentzsch, G., Kley, J., & Alfonso-Pava, C. (2009). Configuration of the Colombian Caribbean Margin: Constraints from 2D Seismic Reflection data and Potential Fields Interpretation. In S. Lallemand & F. Funiciello (Eds.), *Subduction Zone Geodynamics* (pp. 247–272). Berlin, Heidelberg: Springer. doi: 10.1007/978-3-540-87974-9

Marshak, S., Haq, S. S. B., & Sen, P. (2019). Ramp initiation in fold-thrust belts: Insight from PIV analysis of sandbox models. *Journal of Structural Geology*, *118*, 308–323. doi: 10.1016/j.jsg.2018.11.006

Mary, B. C. L., Maillot, B., & Leroy, Y. M. (2013). Predicting orogenic wedge styles as a function of analogue erosion law and material softening. *Geochemistry, Geophysics, Geosystems*, *14*(10), 4523–4543. doi: 10.1002/ggge.20262

Massoli, D., Koyi, H. A., & Barchi, M. R. (2006). Structural evolution of a fold and thrust belt generated by multiple décollements: analogue models and natural examples from the Northern Apennines (Italy). *Journal of Structural Geology*, *28*(2), 185–199. doi: 10.1016/j.jsg.2005.11.002

McBeck, J. A., Cooke, M. L., Herbert, J. W., Maillot, B., & Souloumiac, P. (2017). Work optimization predicts accretionary faulting: An integration of physical and numerical experiments. *Journal of Geophysical Research: Solid Earth*, *122*(9), 7485–7505. doi: 10.1002/2017JB013931

Melnick, D. (2016). Rise of the central Andean coast by earthquakes straddling the Moho. *Nature Geoscience*, *9*(5), 401–407. doi: 10.1038/ngeo2683

Meng, Q., & Hodgetts, D. (2019). Structural styles and decoupling in stratigraphic sequences with double décollements during thin-skinned contractional tectonics: Insights from numerical modelling. *Journal of Structural Geology*, *127*, 103862. doi: 10.1016/j.jsg.2019.103862

Métois, M., Socquet, A., & Vigny, C. (2012). Interseismic coupling, segmentation and mechanical behavior of the central Chile subduction zone. *Journal of Geophysical Research*, *117*, B03406. doi: 10.1029/2011JB008736

Miyakawa, A., Noda, A., & Koge, H. (2022). Evolution of the geological structure and mechanical properties due to the collision of multiple basement topographic highs in a forearc accretionary wedge: insights from numerical simulations. *Progress in Earth and Planetary Science*, *9*(1), 1. doi: 10.1186/s40645-021-00461-4

Miyakawa, A., Yamada, Y., & Matsuoka, T. (2010). Effect of increased shear stress along a plate boundary fault on the formation of an out-of-sequence thrust and a break in surface slope within an accretionary wedge, based on numerical simulations. *Tectonophysics*, *484*, 127–138. doi: 10.1016/j.tecto.2009.08.037

Moore, G. F., Bangs, N. L., Taira, A., Kuramoto, S., Pangborn, E., & Tobin, H. J. (2007). Three-dimensional splay fault geometry and implications for tsunami generation. *Science*, *318*(5853), 1128–1131. doi: 10.1126/science.1147195

Moore, G. F., Boston, B. B., Strasser, M., Underwood, M. B., & Ratliff, R. A. (2015). Evolution of tectono-sedimentary systems in the Kumano Basin, Nankai Trough forearc. *Marine and Petroleum Geology*, *67*, 604–616. doi: 10.1016/j.marpetgeo.2015.05.032

Moore, G. F., Kanagawa, K., Strasser, M., Dugan, B., Maeda, L., Toczko, S., & Party, T. I. E. . S. (2014). IODP Expedition 338: NanTroSEIZE Stage 3: NanTroSEIZE plate boundary deep riser 2. *Scientific Drilling*, *17*, 1–12. doi: 10.5194/sd-17-1-2014

Moore, J. C., Klaus, A., Bangs, N. L., Bekins, B., Bücker, C. J., Brückmann, W., . . . Tokunaga, T. (1998). Consolidation patterns during initiation and evolution of a plate-boundary decollement zone: Northern Barbados accretionary prism. *Geology*, *26*(9), 811–814. doi: 10.1130/0091-7613(1998)026<0811:CPDIAE>2.3.CO;2

Moore, J. C., & Saffer, D. (2001). Updip limit of the seismogenic zone beneath the accretionary prism of southwest japan: An effect of diagenetic to low-grade metamorphic processes and increasing effective stress. *Geology*, *29*(2), 183-186. doi: 10.1130/0091-7613(2001)029<0183:ULOTSZ>2.0.CO;2

Morgan, J. K., & Bangs, N. L. (2017). Recognizing seamount-forearc collisions at accretionary margins: Insights from discrete numerical simulations. *Geology*, *45*(7), 635–638. doi: 10.1130/G38923.1

Morrow, C., Radney, B., & Byerlee, J. (1992). Frictional strength and the effective pressure law of montmorillonite and lllite clays. In B. Evans & T.-f. Wong (Eds.), *Fault mechanics and transport properties of rocks* (Vol. 51, pp. 69–88). Amsterdam, Netherlands: Elsevier. doi: 10.1016/S0074-6142(08)62815-6

Mulugeta, G., & Koyi, H. (1992). Episodic accretion and strain partitioning in a model sand wedge. *Tectonophysics*, *202*(2), 319–333. doi: 10.1016/0040-1951(92)90117-O

Naylor, M., & Sinclair, H. D. (2007). Punctuated thrust deformation in the context of doubly vergent thrust wedges: Implications for the localization of uplift and exhumation. *Geology*, *35*(6), 559–562. doi: 10.1130/G23448A.1

Newton, T. J., & Thomas, A. M. (2020). Stress orientations in the Nankai Trough constrained using seismic and aseismic slip. *Journal of Geophysical Research: Solid Earth*, *125*(7), e2020JB019841. doi: 10.1029/2020JB019841

Nicol, A., Mazengarb, C., Chanier, F., Rait, G., Uruski, C., & Wallace, L. (2007). Tectonic evolution of the active Hikurangi subduction margin, New Zealand, since the Oligocene. *Tectonics*, *26*, TC4002. doi: 10.1029/2006TC002090

Nieuwland, D. A., Urai, J. L., & Knoop, M. (2000). In-situ stress measurements in model experiments of tectonic faulting. In F. K. Lehner & J. L. Urai (Eds.), *Aspects of Tectonic Faulting* (pp. 155–167). Berlin, Heidelberg: Springer-Verlag. doi: 10.1007/978-3-642-59617-9_8

Noda, A. (2016). Forearc basins: Types, geometries, and relationships to subduction zone dynamics. *Geological Society of America Bulletin*, *128*(5–6), 879–895. doi: 10.1130/B31345.1

Noda, A., Graveleau, F., Witt, C., Frank, C., & Vendeville, B. (2023a). Data set for "Accretion cycles, structural evolution, and thrust activity in accretionary wedges with various décollement configurations: Insights from sandbox analog modeling" [Data set]. *Zenodo*. doi: 10.5281/zenodo.7397374

Noda, A., Graveleau, F., Witt, C., Frank, C., & Vendeville, B. (2023b). Supporting information for "Accretion cycles, structural evolution, and thrust activity in accretionary wedges with various décollement configurations: Insights from sandbox analog modeling". *Figshare*. Retrieved from `https://figshare.com/s/efb13bc30c1a76d937a7`

Noda, A., Koge, H., Yamada, Y., Miyakawa, A., & Ashi, J. (2020). Subduction of trench-fill sediments beneath an accretionary wedge: Insights from sandbox analogue experiments. *Geosphere*, *16*(4), 953–968. doi: 10.1130/GES02212.1

Okuda, H., Kitamura, M., Takahashi, M., & Yamaguchi, A. (2023). Frictional properties of the décollement in the shallow Nankai Trough: Constraints from friction experiments simulating in-situ conditions and implications for the seismogenic zone. *Earth and Planetary Science Letters*, *621*, 118357. doi: 10.1016/j.epsl.2023.118357

Okuma, Y., Noda, A., Koge, H., Yamada, Y., Yamaguchi, A., & Ashi, J. (2022). Surface friction of subducting seamounts influences deformation of the accretionary wedge. *Tectonophysics*, *845*, 229644. doi: 10.1016/j.tecto.2022.229644

Oncken, O., Boutelier, D., Dresen, G., & Schemmann, K. (2012). Strain accumulation controls failure of a plate boundary zone: Linking deformation of the Central Andes and lithosphere mechanics. *Geochemistry, Geophysics, Geosystems*, *13*(12), 1–22. doi: 10.1029/2012GC004280

Pajang, S., Khatib, M. M., Heyhat, M., Cubas, N., Bessiere, E., Letouzey, J., …

Le Pourhiet, L. (2022). The distinct morphologic signature of underplating and seamounts in accretionary prisms, insights from thermomechanical modeling applied to Coastal Iranian Makran. *Tectonophysics*, *845*, 229617. doi: 10.1016/j.tecto.2022.229617

Pan, B. (2009). Reliability-guided digital image correlation for image deformation measurement. *Applied Optics*, *48*(8), 1535–1542. doi: 10.1364/AO.48.001535

Pan, B., Asundi, A., Xie, H., & Gao, J. (2009). Digital image correlation using iterative least squares and pointwise least squares for displacement field and strain field measurements. *Optics and Lasers in Engineering*, *47*(7), 865–874. doi: 10.1016/j.optlaseng.2008.10.014

Parvaiz, S., Ali, A., Javed, F., & Shah, M. A. (2022). Deformational pattern and seismogenic potential of the eastern Makran subduction zone. *Journal of Asian Earth Sciences*, *235*, 105298. doi: 10.1016/j.jseaes.2022.105298

Pedley, K. L., Barnes, P. M., Pettinga, J. R., & Lewis, K. B. (2010). Seafloor structural geomorphic evolution of the accretionary frontal wedge in response to seamount subduction, Poverty Indentation, New Zealand. *Marine Geology*, *270*, 119–138. doi: 10.1016/j.margeo.2009.11.006

Perrin, C., Clemenzi, L., Malavieille, J., Molli, G., Taboada, A., & Dominguez, S. (2013). Impact of erosion and décollements on large-scale faulting and folding in orogenic wedges: Analogue models and case studies. *Journal of the Geological Society, London*, *170*(6), 893–904. doi: 10.1144/jgs2013-012

Platt, J. P. (1986). Dynamics of orogenic wedges and the uplift of high-pressure metamorphic rocks. *Geological Society of America Bulletin*, *97*(9), 1037–1053.

Platt, J. P. (1988). The mechanics of frontal imbrication: a first-order analysis. *Geologische Rundschau*, *77*(2), 577–589. doi: 10.1007/BF01832399

Ramberg, H. (1981). *Gravity, Deformation and the Earth's Crust* (2nd ed.). New York: Academic Press.

Reece, R. S., Gulick, S. P. S., Horton, B. K., Christeson, G. L., & Worthington, L. L. (2011). Tectonic and climatic influence on the evolution of the Surveyor Fan and Channel system, Gulf of Alaska. *Geosphere*, *7*(4), 830–844. doi: 10.1130/GES00654.1

Ritter, M. C., Leever, K., Rosenau, M., & Oncken, O. (2016). Scaling the sandbox—Mechanical (dis) similarities of granular materials and brittle rock. *Journal of Geophysical Research: Solid Earth*, *121*, 6863–6879. doi: 10.1002/2016JB012915

Ritter, M. C., Santimano, T., Rosenau, M., Leever, K., & Oncken, O. (2018). Sandbox rheometry: Co-evolution of stress and strain in Riedel–and Critical Wedge–experiments. *Tectonophysics*, *722*, 400–409. doi: 10.1016/j.tecto.2017.11.018

Rodríguez, I., Bulnes, M., Poblet, J., Masini, M., & Flinch, J. (2021). Structural style and evolution of the offshore portion of the Sinu Fold Belt (South Caribbean Deformed Belt) and adjacent part of the Colombian Basin. *Marine and Petroleum Geology*, *125*, 104862. doi: 10.1016/j.marpetgeo.2020.104862

Roy, S., Bose, S., & Saha, P. (2020). Spatial variations of ductile strain in fold-and-thrust belts: From model to nature. *Journal of Structural Geology*, *134*, 104012. doi: 10.1016/j.jsg.2020.104012

Ruh, J. B. (2016). Submarine landslides caused by seamounts entering accretionary wedge systems. *Terra Nova*, *28*(3), 163–170. doi: 10.1111/ter.12204

Ruh, J. B. (2020). Numerical modeling of tectonic underplating in accretionary wedge systems. *Geosphere*, *16*(6), 1385–1407. doi: 10.1130/GES02273.1

Ruh, J. B., Gerya, T., & Burg, J.-P. (2013). High-resolution 3D numerical modeling of thrust wedges: Influence of décollement strength on transfer zones. *Geochemistry, Geophysics, Geosystems*, *14*(4), 1131–1155. doi: 10.1002/ggge.20085

Ruh, J. B., Kaus, B. J. P., & Burg, J.-P. (2012). Numerical investigation of deformation mechanics in fold-and-thrust belts: Influence of rheology of single and multiple décollements. *Tectonics*, *31*, TC3005. doi: 10.1029/2011TC003047

Ruh, J. B., Sallarès, V., Ranero, C. R., & Gerya, T. (2016). Crustal deformation dynamics and stress evolution during seamount subduction: High-resolution 3-D numerical modeling. *Journal of Geophysical Research: Solid Earth*, *121*, 6880–6902. doi: 10.1002/2016JB013250

Saffer, D. M., Lockner, D. A., & McKiernan, A. (2012). Effects of smectite to illite transformation on the frictional strength and sliding stability of intact marine mudstones. *Geophysical Research Letters*, *39*(11), L11304. doi: 10.1029/2012GL051761

Saha, P., Bose, S., & Mandal, N. (2016). Sandbox modelling of sequential thrusting in a mechanically two-layered system and its implications in fold-and-thrust belts. *Journal of Geodynamics*, *100*, 104–114. doi: 10.1016/j.jog.2016.05.005

Saillard, M., Audin, L., Rousset, B., Avouac, J. P., Chlieh, M., Hall, S. R., … Farber, D. L. (2017). From the seismic cycle to long-term deformation: linking seismic coupling and Quaternary coastal geomorphology along the Andean megathrust. *Tectonics*, *36*(2), 241–256. doi: 10.1002/2016TC004156

Schellart, W. P. (2000). Shear test results for cohesion and friction coefficients for different granular materials: scaling implications for their usage in analogue modelling. *Tectonophysics*, *324*(1–2), 1–16. doi: 10.1016/S0040-1951(00)00111-6

Schellart, W. P., & Strak, V. (2016). A review of analogue modelling of geodynamic processes: Approaches, scaling, materials and quantification, with an application to subduction experiments. *Journal of Geodynamics*, *100*, 7–32. doi: 10.1016/j.jog.2016.03.009

Schlüter, H. U., Prexl, A., Gaedicke, C., Roeser, H., Reichert, C., Meyer, H., & von Daniels, C. (2002). The Makran accretionary wedge: sediment thicknesses and ages and the origin of mud volcanoes. *Marine Geology*, *185*(3–4), 219–232. doi: 10.1016/S0025-3227(02)00192-5

Schulze, D. (1994). Development and application of a novel ring shear tester [entwicklung und anwendung eines neuartigen ringschergeraetes]. *Aufbereitungs-Technik*, *35*(10), 524–535.

Schumann, K., Behrmann, J. H., Stipp, M., Yamamoto, Y., Kitamura, Y., & Lempp, C. (2014). Geotechnical behavior of mudstones from the Shimanto and Boso accretionary complexes, and implications for the Nankai accretionary prism. *Earth, Planets and Space*, *66*(129). doi: 10.1186/1880-5981-66-129

Schwarze, C. O., & Kukowski, N. (2022). Décollement strength and mechanical segmentation along the frontal wedge of the Hikurangi convergent margin (New Zealand): Insights from critical taper analysis. *Tectonophysics*, *844*, 229622. doi: 10.1016/j.tecto.2022.229622

Simpson, G. D. H. (2010). Formation of accretionary prisms influenced by sediment subduction and supplied by sediments from adjacent continents. *Geology*, *38*(2), 131–134. doi: 10.1130/G30461.1

Simpson, G. D. H. (2011). Mechanics of non-critical fold–thrust belts based on finite element models. *Tectonophysics*, *499*(1), 142–155. doi: 10.1016/j.tecto.2011.01.004

Singh, S. C., Hananto, N., Mukti, M., Robinson, D. P., Das, S., Chauhan, A., ... Harjono, H. (2011). Aseismic zone and earthquake segmentation associated with a deep subducted seamount in Sumatra. *Nature Geoscience*, *4*(5), 308–311. doi: 10.1038/ngeo1119

Smith, G., McNeill, L., Henstock, T. J., & Bull, J. (2012). The structure and fault activity of the Makran accretionary prism. *Journal of Geophysical Research*, *117*, B07407. doi: 10.1029/2012JB009312

Souloumiac, P., Krabbenhøft, K., Leroy, Y. M., & Maillot, B. (2010). Failure in accretionary wedges with the maximum strength theorem: numerical algorithm and 2D validation. *Computational Geosciences*, *14*(4), 793–811. doi: 10.1007/s10596-010-9184-4

Souloumiac, P., Leroy, Y. M., Maillot, B., & Krabbenhøft, K. (2009). Predicting stress distributions in fold-and-thrust belts and accretionary wedges by optimization. *Journal of Geophysical Research*, *114*, B09404. doi: 10.1029/2008JB005986

Souloumiac, P., Maillot, B., & Leroy, Y. M. (2012). Bias due to side wall friction in sand box experiments. *Journal of Structural Geology*, *35*, 90–101. doi: 10.1016/j.jsg.2011.11.002

Stockmal, G. S., Beaumont, C., Nguyen, M., & Lee, B. (2007). Mechanics of thin-skinned fold-and-thrust belts: Insights from numerical models. In J. W. Sears, T. A. Harms, & C. A. Evenchick (Eds.), *Whence the Mountains? Inquiries into the Evolution of Orogenic Systems* (Vol. 433, pp. 63–98). Boulder, Colorado, USA: Geological Society of America. doi: 10.1130/2007.2433(04)

Storti, F., Salvini, F., & McClay, K. (2000). Synchronous and velocity-partitioned thrusting and thrust polarity reversal in experimentally produced, doubly-vergent thrust wedges: Implications for natural orogens. *Tectonics*, *19*, 378–396. doi: 10.1029/1998TC001079

Strasser, M., Moore, G. F., Kimura, G., Kitamura, Y., Kopf, A. J., Lallemant, S., ... Zhao, X. (2009). Origin and evolution of a splay fault in the Nankai accretionary wedge. *Nature Geoscience*, *2*(9), 648–652. doi: 10.1038/NGEO609

Sun, C., Li, Z., Wu, S., He, Z., Zhao, S., & Wang, P. (2021). Structural significance of the mid-level décollement within the western Sichuan fold-and-thrust belt (WSFTB), insights from sandbox modeling. *Frontiers in Earth Science*, *9*, 631405. doi: 10.3389/feart.2021.631405

Sun, T., Saffer, D., & Ellis, S. (2020). Mechanical and hydrological effects of seamount subduction on megathrust stress and slip. *Nature Geoscience*, *13*(3), 249–255. doi: 10.1038/s41561-020-0542-0

Suppe, J. (2007). Absolute fault and crustal strength from wedge tapers. *Geology*, *35*(12), 1127–1130. doi: 10.1130/G24053A.1

Terzaghi, K. (1943). *Theoretical Soil Mechanics*. New York: John Wiley.

Tobin, H. J., Saffer, D. M., Castillo, D. A., & Hirose, T. (2022). Direct constraints on in situ stress state from deep drilling into the Nankai subduction zone, Japan. *Geology*, *50*(11), 1229–1233. doi: 10.1130/G49639.1

van Burkalow, A. (1945). Angle of repose and angle of sliding friction: An experimental study. *Geological Society of America Bulletin*, *56*(6), 669–707. doi: 10.1130/0016-7606(1945)56[669:AORAAO]2.0.CO;2

von Hagke, C., Oncken, O., & Evseev, S. (2014). Critical taper analysis reveals lithological control of variations in detachment strength: An analysis of the Alpine basal detachment (Swiss Alps). *Geochemistry, Geophysics, Geosystems*, *15*(1), 176–191. doi: 10.1002/2013GC005018

Wallace, L. M., Barnes, P. M., Beavan, J., Van Dissen, R., Litchfield, N., Mountjoy, J., … Pondard, N. (2012). The kinematics of a transition from subduction to strike-slip: An example from the central New Zealand plate boundary. *Journal of Geophysical Research*, *117*, B02405. doi: 10.1029/2011JB008640

Wang, K., & Bilek, S. L. (2011). Do subducting seamounts generate or stop large earthquakes? *Geology*, *39*(9), 819–822. doi: 10.1130/G31856.1

Wang, K., & Hu, Y. (2006). Accretionary prisms in subduction earthquake cycles: The theory of dynamic Coulomb wedge. *Journal of Geophysical Research*, *111*, B06410. doi: 10.1029/2005JB004094

Watson, S. J., Mountjoy, J. J., Barnes, P. M., Crutchley, G. J., Lamarche, G., Higgs, B., … Pecher, I. A. (2019). Focused fluid seepage related to variations in accretionary wedge structure, Hikurangi margin, New Zealand. *Geology*, *48*(1), 56–61. doi: 10.1130/G46666.1

Weiss, J. R., Brooks, B. A., Arrowsmith, J. R., & Vergani, G. (2015). Spatial and temporal distribution of deformation at the front of the Andean orogenic wedge in southern Bolivia. *Journal of Geophysical Research: Solid Earth*, *120*(3), 1909–1931. doi: 10.1002/2014JB011763

Yagupsky, D. L., Brooks, B. A., Whipple, K. X., Duncan, C. C., & Bevis, M. (2014). Distribution of active faulting along orogenic wedges: Minimum-work models and natural analogue. *Journal of Structural Geology*, *66*, 237–247. doi: 10.1016/j.jsg.2014.05.025

Yáñez-Cuadra, V., Ortega-Culaciati, F., Moreno, M., Tassara, A., Krumm-Nualart, N., Ruiz, J., ... Benavente, R. (2022). Interplate coupling and seismic potential in the Atacama seismic gap (Chile): Dismissing a rigid Andean sliver. *Geophysical Research Letters*, *49*(11), e2022GL098257. doi: 10.1029/2022GL098257

Yokota, Y., Ishikawa, T., Watanabe, S.-i., Tashiro, T., & Asada, A. (2016). Seafloor geodetic constraints on interplate coupling of the Nankai Trough megathrust zone. *Nature*, *534*(7607), 374–377. doi: 10.1038/nature17632

Zhang, Z., Zhang, H., Wang, L., Cheng, H., & Shi, Y. (2019). Late Cenozoic structural deformation and evolution of the central-southern Longmen Shan fold-and-thrust belt, China: Insights from numerical simulations. *Journal of Asian Earth Sciences*, *176*, 88–104. doi: 10.1016/j.jseaes.2019.01.026

Figure caption

Figure 1 Natural examples of modern accretionary wedges with various décollement features. (a) Single décollement in the accretionary wedge of the Southern Caribbean Deformation Belt (Mantilla-Pimiento et al., 2009; Rodríguez et al., 2021). (b) Accretionary wedge dominated by both frontal and basal accretion (underplating) in association with landward stepping down of the décollement level at the Makran margin (Burg et al., 2013; Burg, 2018; Grando & McClay, 2007; C. Kopp et al., 2000). (c) Accretionary wedge deformed by subduction of a seamount at the Hikurangi margin (Barnes et al., 2002, 2010; Nicol et al., 2007; Watson et al., 2019). (d) Accretionary wedge segmented by megasplay faults, being considered a double-décollement accretionary wedge at the Nankai margin (G. F. Moore et al., 2014; Tobin et al., 2022). Note that the colors are used to aid visibility, and that areas of the same color in the different accretionary wedges do not represent the same lithology.

Figure 2 (a) The experimental set-up used in this study. The dimensions of the tank are 1890 mm long × 315 mm high × 300 mm wide. The red arrow indicates the direction of the shortening. (b–e) Modeling set-ups. (b) Type 1: continuous single décollement model. The 25 mm-thick sand layer covers a 10 mm-thick glass microbead layer. (c) Type 2: continuous double décollement model. A 5 mm-thick glass microbead layer was placed in the middle of the incoming sediment layer. (d) Type 3: discontinuous single décollement model. A 90 mm-wide sand mound disrupts the continuity of the basal microbead layer. (e) Type 4: discontinuous double décollement model. Asterisks (*) indicate the models used for the DIC analysis.

Figure 3 Schematic illustrations of the measurements of the geometrical and kinematic parameters. (a) The coordinate system for the geometrical parameters. The origin was assigned at the toe of the proto-wedge in the initial stage. (b) The geometrical parameters include the wedge width, height, and slope (α). The slope was measured between the deformation front (P_0) and the highest point on the wedge (P_1). (c) The top (blue line) and bottom (black line) measurement zones for the normalized horizontal displacements ($\hat{u}$) at the top ($\hat{u}_{\mathrm{top}}$) and at the bottom ($\hat{u}_{\mathrm{bottom}}$), respectively. (d) The top (blue line) and bottom (black line) measurement zones for the normalized maximum shear strains ($\hat{\varepsilon}_{\max}$) at the top ($\hat{\varepsilon}_{\max(\mathrm{top})}$) and the bottom ($\hat{\varepsilon}_{\mathrm{max(bottom)}}$), respectively. The positions of the lines are the same as those for $\hat{u}$. Active forethrusts and backthrusts are shown as orange to red zones and blue to purple zones, respectively. (e) Dips $\delta_{\mathrm{f(init)}}$ and δ_{b} are the angles of a set of conjugate faults when a new frontal thrust initiates in front of the previous deformation front. $\delta_{\mathrm{f(final)}}$ is the dip of the trailing previously formed frontal thrust. The length of a new ramp is the width between the toe of the previous deformation front and the new one.

Figure 4 Plots of the geometrical parameters; (a) width; (b) height; (c) slope. The right and left columns are the type 1–2 and 3–4 models, respectively. Vertical dashed lines in the right column indicate the onset of sand mound subduction. Horizontal lines of α_{case1}, α_{case2}, and α_{case3} in (c) correspond to the critical slope angles for cases 1–3 in Figure S1, respectively. Labels $F_{\#}$ indicate the timing of the emergence of deeply rooted forethrusts. The theoretical width and height of the wedge, and the critical zones of the slope were obtained as shown in Supporting Information (Figure S2). The geometrical parameters of all the models are shown in Figure S3.

Figure 5 Final stacking patterns of the models. Numbered faults are deeply rooted forethrusts.

Figure 6 Sequential images of normalized horizontal ($\hat{u}$; left column) and vertical ($\hat{v}$; right column) displacement showing an accretion cycle. (a) Type 1 model (M06). (b) Type 2 model (M04). DIC images without interpretations are shown in Figures S8 and S9.

Figure 7 Comparison of the accretion cycles between the type 1 (left row) and type 2 (right row) models. (a) Normalized horizontal displacement in the top measurement zone ($\hat{u}_{\mathrm{top}}$ from Figure S5). (b) Normalized horizontal displacement in the bottom measurement zone ($\hat{u}_{\mathrm{bottom}}$ from Figure S5). (c) The ratio of normalized horizontal displacement at the top to the bottom $\hat{u}_{\mathrm{top}}/\hat{u}_{\mathrm{bottom}}$ (Figure S5). (d) Normalized vertical displacement ($\hat{v}$ from Figure S6). (e) Maximum shear strain in the top measurement zone ($\hat{\varepsilon}_{\mathrm{max(top)}}$ from Figure S7). White and black arrows indicate major out-of-sequence thrusts and reactivated thrusts, respectively. The extracted intervals are the shortening length L_s = 800–1000 mm for the type 1 model (M06) and L_s = 630–800 mm for the type 2 model (M04).

Figure 8 Interpreted DIC images for the (a) type 3 and (b) type 4 models. The left and right columns are normalized horizontal and vertical displacements, respectively. The black area in each image shows the location of the sand mound. Raw DIC images without interpretations are shown in Figures S10 and S11.

Figure 9 Comparison of the sand mound subduction between the type 3 (left row) and type 4 (right row) models. (a) Normalized horizontal displacement in the top measurement zone ($\hat{u}_{\mathrm{top}}$ from Figure S5). (b) Normalized horizontal displacement in the bottom measurement zone ($\hat{u}_{\mathrm{bottom}}$ from Figure S5). (c) The ratio of normalized horizontal displacement at the top to the bottom $\hat{u}_{\mathrm{top}}/\hat{u}_{\mathrm{bottom}}$ (Figure S5). (d) Normalized vertical displacement ($\hat{v}$ from Figure S6). (e) Maximum shear strain in the top measurement zone ($\hat{\varepsilon}_{\mathrm{max(top)}}$ from Figure S7). White and black arrows indicate major out-of-sequence thrusts and reactivated thrusts, respectively. The meshed areas indicate the traces of the subducting sand mound. The extracted intervals are the shortening length L_s = 300–800 mm for both type 3 (M08) and type 4 (M10) models.

Figure 10 Conceptual models of an accretion cycle for the continuous single décollement model. Solid and open circles at the bottom of the wedge are the reference points used to calculate the wedge and detachment strengths in Figures 11 and 12. Gray shading in the bands below the wedge indicate the degree of coupling between the basal plastic film and wedge; black and white colors mean completely coupled and decoupled, respectively. ϕ'_{in} and ϕ'_{out} are the effective friction angles of the inner and outer parts of the wedge, respectively. α'_{out} is the effective slope angle at the point that a new frontal forethrust emerges. $\alpha_{\phi_{\mathrm{peak}}}$ and $\alpha_{\phi_{\mathrm{dynamic}}}$ are the theoretical taper angles in cases 1 and 2, respectively (Figure S1).

Figure 11 (a) A sketch of an accretionary wedge showing the parameters related to the wedge and detachment strengths. Subscripts “in” and “out” represent the inner and outer parts of the wedge, respectively. H = height; L = length; α = slope angle; ϕ = internal friction angle; σ_1 = maximum principal stress; σ_3 = minimum principal stress; σ_n = normal stress; τ_b = basal shear stress; δ_{f} and δ_{b} = dip angles of the forethrust and backthrust, respectively. (b) Effective internal friction angle (ϕ'). The left and right columns are the inner and outer parts of the wedge, respectively. Horizontal lines of ϕ_{peak} and ϕ_{dynamic} are the measured friction angles of the sand used in this study. (c) Surface slope (α). Solid and dashed lines in the right column are the effective (α'_{out}) and apparent (α_{out}) slope of the wedge, respectively. The effective slope ($\alpha'_{\mathrm{out}} = 4°$) is estimated from $\delta_{\mathrm{f(init)}}$ and δ_{b} Figure S12b. Horizontal lines of $\alpha_{\phi_{\mathrm{peak}}}$ and $\alpha_{\phi_{\mathrm{dynamic}}}$ are the theoretical taper angles for the friction angles of sand (Figure S1). (d–f) Calculated geometric and kinematic trends based on the assumed friction angles (ϕ_{peak} and ϕ_{dynamic}) and slopes (α_{in} and α'_{out}). (d) Wedge length L (solid line) and height H (dashed line). (e) Differential stress $(\sigma_1 - \sigma_3)/2$ (solid line) and basal shear stress τ_b (dashed line). (f) Wedge strength (W_s) and basal detachment strength (F_s).

Figure 12 Trends of the wedge and detachment strengths at locations in the outer and inner parts of the wedge (Figure 11). Thick dashed and solid lines show the trends of the strengths from phase 1 to 4 in the outer and inner parts of the wedge, respectively. The two lines for $\alpha_{\phi_{\mathrm{peak}}}$ and $\alpha_{\phi_{\mathrm{dynamic}}}$ are the theoretical lines of the strengths calculated from $\alpha = F_s/(1 + W_s)$ (Eq. 2a in Suppe, 2007). The lower right and upper left corners in the diagram indicate that the wedge is decoupled and coupled to the basal detachment, respectively.

Figure 13 Mohr diagrams using the pole projection method (P-pole; Terzaghi, 1943). (a) Type 1 model. (b) Type 2 model. $\delta_{\mathrm{f(init)}}$ = dip of a new frontal forethrust when it is nucleated (Figure S13d); $\delta_{\mathrm{f(final)}}$ = dip of the trailing previously formed frontal forethrust (Figure S13e); δ_{b} = dip of the backthrust in a conjugate set with the new frontal forethrust (Figure S13c); α' = effective slope angle at which a new frontal thrust emerges (Figure S12b); $\alpha_{\phi_{\mathrm{case1}}}$ and α_{case3} = theoretical slope angles (Figure S1); ϕ'_{peak} = effective peak friction angle when a new frontal thrust initiates; ϕ'_{stable} = effective stable friction angle; ϕ'_{base} = effective stable friction angle at the basal interface; P = position of the pole on the circle. Green areas indicate the ranges of the effective internal friction angles (ϕ'_{stable}) of the incoming sediments while the frontal forethrust is active.

Figure 14 A comparison between our discontinuous basal décollement models and other published models. (a) Type 3 model (M08). (b) Type 4 model (M10). (c) A sandbox model for subduction of a partially buried seamount (Dominguez et al., 2000). The rigid seamount is fixed to the lower plate. (d) A model of buried seamount subduction proposed from a study offshore of Kodiak Island (Frederik et al., 2020). DF = deformation front; PTZ = proto-thrust zone; OOST = out-of-sequence thrust.

Table 1. Material properties used in this study.

Property	Sand (GA39)	Glass microbeads
Grain size (μm)	115	70–110
Bulk density (kg/m^{-3})	1426	1660
Friction angle (peak)	35.5±0.2	26.6±0.1
Friction angle (reactivation)	35.5±0.1	26.1±0.05
Friction angle (dynamic)	30.8±0.04	24.0±0.06
Cohesion (peak) (Pa)	24±12	31±6
Cohesion (reactivation) (Pa)	36±6	42±3
Cohesion (dynamic) (Pa)	54±2	30±4
Strain softening* (undeformed material) (%)	19.8[a]	12.3[a]
Strain softening (shear zone reactivation) (%)	19.6[b]	9.9[b]

*Strain softening expresses the percentage difference between peak friction and dynamic stable friction.

[a]: Ratio of the friction angles, (peak strength−dynamic strength)/dynamic strength in percent.

[b]: Ratio of the friction angles, (static strength−dynamic strength)/dynamic strength in percent.

All data of the frictional angle and cohesion were measured using a Schulze ring shear tester at the Helmholtz Centre Potsdam, German Research Centre for Geosciences GFZ (Klinkmüller et al., 2016; Lohrmann et al., 2003; Schulze, 1994).

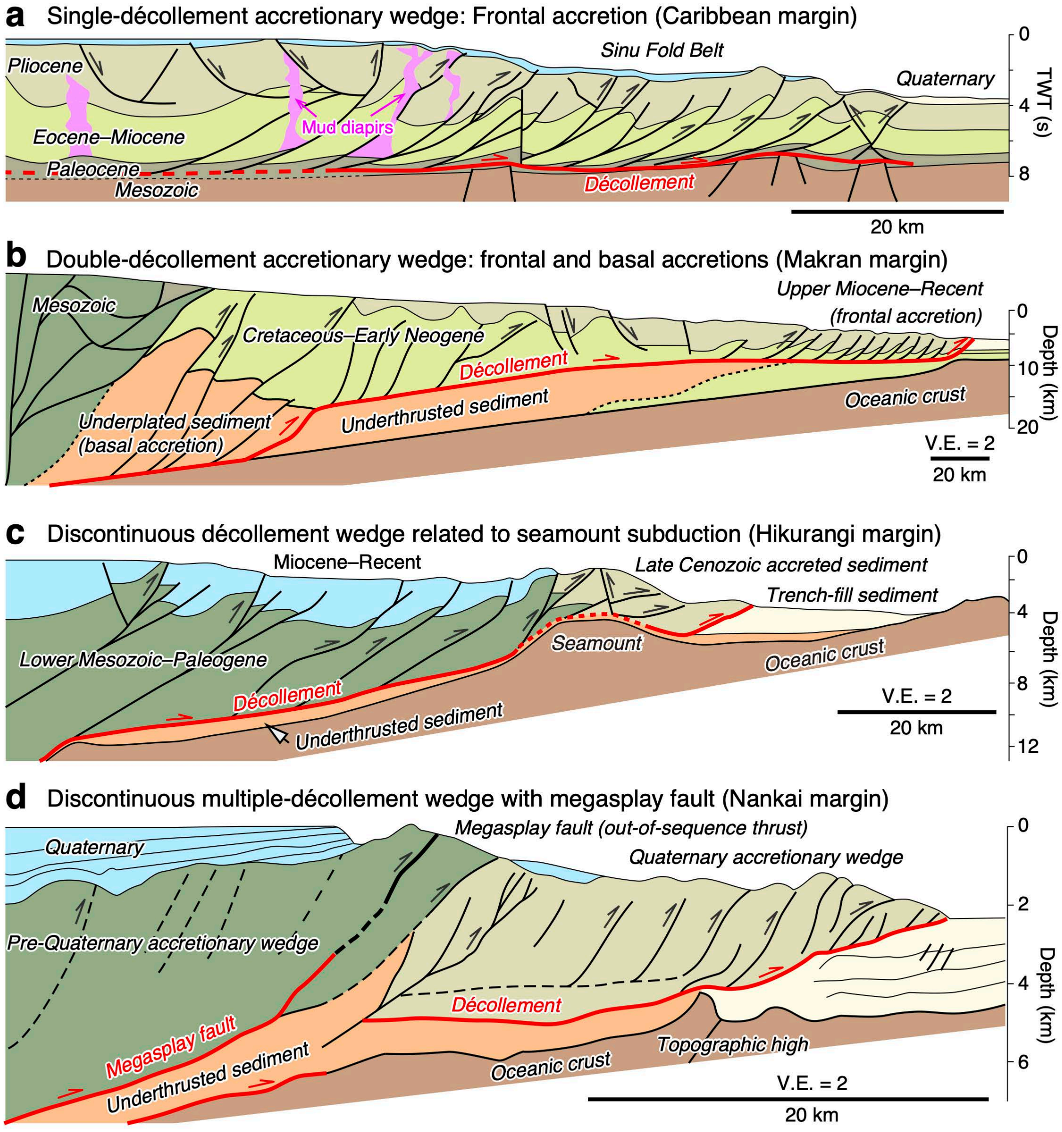
a Single-décollement accretionary wedge: Frontal accretion (Caribbean margin)
Pliocene
Sinu Fold Belt
Quaternary
Eocene–Miocene
Mud diapirs
Paleocene
Mesozoic
Décollement
TWT (s)
0
4
8
20 km
b Double-décollement accretionary wedge: frontal and basal accretions (Makran margin)
Mesozoic
Cretaceous–Early Neogene
Upper Miocene–Recent (frontal accretion)
Décollement
Underplated sediment (basal accretion)
Underthrusted sediment
Oceanic crust
Depth (km)
0
10
20
V.E. = 2
20 km
c Discontinuous décollement wedge related to seamount subduction (Hikurangi margin)
Miocene–Recent
Late Cenozoic accreted sediment
Trench-fill sediment
Lower Mesozoic–Paleogene
Seamount
Oceanic crust
Décollement
Underthrusted sediment
V.E. = 2
20 km
Depth (km)
0
4
8
12
d Discontinuous multiple-décollement wedge with megasplay fault (Nankai margin)
Quaternary
Megasplay fault (out-of-sequence thrust)
Quaternary accretionary wedge
Pre-Quaternary accretionary wedge
Décollement
Megasplay fault
Underthrusted sediment
Oceanic crust
Topographic high
V.E. = 2
20 km
Depth (km)
0
2
4
6

Figure 1.

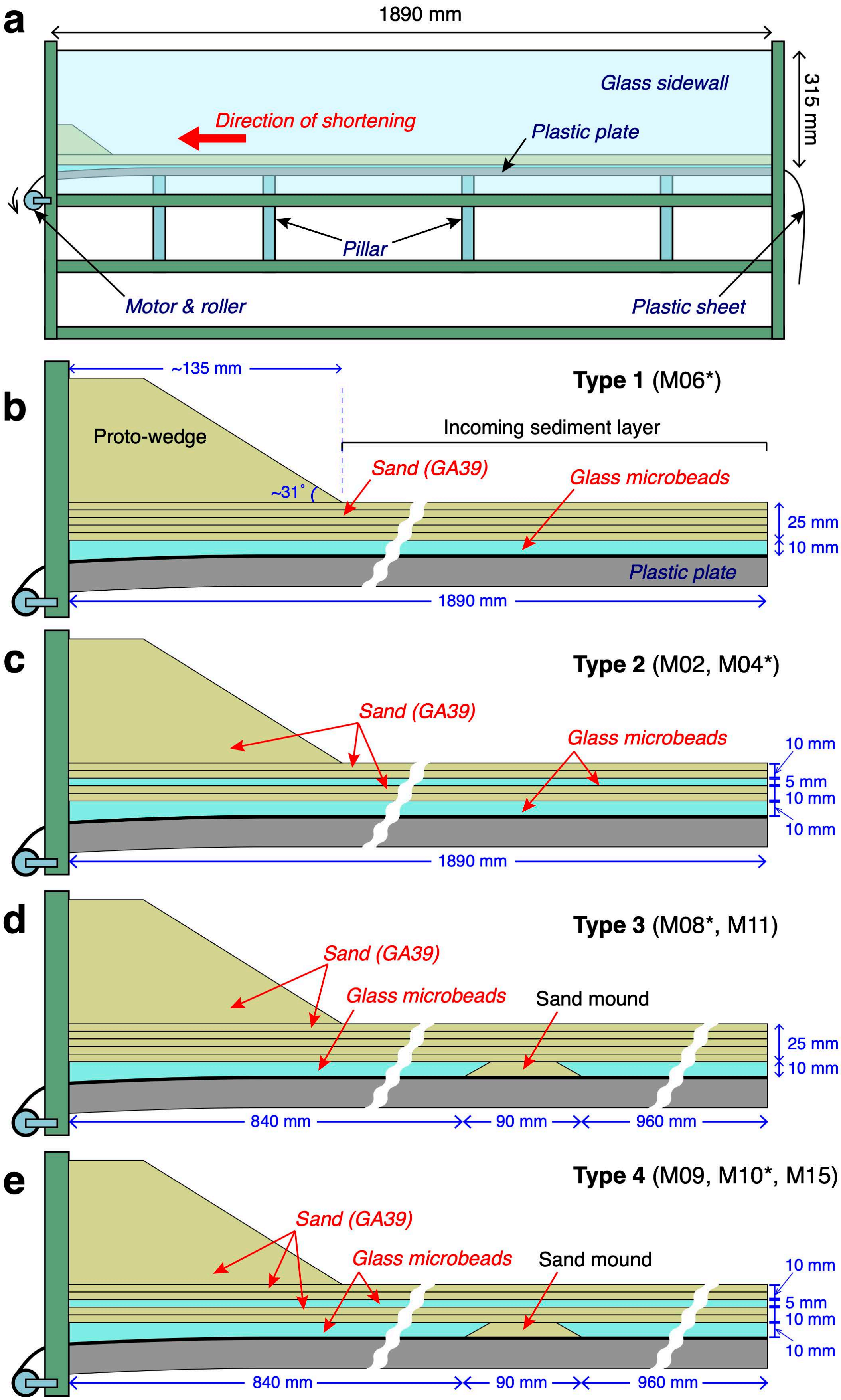
a
1890 mm
315 mm
Glass sidewall
Direction of shortening
Plastic plate
Pillar
Motor & roller
Plastic sheet
b
~135 mm
Type 1 (M06*)
Proto-wedge
Incoming sediment layer
Sand (GA39)
Glass microbeads
~31°
25 mm
10 mm
Plastic plate
1890 mm
c
Type 2 (M02, M04*)
Sand (GA39)
Glass microbeads
10 mm
5 mm
10 mm
10 mm
1890 mm
d
Type 3 (M08*, M11)
Sand (GA39)
Glass microbeads
Sand mound
25 mm
10 mm
840 mm
90 mm
960 mm
e
Type 4 (M09, M10*, M15)
Sand (GA39)
Glass microbeads
Sand mound
10 mm
5 mm
10 mm
10 mm
840 mm
90 mm
960 mm

Figure 2.

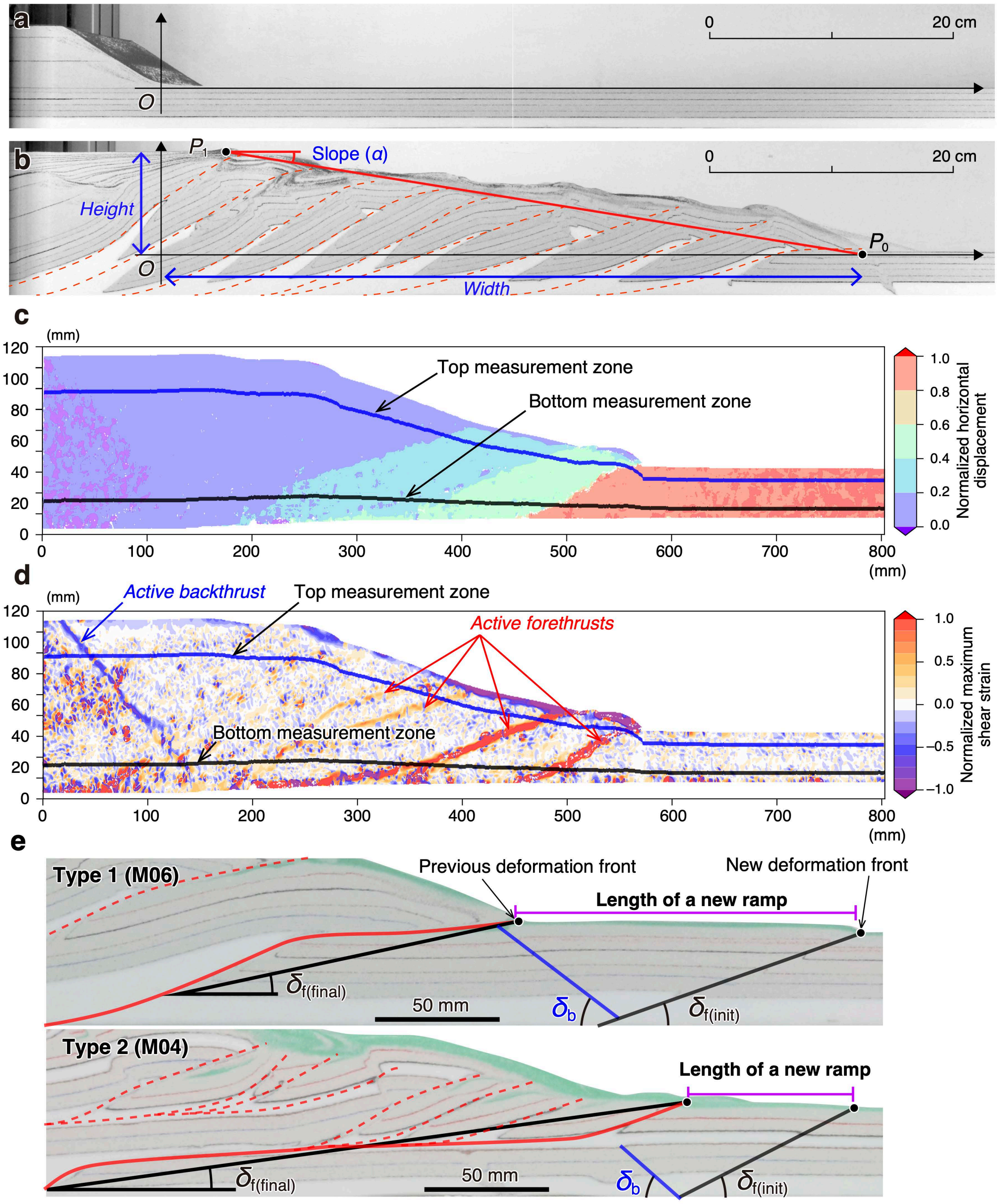
a
O
0
20 cm
b
P_1
Slope (α)
Height
O
Width
P_0
0
20 cm
c
(mm)
120
100
80
60
40
20
0
Top measurement zone
Bottom measurement zone
0
100
200
300
400
500
600
700
800
(mm)
1.0
0.8
0.6
0.4
0.2
0.0
Normalized horizontal displacement
d
(mm)
Active backthrust
Top measurement zone
Active forethrusts
Bottom measurement zone
120
100
80
60
40
20
0
0
100
200
300
400
500
600
700
800
(mm)
1.0
0.5
0.0
−0.5
−1.0
Normalized maximum shear strain
e
Type 1 (M06)
Previous deformation front
New deformation front
Length of a new ramp
$\delta_{f(final)}$
50 mm
δ_b
$\delta_{f(init)}$
Type 2 (M04)
Length of a new ramp
$\delta_{f(final)}$
50 mm
δ_b
$\delta_{f(init)}$

Figure 3.

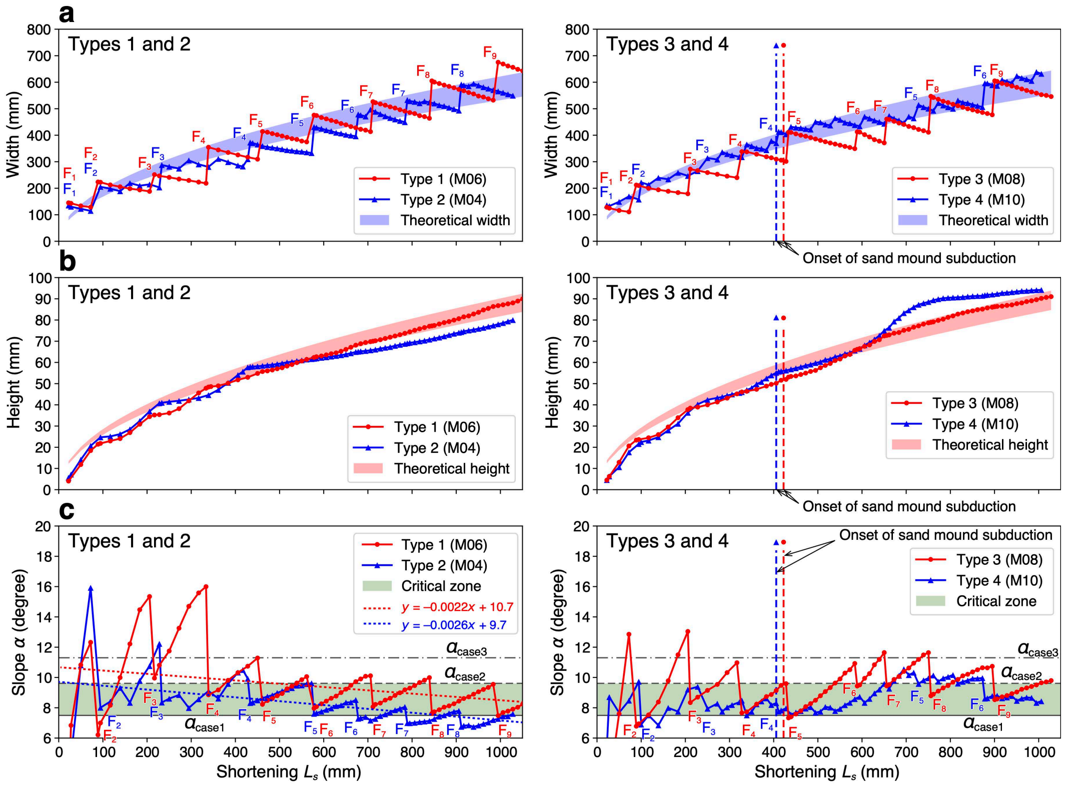
a
Types 1 and 2
Types 3 and 4
Width (mm)
Type 1 (M06)
Type 2 (M04)
Type 3 (M08)
Type 4 (M10)
Theoretical width
Onset of sand mound subduction
b
Height (mm)
Theoretical height
c
Slope α (degree)
Critical zone
y = −0.0022x + 10.7
y = −0.0026x + 9.7
α_{case1}
α_{case2}
α_{case3}
F_1 F_2 F_3 F_4 F_5 F_6 F_7 F_8 F_9
Shortening L_s (mm)

Figure 4.

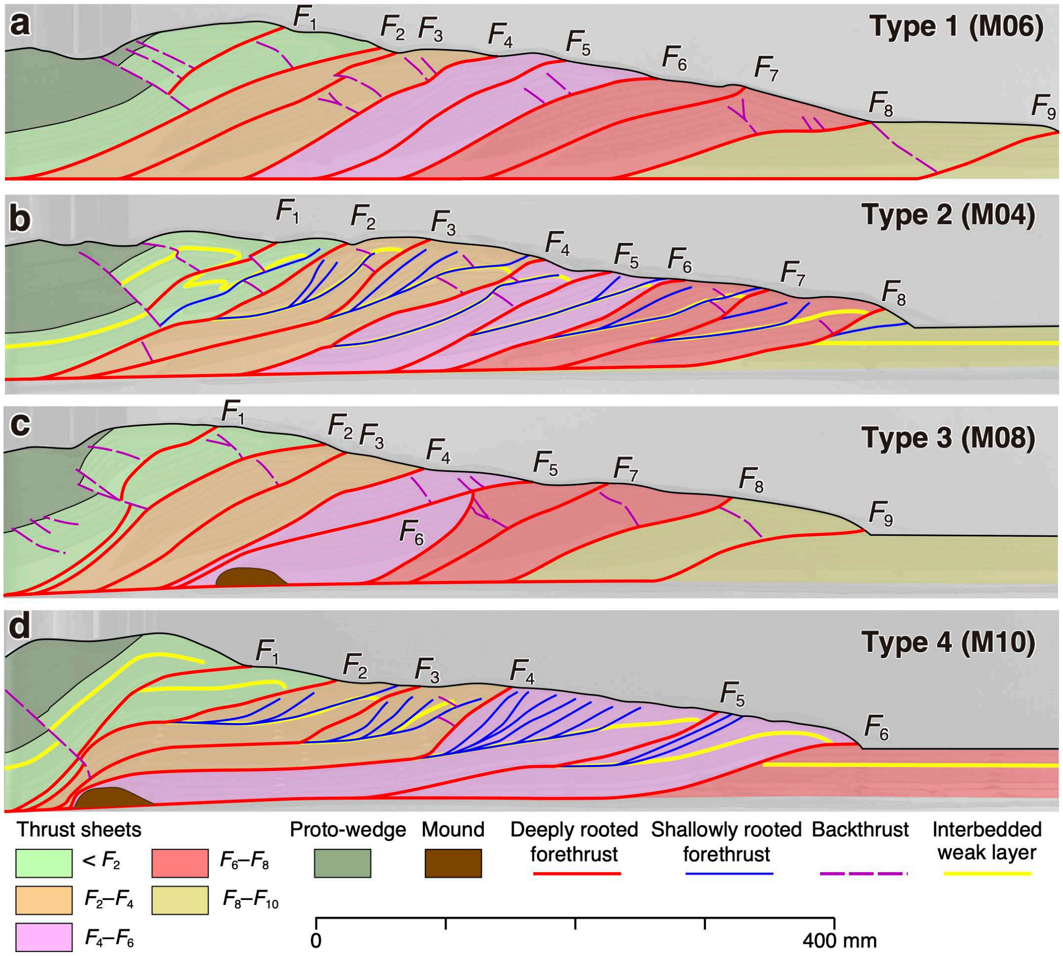
a
Type 1 (M06)
F1
F2
F3
F4
F5
F6
F7
F8
F9
b
Type 2 (M04)
F1
F2
F3
F4
F5
F6
F7
F8
c
Type 3 (M08)
F1
F2
F3
F4
F5
F6
F7
F8
F9
d
Type 4 (M10)
F1
F2
F3
F4
F5
F6
Thrust sheets
< F2
F2–F4
F4–F6
F6–F8
F8–F10
Proto-wedge
Mound
Deeply rooted forethrust
Shallowly rooted forethrust
Backthrust
Interbedded weak layer
0
400 mm

Figure 5.

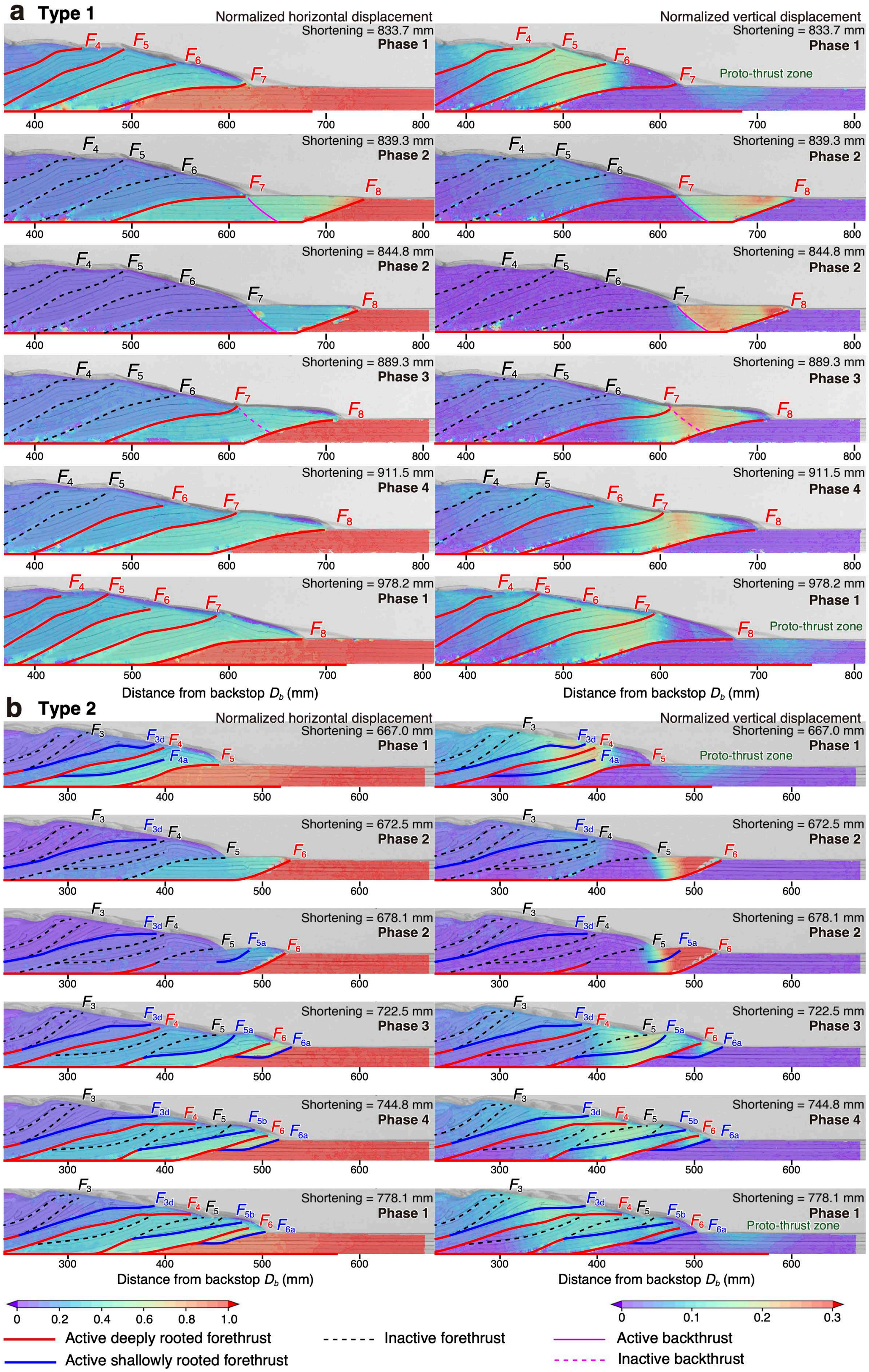

a Type 1
Normalized horizontal displacement
Normalized vertical displacement
Shortening = 833.7 mm
Phase 1
Proto-thrust zone
Shortening = 839.3 mm
Phase 2
Shortening = 844.8 mm
Phase 2
Shortening = 889.3 mm
Phase 3
Shortening = 911.5 mm
Phase 4
Shortening = 978.2 mm
Phase 1
Proto-thrust zone
F4
F5
F6
F7
F8
400
500
600
700
800
Distance from backstop D_b (mm)
b Type 2
Normalized horizontal displacement
Normalized vertical displacement
Shortening = 667.0 mm
Phase 1
Proto-thrust zone
Shortening = 672.5 mm
Phase 2
Shortening = 678.1 mm
Phase 2
Shortening = 722.5 mm
Phase 3
Shortening = 744.8 mm
Phase 4
Shortening = 778.1 mm
Phase 1
Proto-thrust zone
F3
F3d
F4
F4a
F5
F5a
F5b
F6
F6a
300
400
500
600
Distance from backstop D_b (mm)
0
0.2
0.4
0.6
0.8
1.0
0
0.1
0.2
0.3
Active deeply rooted forethrust
Active shallowly rooted forethrust
Inactive forethrust
Active backthrust
Inactive backthrust

Figure 6.

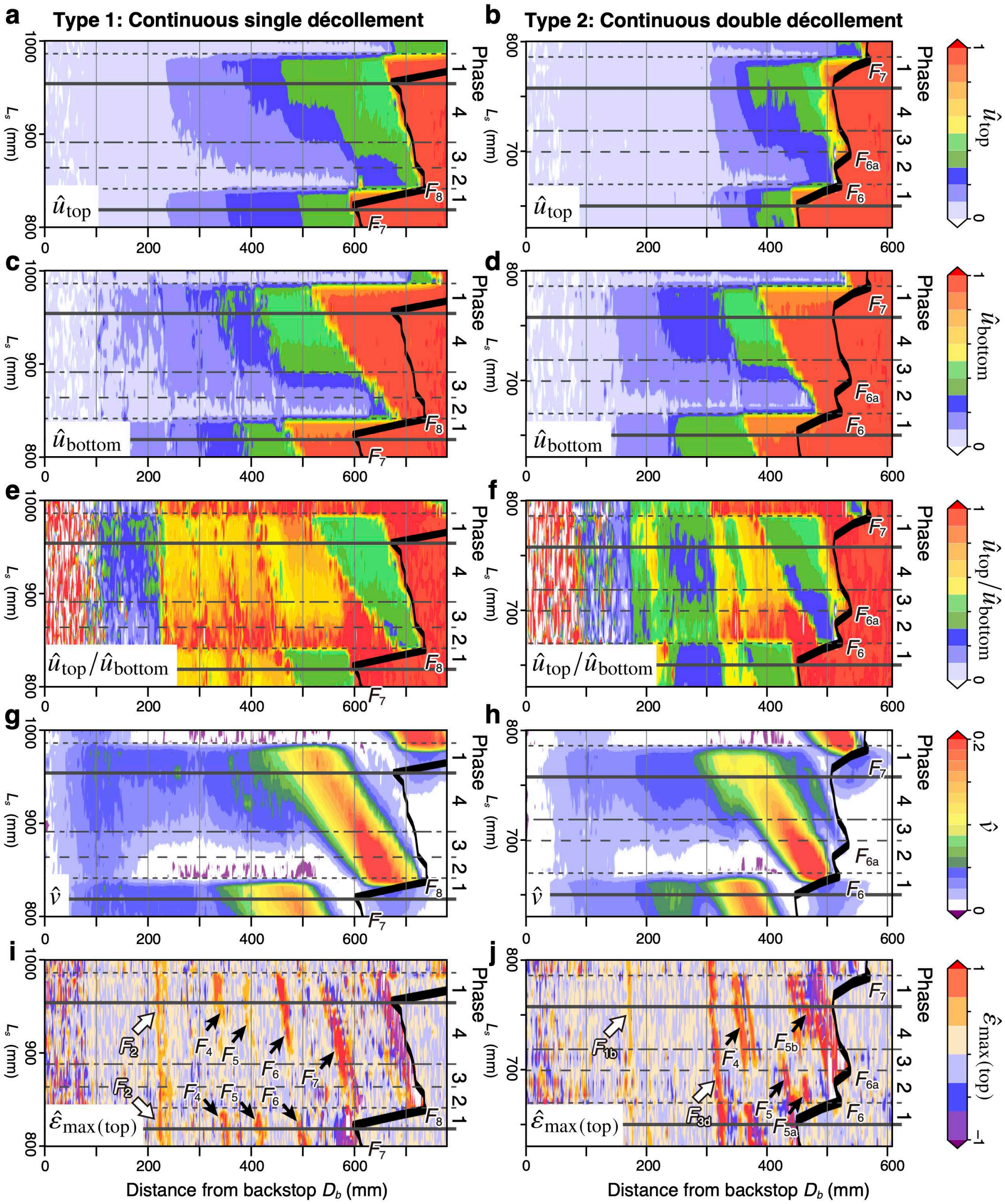
a
Type 1: Continuous single décollement
b
Type 2: Continuous double décollement
c
d
e
f
g
h
i
j
L_s (mm)
1000
900
800
700
Phase
1
4
3
2
1
$\hat{u}_{\text{top}}$
$\hat{u}_{\text{bottom}}$
$\hat{u}_{\text{top}}/\hat{u}_{\text{bottom}}$
$\hat{v}$
$\hat{\varepsilon}_{\max(\text{top})}$
0
0.2
−1
F_2
F_4
F_5
F_6
F_7
F_8
F_{1b}
F_{3d}
F_{5a}
F_{5b}
F_{6a}
0
200
400
600
Distance from backstop D_b (mm)

Figure 7.

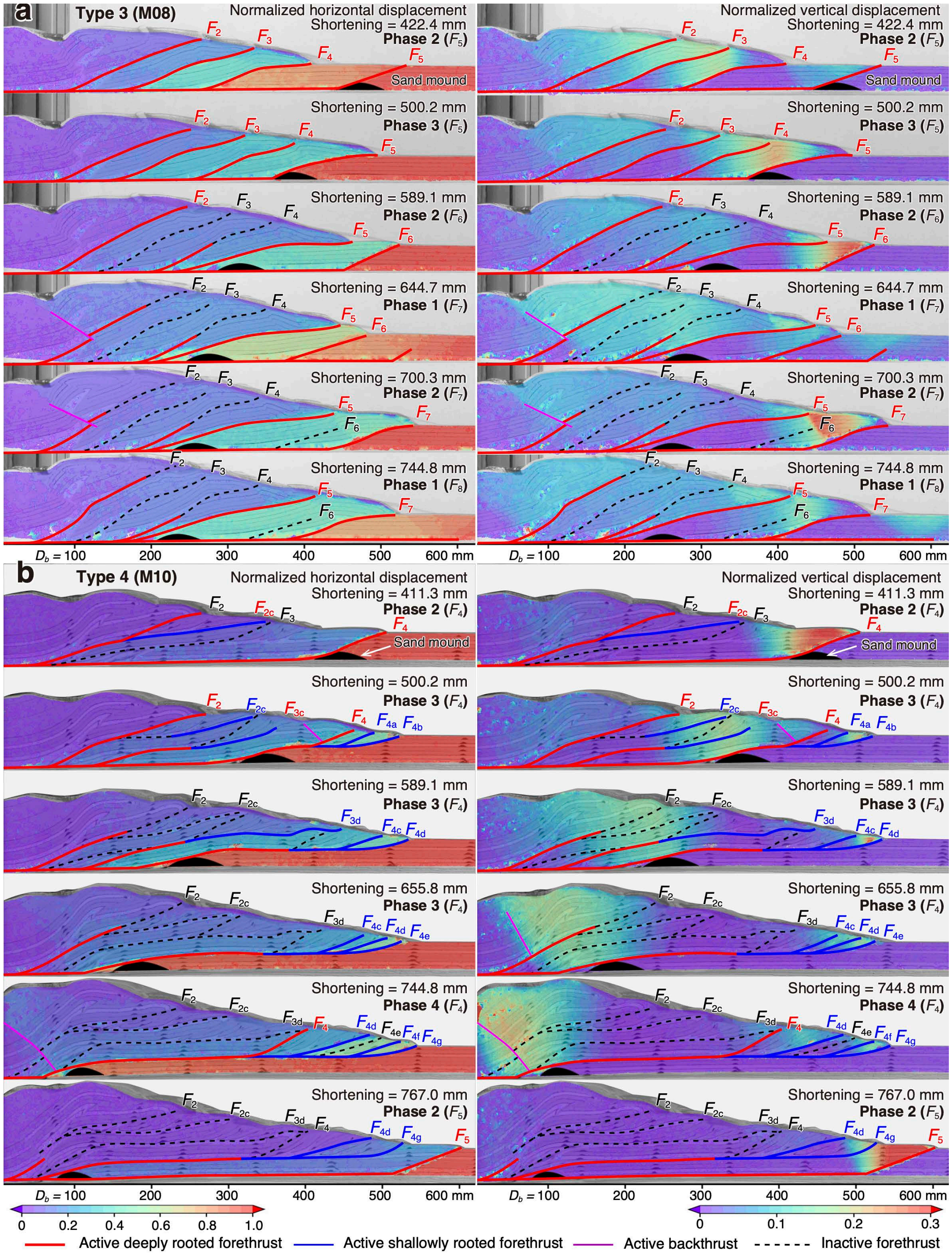
a
Type 3 (M08)
Normalized horizontal displacement
Normalized vertical displacement
Shortening = 422.4 mm
Phase 2 (F5)
Sand mound
Shortening = 500.2 mm
Phase 3 (F5)
Shortening = 589.1 mm
Phase 2 (F6)
Shortening = 644.7 mm
Phase 1 (F7)
Shortening = 700.3 mm
Phase 2 (F7)
Shortening = 744.8 mm
Phase 1 (F8)
F2
F3
F4
F5
F6
F7
Db = 100
200
300
400
500
600 mm
b
Type 4 (M10)
Normalized horizontal displacement
Normalized vertical displacement
Shortening = 411.3 mm
Phase 2 (F4)
Sand mound
Shortening = 500.2 mm
Phase 3 (F4)
Shortening = 589.1 mm
Phase 3 (F4)
Shortening = 655.8 mm
Phase 3 (F4)
Shortening = 744.8 mm
Phase 4 (F4)
Shortening = 767.0 mm
Phase 2 (F5)
F2
F2c
F3
F3c
F3d
F4
F4a
F4b
F4c
F4d
F4e
F4f
F4g
F5
Db = 100
200
300
400
500
600 mm
0
0.2
0.4
0.6
0.8
1.0
0
0.1
0.2
0.3
Active deeply rooted forethrust
Active shallowly rooted forethrust
Active backthrust
Inactive forethrust

Figure 8.

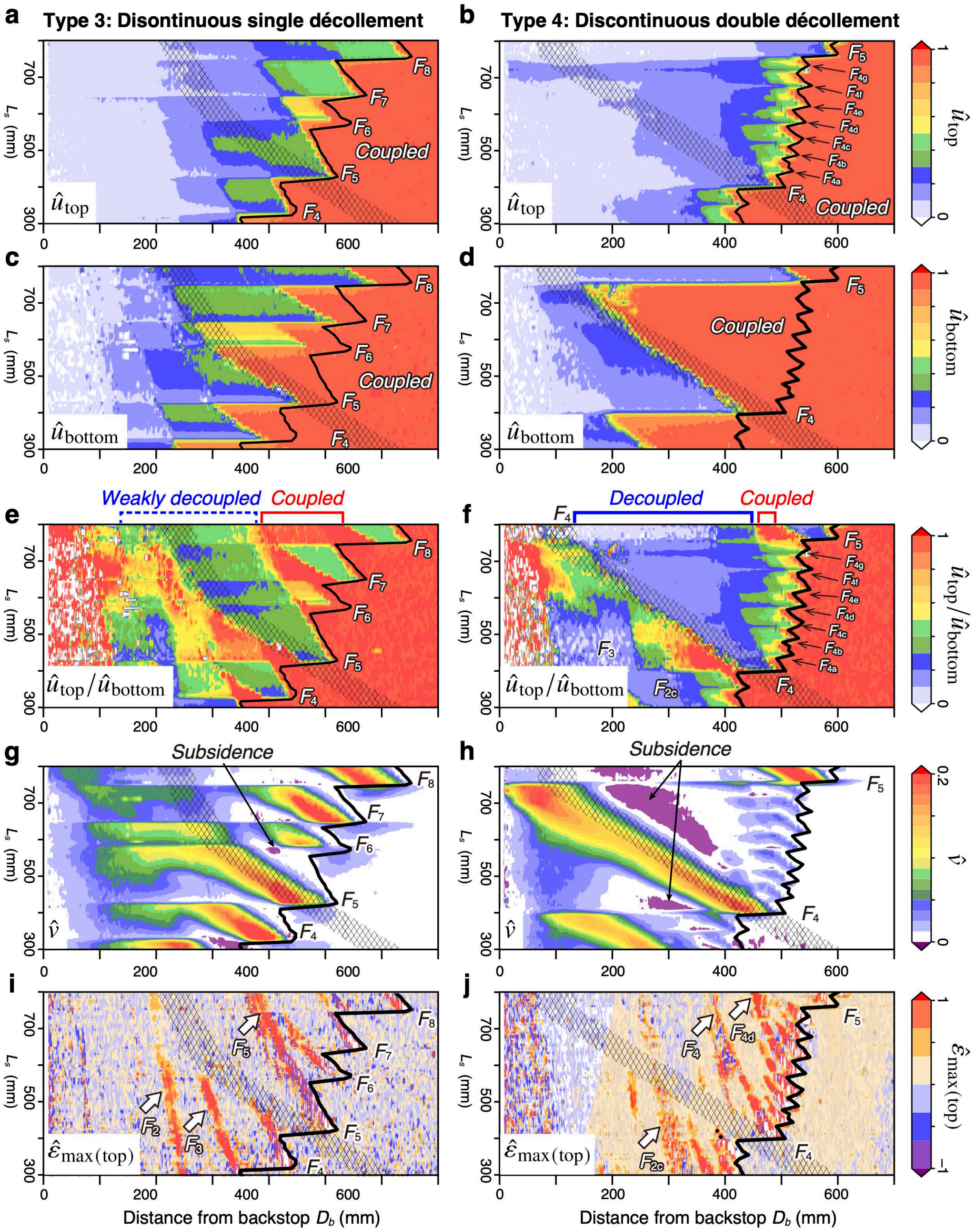
a
Type 3: Disontinuous single décollement
b
Type 4: Discontinuous double décollement
$\hat{u}_{\mathrm{top}}$
$\hat{u}_{\mathrm{bottom}}$
$\hat{u}_{\mathrm{top}}/\hat{u}_{\mathrm{bottom}}$
$\hat{v}$
$\hat{\varepsilon}_{\max(\mathrm{top})}$
Coupled
Weakly decoupled
Decoupled
Subsidence
F2
F2c
F3
F4
F4a
F4b
F4c
F4d
F4e
F4f
F4g
F5
F6
F7
F8
c
d
e
f
g
h
i
j
L_s (mm)
300
500
700
0
200
400
600
0.2
1
−1
Distance from backstop D_b (mm)

Figure 9.

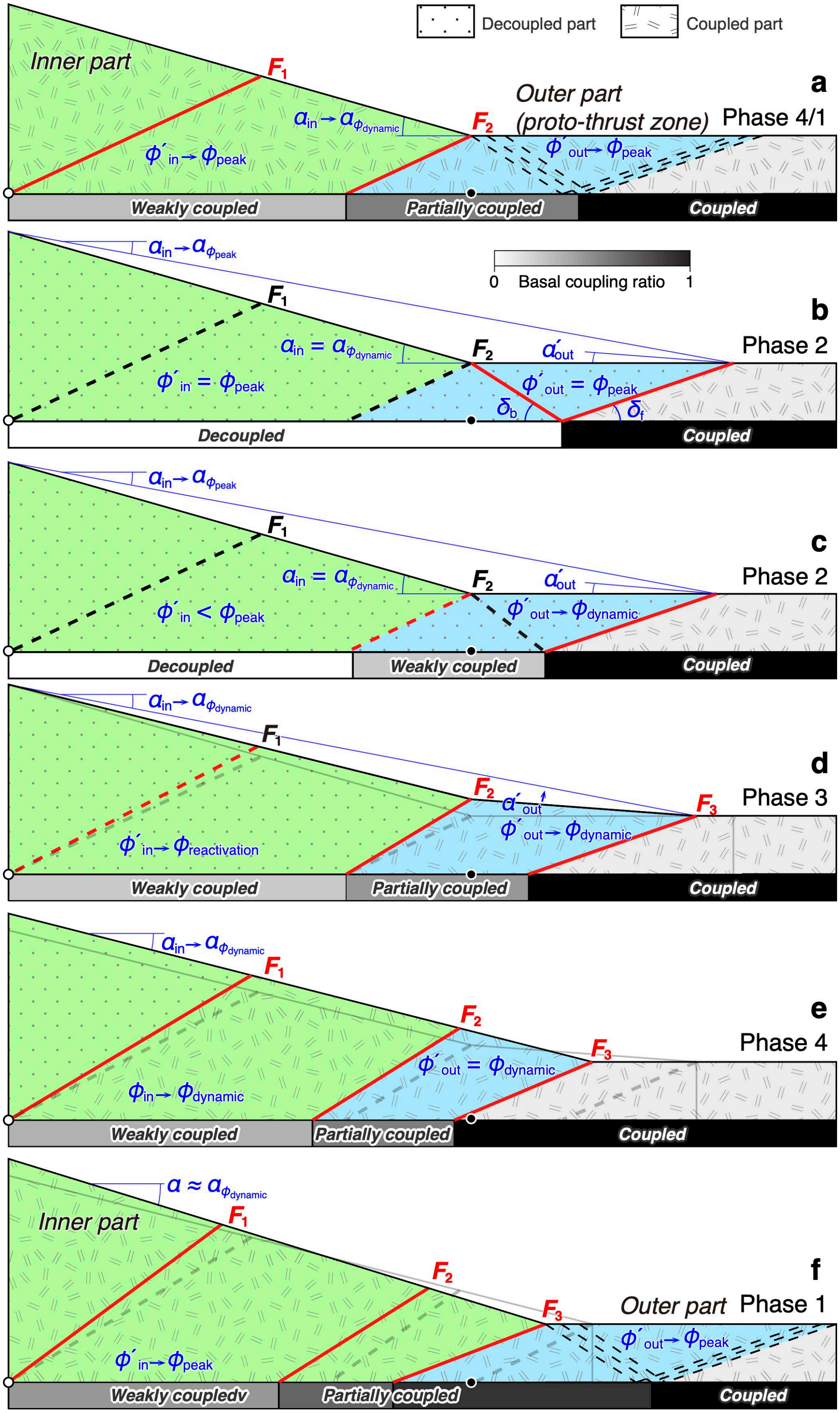
Decoupled part
Coupled part
a
Phase 4/1
Inner part
Outer part
(proto-thrust zone)
F1
F2
α_in → α_φdynamic
φ′_in → φ_peak
φ′_out → φ_peak
Weakly coupled
Partially coupled
Coupled
b
Phase 2
0 Basal coupling ratio 1
α_in → α_φpeak
F1
F2
α_in = α_φdynamic
α′_out
φ′_in = φ_peak
φ′_out = φ_peak
δ_b
δ_f
Decoupled
Coupled
c
Phase 2
α_in → α_φpeak
F1
F2
α_in = α_φdynamic
α′_out
φ′_in < φ_peak
φ′_out → φ_dynamic
Decoupled
Weakly coupled
Coupled
d
Phase 3
α_in → α_φdynamic
F1
F2
F3
α′_out
φ′_out → φ_dynamic
φ′_in → φ_reactivation
Weakly coupled
Partially coupled
Coupled
e
Phase 4
α_in → α_φdynamic
F1
F2
F3
φ′_out = φ_dynamic
φ_in → φ_dynamic
Weakly coupled
Partially coupled
Coupled
f
Phase 1
α ≈ α_φdynamic
Inner part
F1
F2
F3
Outer part
φ′_out → φ_peak
φ′_in → φ_peak
Weakly coupledv
Partially coupled
Coupled

Figure 10.

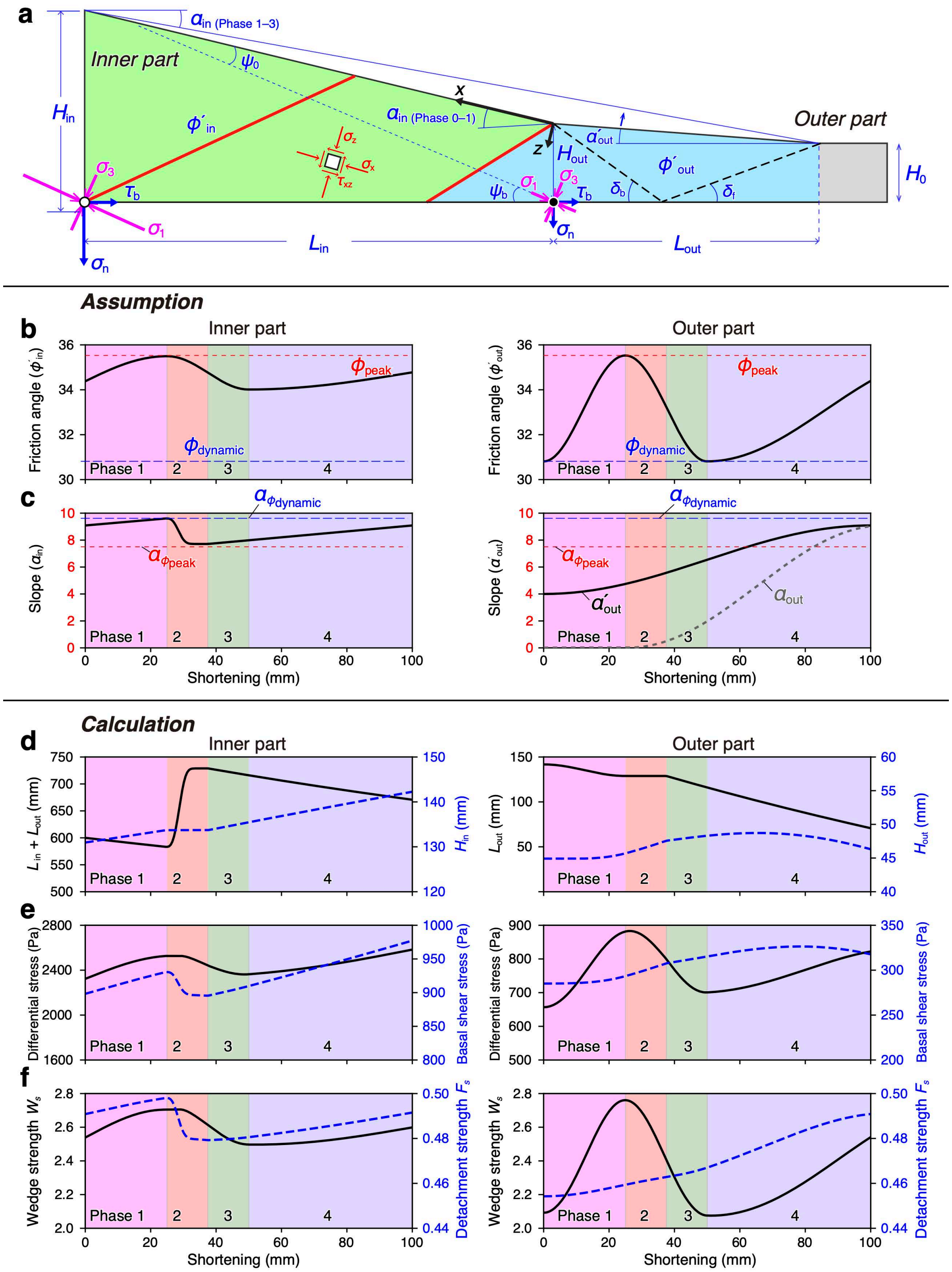
a
α_in (Phase 1–3)
Inner part
ψ_0
H_in
φ´_in
x
α_in (Phase 0–1)
σ_z
σ_x
τ_xz
z
H_out
α´_out
φ´_out
Outer part
H_0
σ_3
τ_b
σ_1
ψ_b
δ_b
δ_f
σ_n
L_in
L_out
Assumption
b
Inner part
Outer part
Friction angle (φ´_in)
Friction angle (φ´_out)
φ_peak
φ_dynamic
Phase 1
2
3
4
c
Slope (α_in)
Slope (α_out)
α_φdynamic
α_φpeak
α´_out
α_out
Shortening (mm)
Calculation
d
L_in + L_out (mm)
H_in (mm)
L_out (mm)
H_out (mm)
e
Differential stress (Pa)
Basal shear stress (Pa)
f
Wedge strength W_s
Detachment strength F_s
0
20
40
60
80
100

Figure 11.

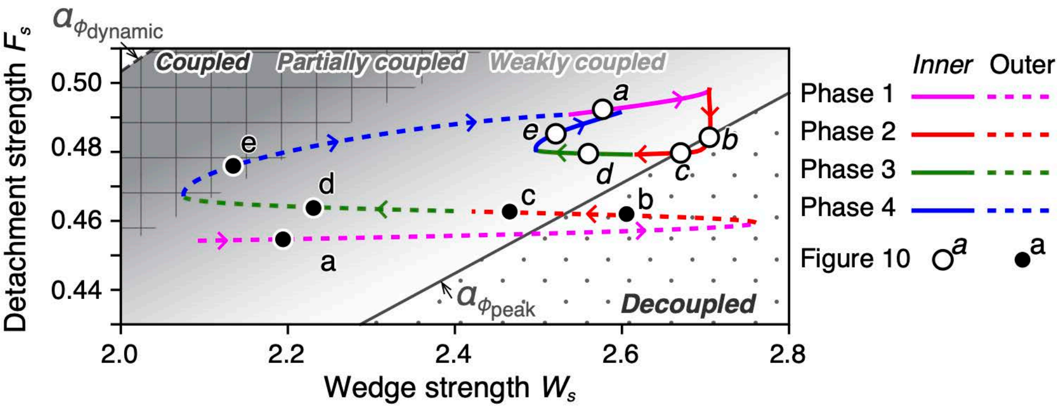

$\alpha_{\phi_{\text{dynamic}}}$
Coupled
Partially coupled
Weakly coupled
Decoupled
$\alpha_{\phi_{\text{peak}}}$
Detachment strength F_s
0.50
0.48
0.46
0.44
Wedge strength W_s
2.0
2.2
2.4
2.6
2.8
a
b
c
d
e
Inner
Outer
Phase 1
Phase 2
Phase 3
Phase 4
Figure 10

Figure 12.

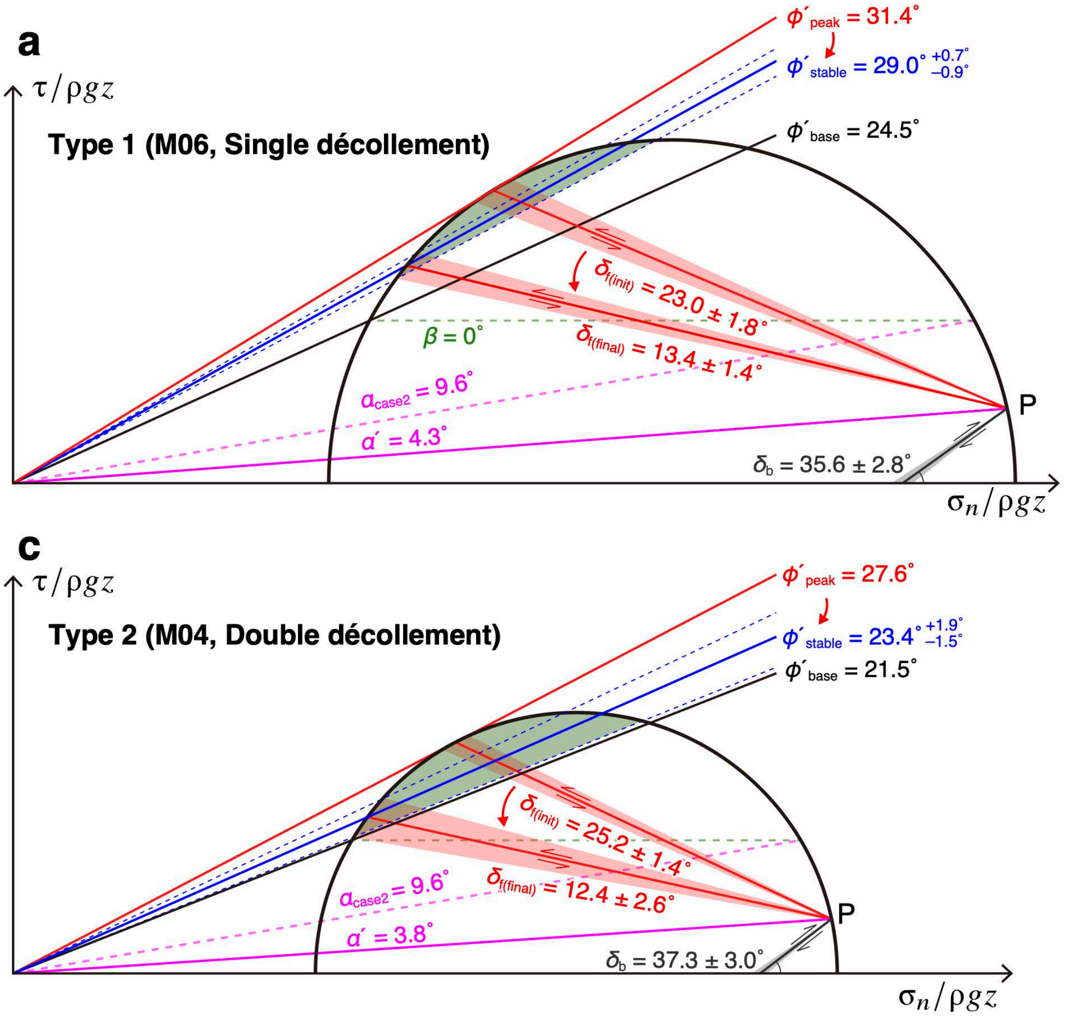
a
τ/ρgz
Type 1 (M06, Single décollement)
φ´peak = 31.4°
φ´stable = 29.0° +0.7° −0.9°
φ´base = 24.5°
δf(init) = 23.0 ± 1.8°
δf(final) = 13.4 ± 1.4°
β = 0°
αcase2 = 9.6°
α´ = 4.3°
P
δb = 35.6 ± 2.8°
σn/ρgz
c
τ/ρgz
Type 2 (M04, Double décollement)
φ´peak = 27.6°
φ´stable = 23.4° +1.9° −1.5°
φ´base = 21.5°
δf(init) = 25.2 ± 1.4°
δf(final) = 12.4 ± 2.6°
αcase2 = 9.6°
α´ = 3.8°
P
δb = 37.3 ± 3.0°
σn/ρgz

Figure 13.

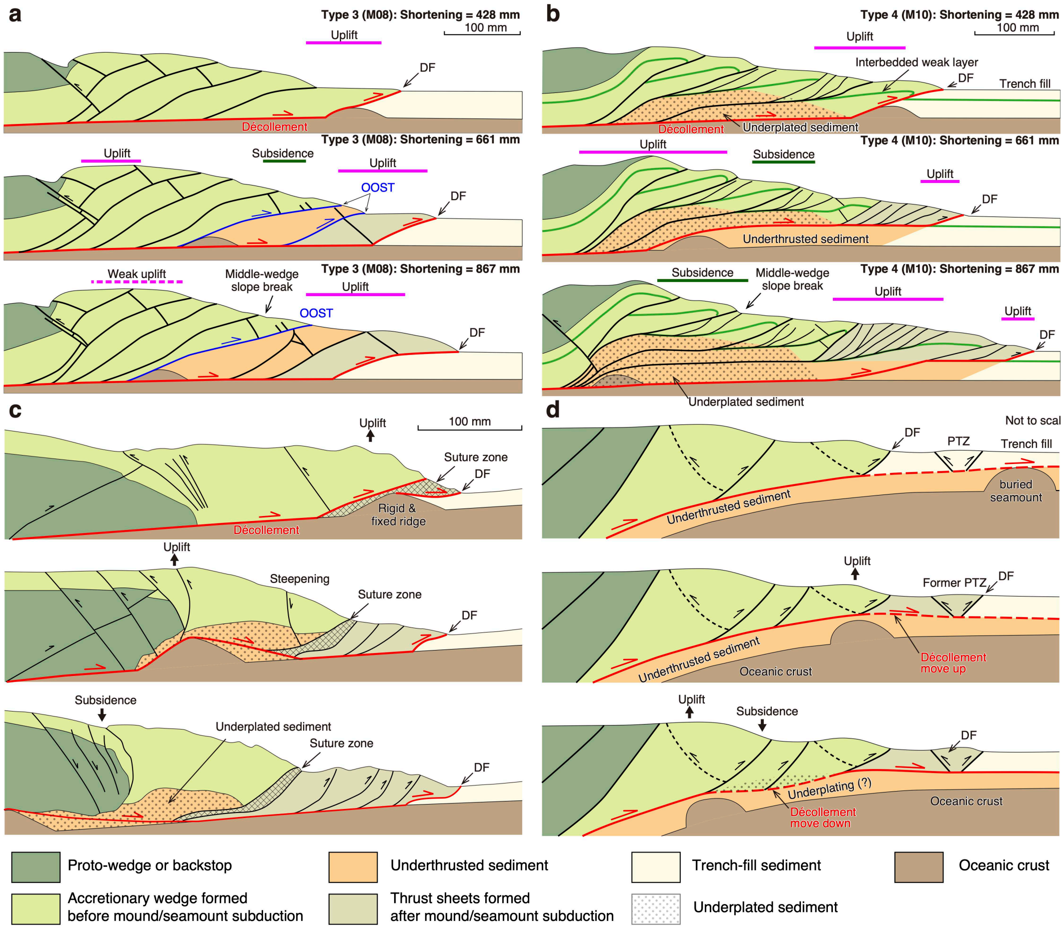
a
Type 3 (M08): Shortening = 428 mm
100 mm
Uplift
DF
Décollement
Type 3 (M08): Shortening = 661 mm
Uplift
Subsidence
Uplift
OOST
DF
Type 3 (M08): Shortening = 867 mm
Weak uplift
Middle-wedge slope break
Uplift
OOST
DF
b
Type 4 (M10): Shortening = 428 mm
100 mm
Uplift
Interbedded weak layer
DF
Trench fill
Décollement
Underplated sediment
Uplift
Subsidence
Type 4 (M10): Shortening = 661 mm
Uplift
DF
Underthrusted sediment
Subsidence
Middle-wedge slope break
Type 4 (M10): Shortening = 867 mm
Uplift
Uplift
DF
Underplated sediment
c
Uplift
100 mm
Suture zone
DF
Rigid & fixed ridge
Décollement
Uplift
Steepening
Suture zone
DF
Subsidence
Underplated sediment
Suture zone
DF
d
Not to scal
DF
PTZ
Trench fill
buried seamount
Underthrusted sediment
Uplift
Former PTZ
DF
Underthrusted sediment
Oceanic crust
Décollement move up
Uplift
Subsidence
DF
Underplating (?)
Décollement move down
Oceanic crust
Proto-wedge or backstop
Accretionary wedge formed before mound/seamount subduction
Underthrusted sediment
Thrust sheets formed after mound/seamount subduction
Trench-fill sediment
Underplated sediment
Oceanic crust

Figure 14.

Supporting Information for "Accretion cycles, structural evolution, and thrust activity in accretionary wedges with various décollement settings: Insights from sandbox analog modeling"

Atsushi Noda*,†[1], Fabien Graveleau†, César Witt†, Frank Chanier†, and Bruno Vendeville†[2]

*Geological Survey of Japan, National Institute of Advanced Industrial Science and Technology (AIST), Central 7, Higashi 1-1-1, Tsukuba, Ibaraki 305-8567, Japan

†University of Lille, CNRS, ULCO, IRD, UMR 8187, Laboratory of Oceanology and Geosciences (LOG), Lille, 59000, France

This is the supporting information for "Accretion cycle, structural evolution, and thrust activities in accretionary wedges with various décollement settings: Insights from sandbox analog modeling." A definitive version is published in doi: .

Noda, A., Graveleau, F., Witt, C., Chanier, F., and Vendeville, B., 2023, Accretion cycle, structural evolution, and thrust activities in accretionary wedges with various décollement settings: Insights from sandbox analog modeling. doi.

Keywords: subduction zone; analog modeling; accretionary wedge; digital image correlation

---

[1] Corresponding author: A. NODA (a.noda@aist.go.jp)

[2] Deceased

S1 Theoretical width, height, and slope of the wedge

The accretionary wedge develops and deforms at its Coulomb failure limit (Dahlen, 1984, 1990; Davis et al., 1983; Lehner, 1986). The topographic slope (α) can be predicted from the material properties of dry sand (i.e., no pore fluid pressure) relative to the basal slope angle of the décollement ($\beta = 0$ in this study), along with the basal (ϕ_b) and internal (ϕ) friction angles of the materials.

$$\begin{aligned}
\alpha &= \psi_{\mathrm{b}} - \psi_0 - \beta \\
\psi_0 &= \frac{1}{2}\arcsin\left(\frac{\sin\alpha}{\sin\phi}\right) - \frac{1}{2}\alpha \\
\psi_{\mathrm{b}} &= \frac{1}{2}\arcsin\left(\frac{\sin\phi_b}{\sin\phi}\right) - \frac{1}{2}\phi_b.
\end{aligned}$$

When the basal décollement consists of glass microbeads with a dynamic friction angle $\phi_b = 24.0°$, the theoretical wedge slopes are $\alpha_{\phi_{\mathrm{peak}}} = 7.5°$ for sand with a peak friction angle $\phi_{\mathrm{peak}} = 30.8°$ (case 1 in Figure S1) and $\alpha_{\phi_{\mathrm{dynamic}}} = 9.6°$ for the overlying sand layer with a dynamic friction angle $\phi_{\mathrm{dynamic}} = 30.8°$ (case 2 in Figure S1).

We can estimate the theoretical wedge width (W_w) and height (H_w) by using these slope angles (Figure S2). A simplified wedge area can then be expressed as:

$$\begin{aligned}
& \frac{1}{2}H_w(W_w + Wp) \\
&= \frac{1}{2}W_w^2\tan\alpha + \frac{1}{2}W_w^2\tan^2\alpha\tan\eta \\
&= H_s \times W_s,
\end{aligned}$$

where W_s is the cumulative shortening length, γ is the slope angle of the proto-wedge (~31°), and H_s is the thickness of the incoming sediment layer. The theoretical height should be simply $W_w \tan\alpha$.

S2 Thrust propagation and effective internal friction

We measured the shortening length required for the propagation of a new frontal thrust, and the length of a new ramp (Figures 3e, S12a, and S13a–b) and dip angles of the deeply rooted frontal forethrusts ($\delta_{\mathrm{f(init)}}$) and conjugate backthrusts (δ_{b}) when the new frontal thrust emerges (Figures 3e, S12b, and S13c–e).

The shortening length required for propagation of a new deeply rooted forethrust is generally 116–136 mm in the type 1–3 models, but much larger in the type 4 model (144–211 mm) (Figures S12a and S13a). The lengths of the new ramps are 103–113 mm for the type 1 and 3 models, and 72–91 mm for the type 2 and 4 models. These shortening lengths for new thrust propagation are ∼1.1–1.3 times larger than the length of a new ramp in the type 1 and 3 models, 1.5 times than that in the type 2 model, and 2.0 times than that in the type 4 model (Figure S12a).

The initial dip angles of the frontal deeply rooted forethrusts ($\delta_{\mathrm{f(init)}}$) in the type 1 and 3 models is averaged around ∼23° and those of the type 2 and 4 models are ∼25° (Figures S12b and S13d). The backthrust angles (δ_{b}) vary between 36–40° and do not exhibit a clear difference between model types (Figures S12b and S13c).

The annotated lines in Figure S12b were drawn to estimate the effective internal friction (ϕ') and effective surface slope angles (α') for a given $\delta_{\mathrm{f(init)}}$ and δ_{b} when a new forethrust is initiated. These lines are based on the non-cohesive critical taper theory (Dahlen, 1984).

$$\delta_{\mathrm{f}} = \frac{\pi}{4} - \frac{\phi'}{2} - \psi_{\mathrm{b}} \tag{S1}$$

$$\delta_{\mathrm{b}} = \frac{\pi}{4} - \frac{\phi'}{2} + \psi_{\mathrm{b}} \tag{S2}$$

with

$$\psi_0 = \frac{1}{2}\sin^{-1}\left(\frac{\sin\alpha'}{\sin\phi'}\right) - \frac{1}{2}\alpha' \tag{S3}$$

$$\psi_{\mathrm{b}} = \alpha' + \beta - \psi_0 \tag{S4}$$

where β is 0.

For example, the data for the type 1 model (red circle in Figure S12b) indicates ϕ' is 31.4° and α' is 4.3°. For the type 2 model, ϕ' is 27.6° and α' is 3.8°.

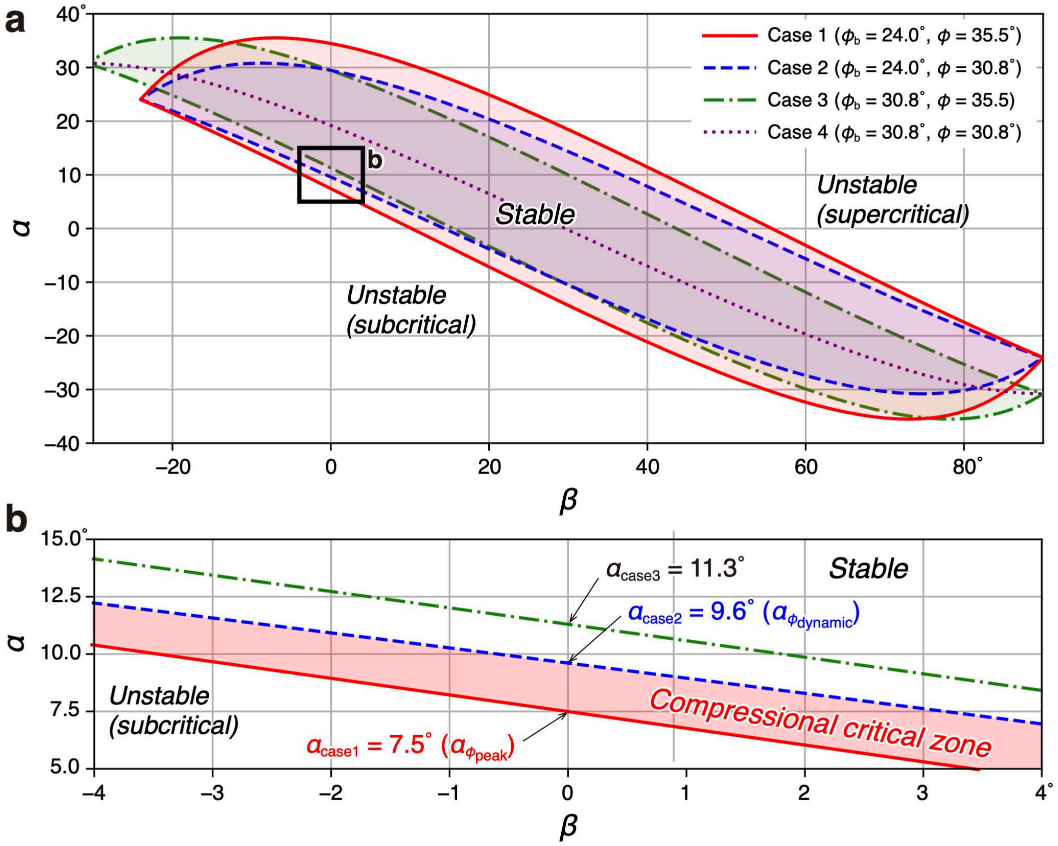

Figure S1. (a) Plots of the stability fields for critical taper wedges, with the surface slope (α) and basal dip (β). Four cases are plotted with different basal and internal friction angles. ϕ_b = basal friction angle; ϕ = internal friction angle. Case 1: $\phi_b = 24.0^\circ$ (dynamic friction angle of the glass microbeads) and $\phi = 35.5^\circ$ (peak friction angle of the sand). Case 2: $\phi_b = 24.0^\circ$ (dynamic friction angle of the microbeads) and $\phi = 30.8^\circ$ (dynamic friction angle of the sand). Case 3: $\phi_b = 30.8^\circ$ (dynamic friction angle of the sand) and $\phi = 35.5^\circ$ (peak friction of the sand). Case 4: $\phi_b = \phi = 30.8^\circ$ (dynamic friction angle of the sand). Details of the frictional properties are listed in Table 1. (b) Enlarged view of (a) around $\beta = 0$. The shaded area bounded by case 1 ($\alpha_{\phi_{\mathrm{peak}}} = 7.5^\circ$) and case 2 ($\alpha_{\phi_{\mathrm{dynamic}}} = 9.6^\circ$) is the compressional critical zone for this study.

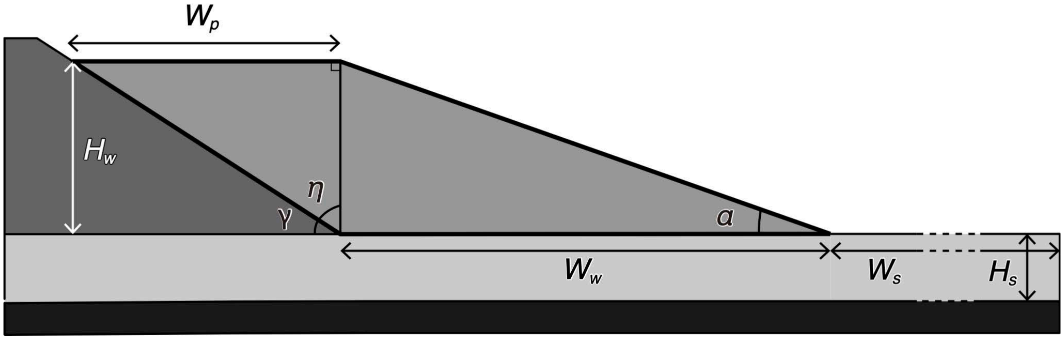

Figure S2. Sketch for the calculation of the theoretical width and height of the wedge.

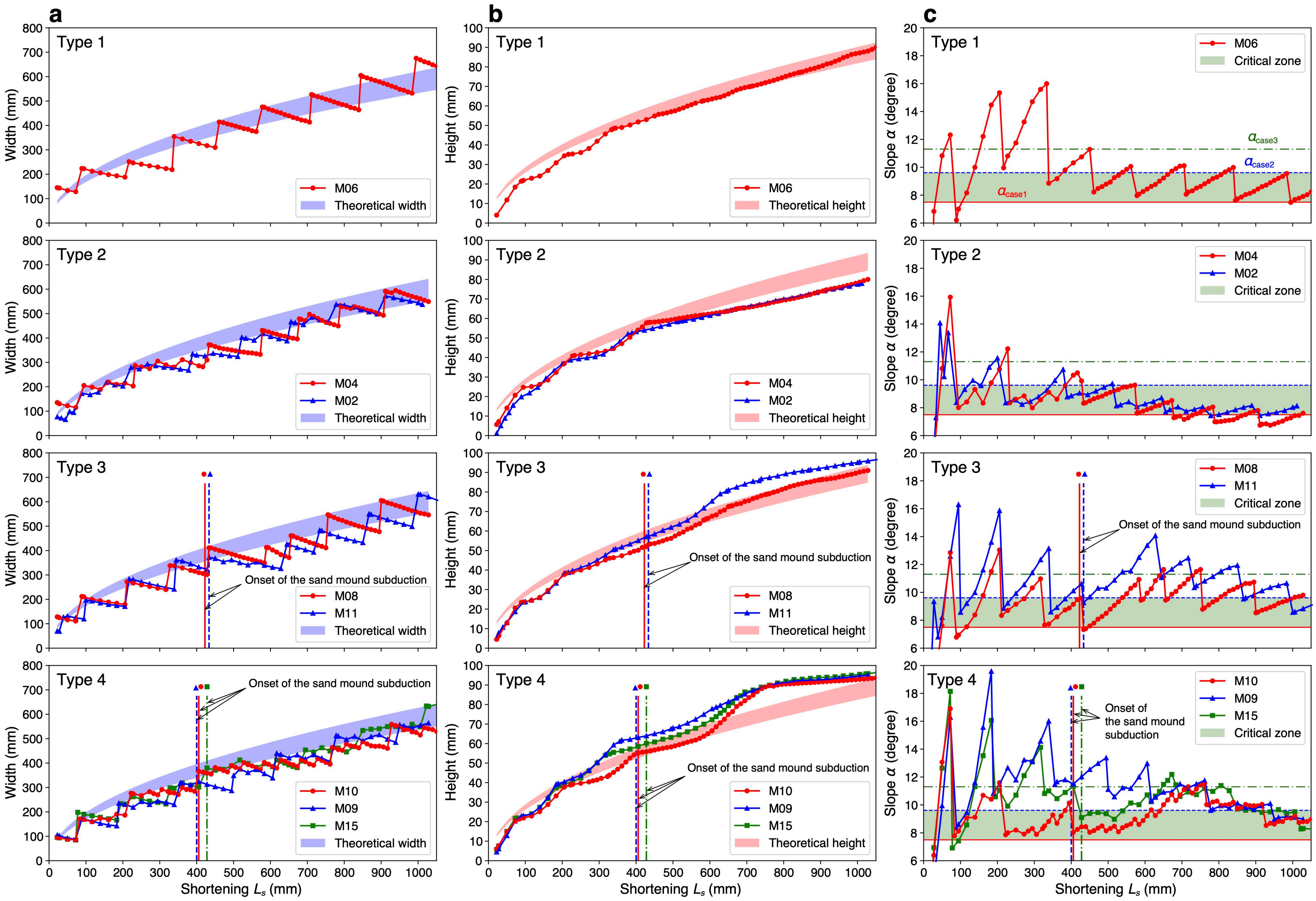

Figure S3. Plots of the geometrical parameters for all models. (a) Width. (b) Height. (c) Slope. Vertical lines in the right column indicate shortening lengths of onset of the sand mound subduction. Horizontal lines of α_{case1}, α_{case2}, and α_{case3} in (c) show the critical slope angles for the cases 1–3 (Figure S1). Regions of the theoretical width and height and the critical zone of the slope are explained in Supporting Information S1 (Figure S2).

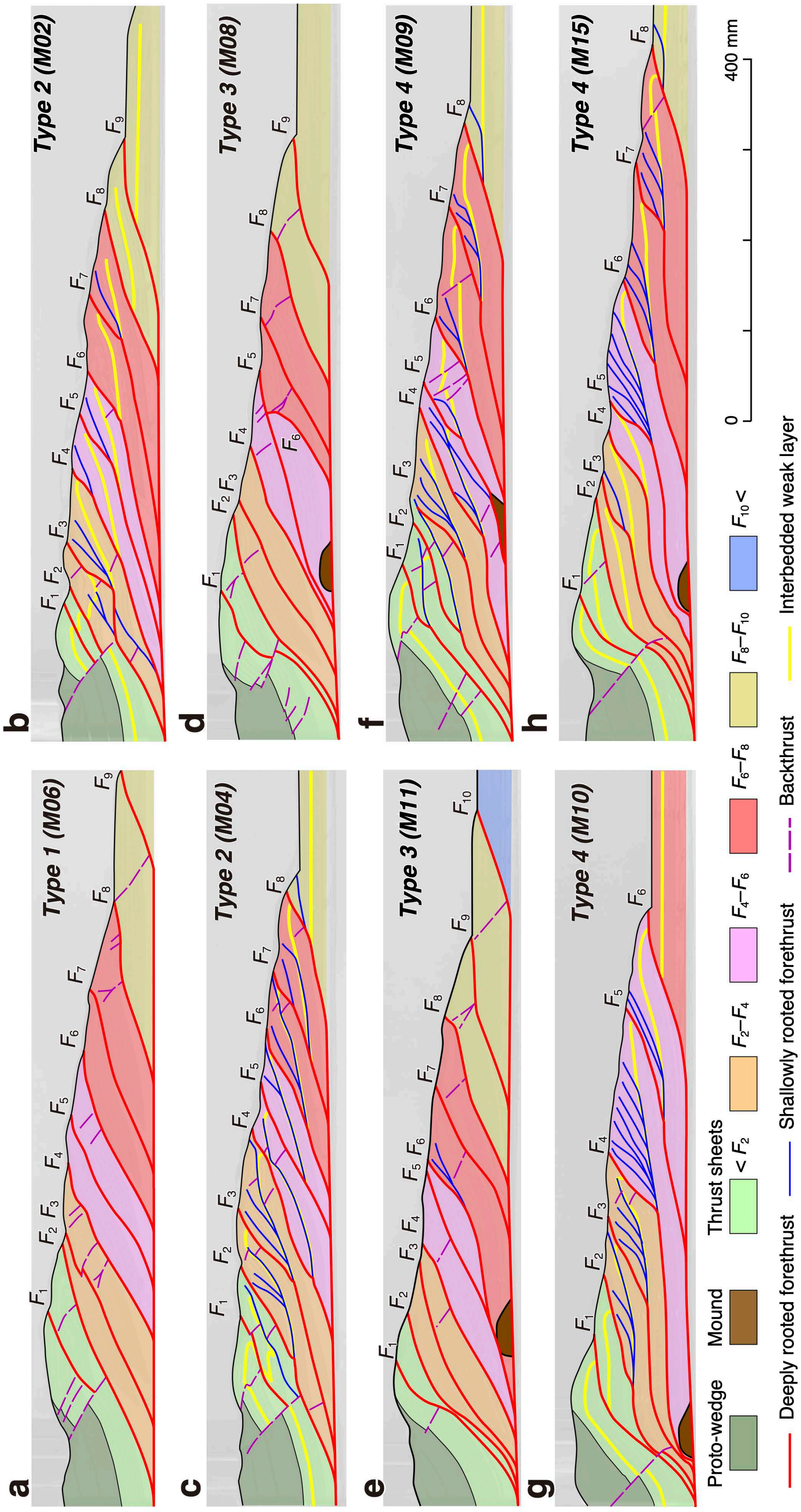

Figure S4. Final stacking patterns of all models. Numbered faults are deeply rooted forethrusts.

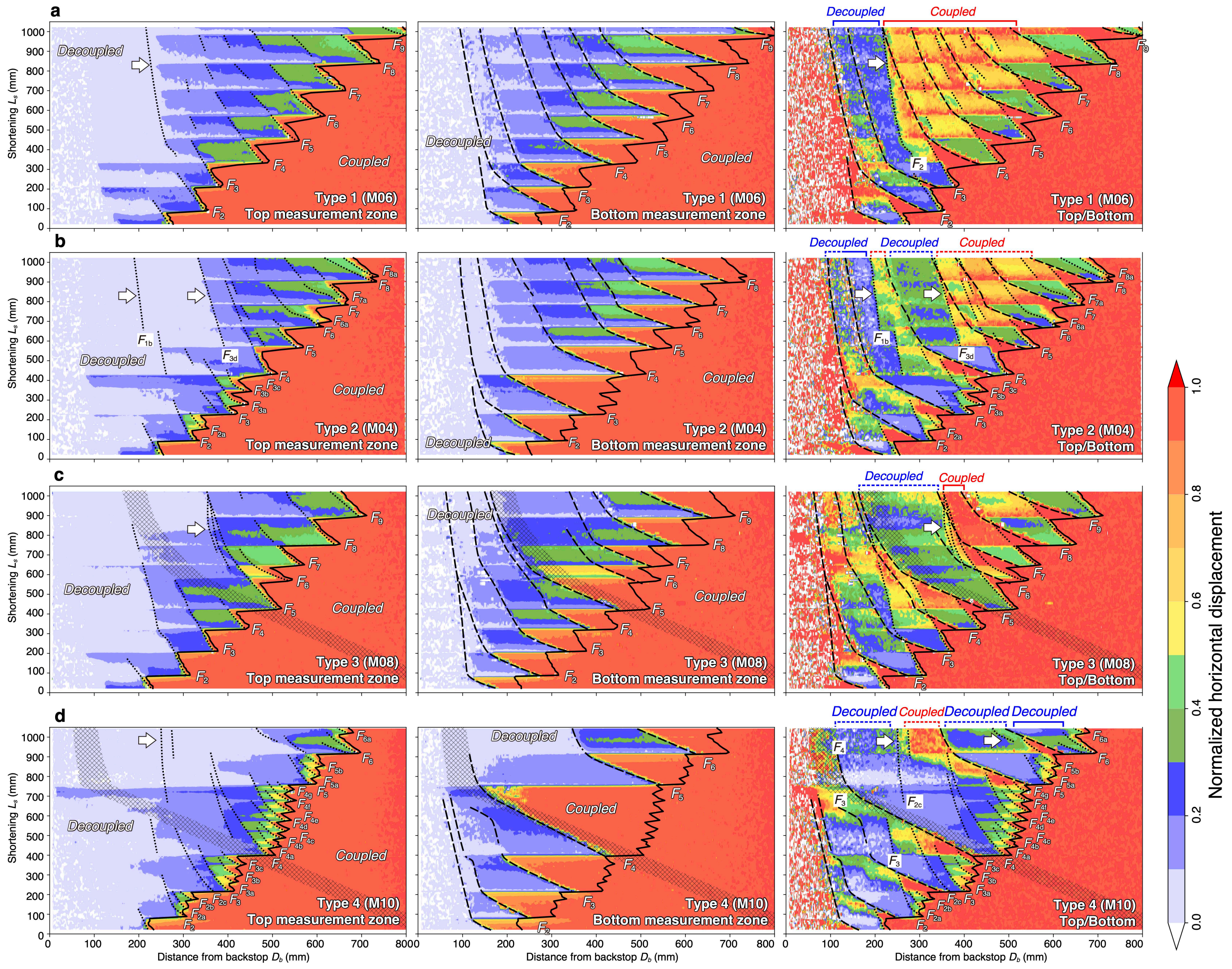

Figure S5. Normalized horizontal displacements in the top measurement zone ($\hat{u}_{\text{top}}$; left column) and bottom measurement zone ($\hat{u}_{\text{bottom}}$; middle column), and their ratio ($\hat{u}_{\text{top}}/\hat{u}_{\text{bottom}}$; right column) (see Figure 3 for the measured locations). (a) Type 1 model (M06). (b) Type 2 model (M04). (c) Type 3 model (M08). (d) Type 4 model (M10). Thick solid lines indicate the deformation front. Dotted lines (left column) and dashed lines (middle column) show the positions of active thrusts in the top and bottom measurement zones, respectively. White arrows are major out-of-sequence thrusts. In the right column, ratios $\hat{u}_{\text{top}}/\hat{u}_{\text{bottom}}$ indicate the degree of intra-wedge coupling between the upper and lower parts of the wedge. Meshed areas in (c) and (d) show the traces of the subducting sand mound.

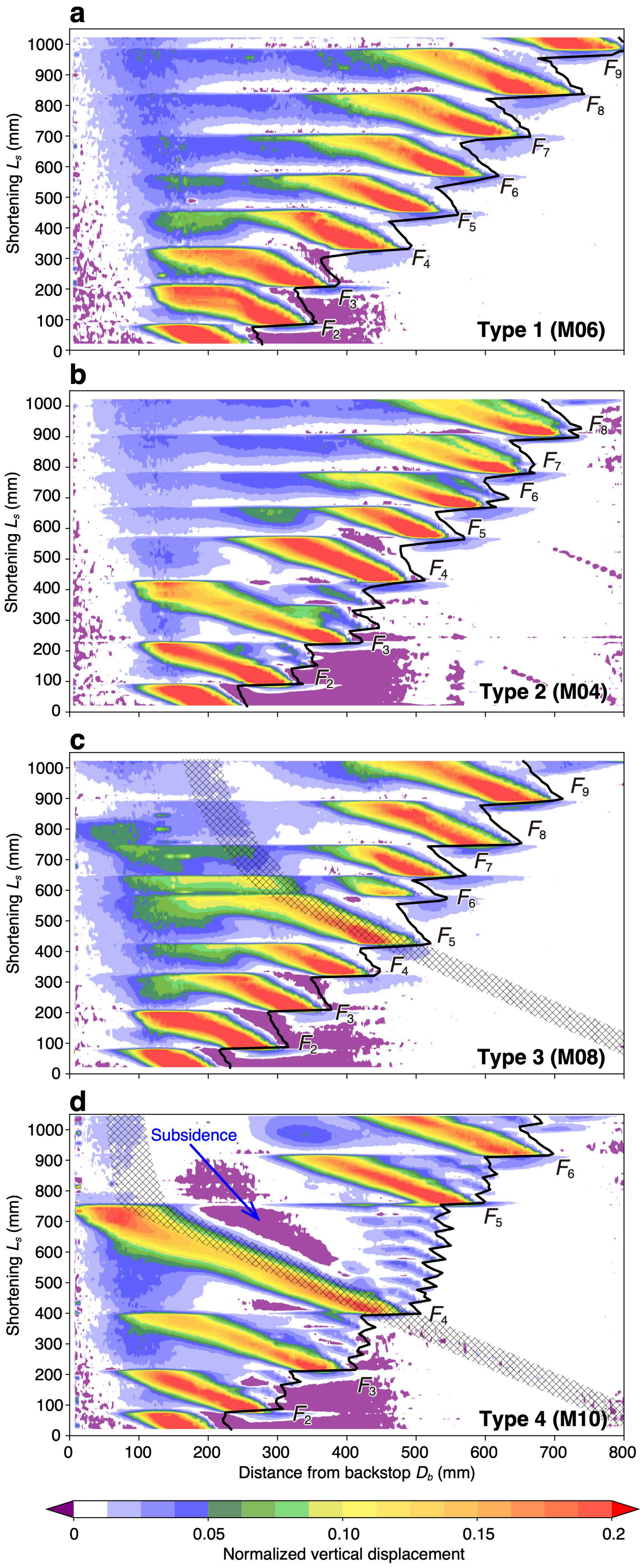

Figure S6. Normalized vertical displacement ($\hat{v}$) for the type 1–4 models. (a) Type 1 model (M06). (b) Type 2 model (M04). (c) Type 3 model (M08). (d) Type 4 model (M10). Thick solid lines are the deformation fronts. Meshed areas in (c) and (d) show the traces of the subducting

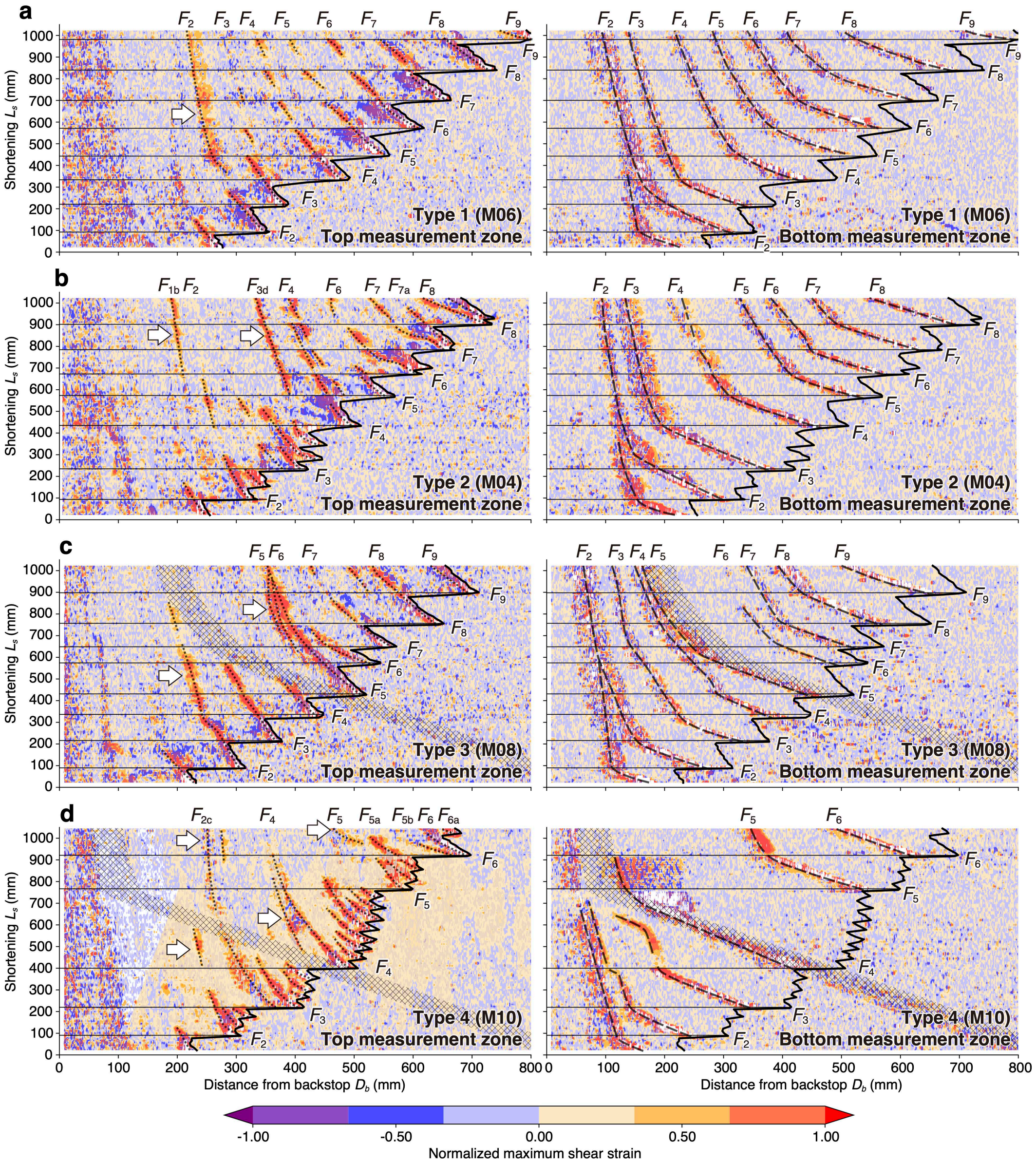

Figure S7. Normalized maximum shear strain in the top measurement zone ($\hat{\varepsilon}_{\max(\mathrm{top})}$; left column) and bottom measurement zone ($\hat{\varepsilon}_{\max(\mathrm{bottom})}$; right column) for the type 1–4 models. (a) Type 1 model (M06). (b) Type 2 model (M04). (c) Type 3 model (M08). (d) Type 4 model (M10). Positive and negative values indicate the direction of the shear strain (i.e., forethrusts [outward-vergent faults] are positive and backthrusts [inward-vergent faults] are negative). Thick solid lines show the deformation fronts. Thin horizontal lines indicate the timing of formation of a new deeply rooted frontal forethrust. White arrows are major out-of-sequence thrusts. Meshed areas in (c) and (d) show the traces of the subducting sand mound.

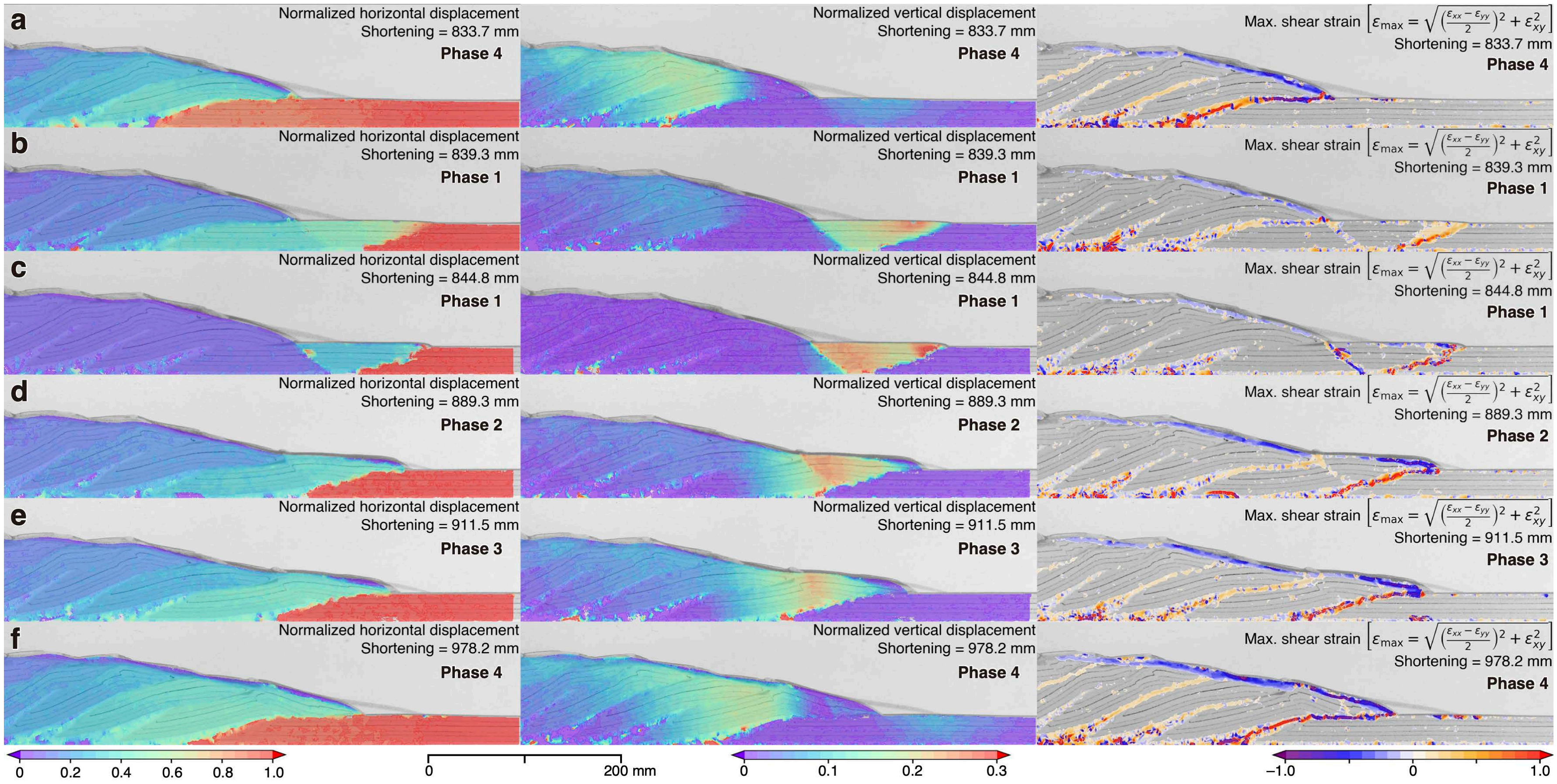

Figure S8. DIC images of the normalized horizontal ($\hat{u}$, left column), vertical displacement ($\hat{v}$, middle column), and maximum shear strain ($\hat{\varepsilon}_{\max}$) showing an accretion cycle in the Type 1 model (M06). Interpretations are shown in Figure 6a.

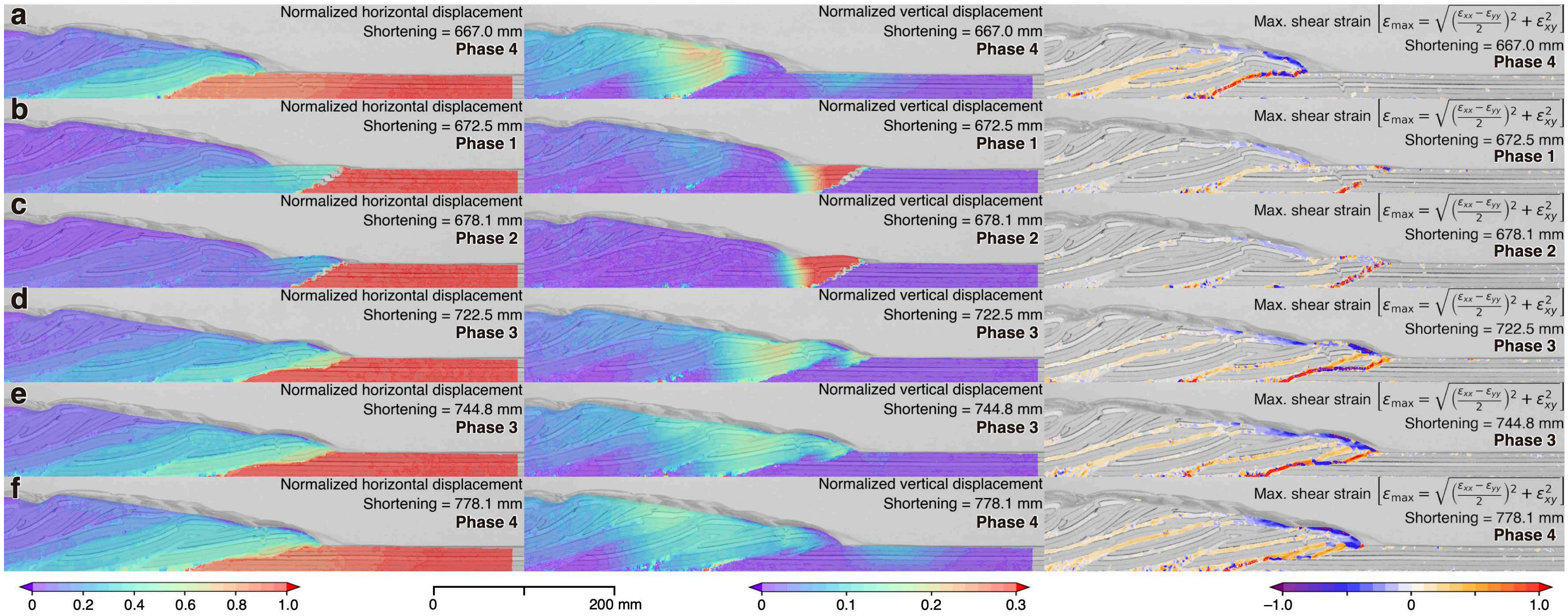

Figure S9. DIC images of the normalized horizontal ($\hat{u}$, left column) and vertical displacement ($\hat{v}$, right column) showing an accretion cycle in the Type 2 model (M04). Interpretations are shown in Figure 6b.

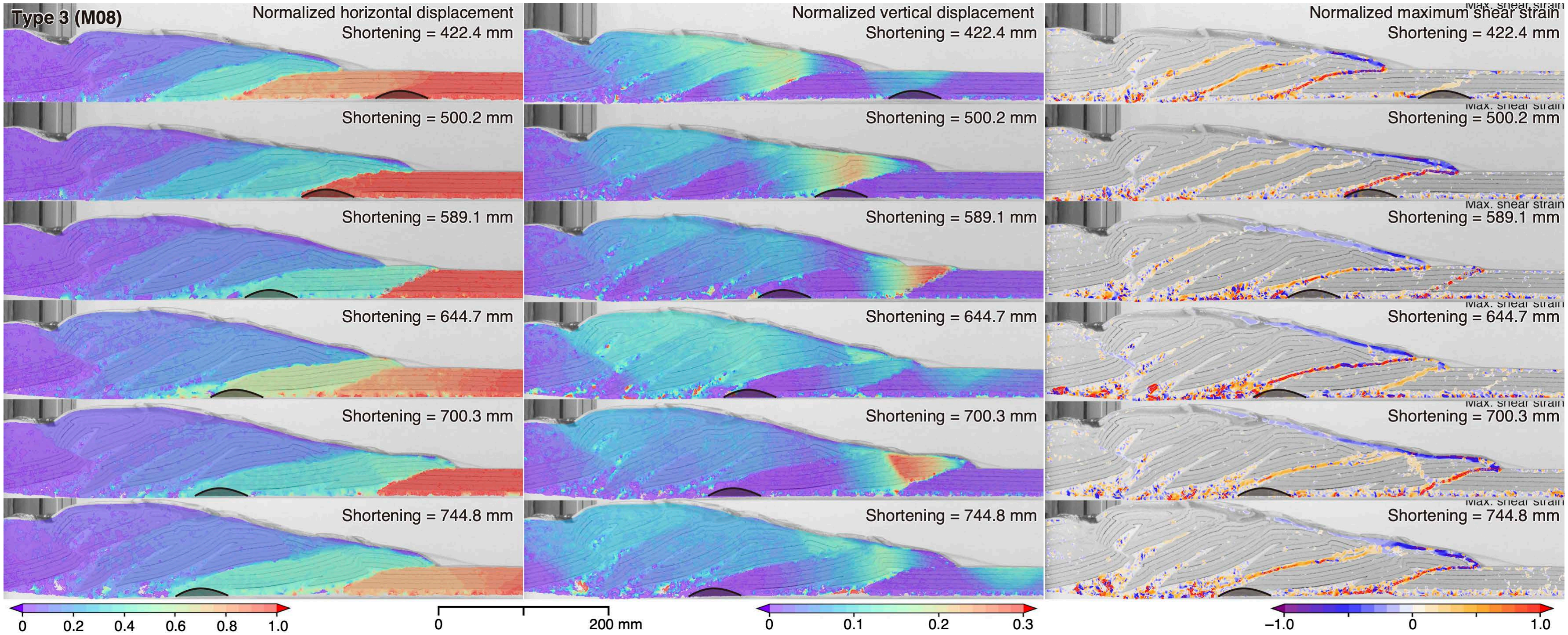

Figure S10. DIC images of the sand mound subduction for the Type 3 model. Interpretations are shown in Figure 8.

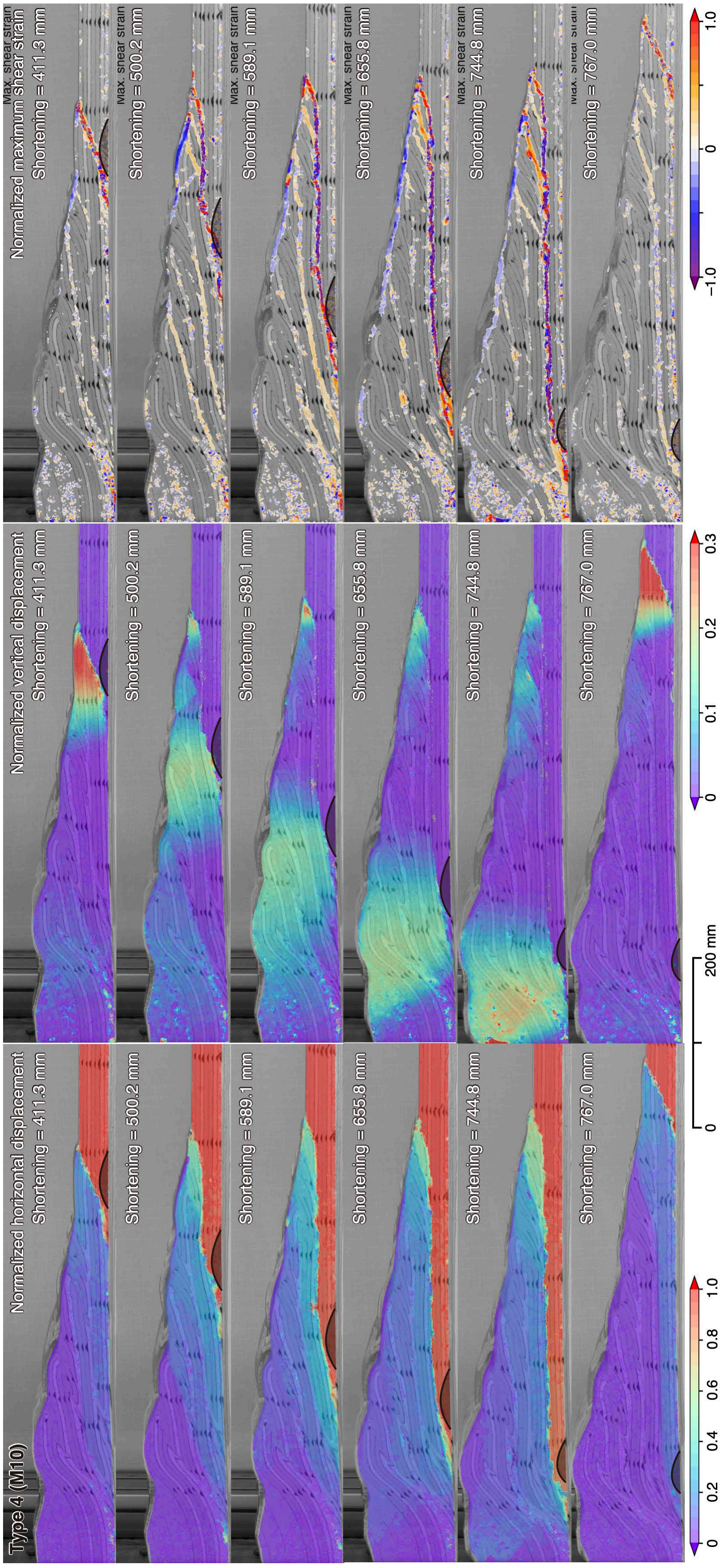

Figure S11. DIC images of the sand mound subduction for the Type 4 model. Interpretations are shown in Figure 8.

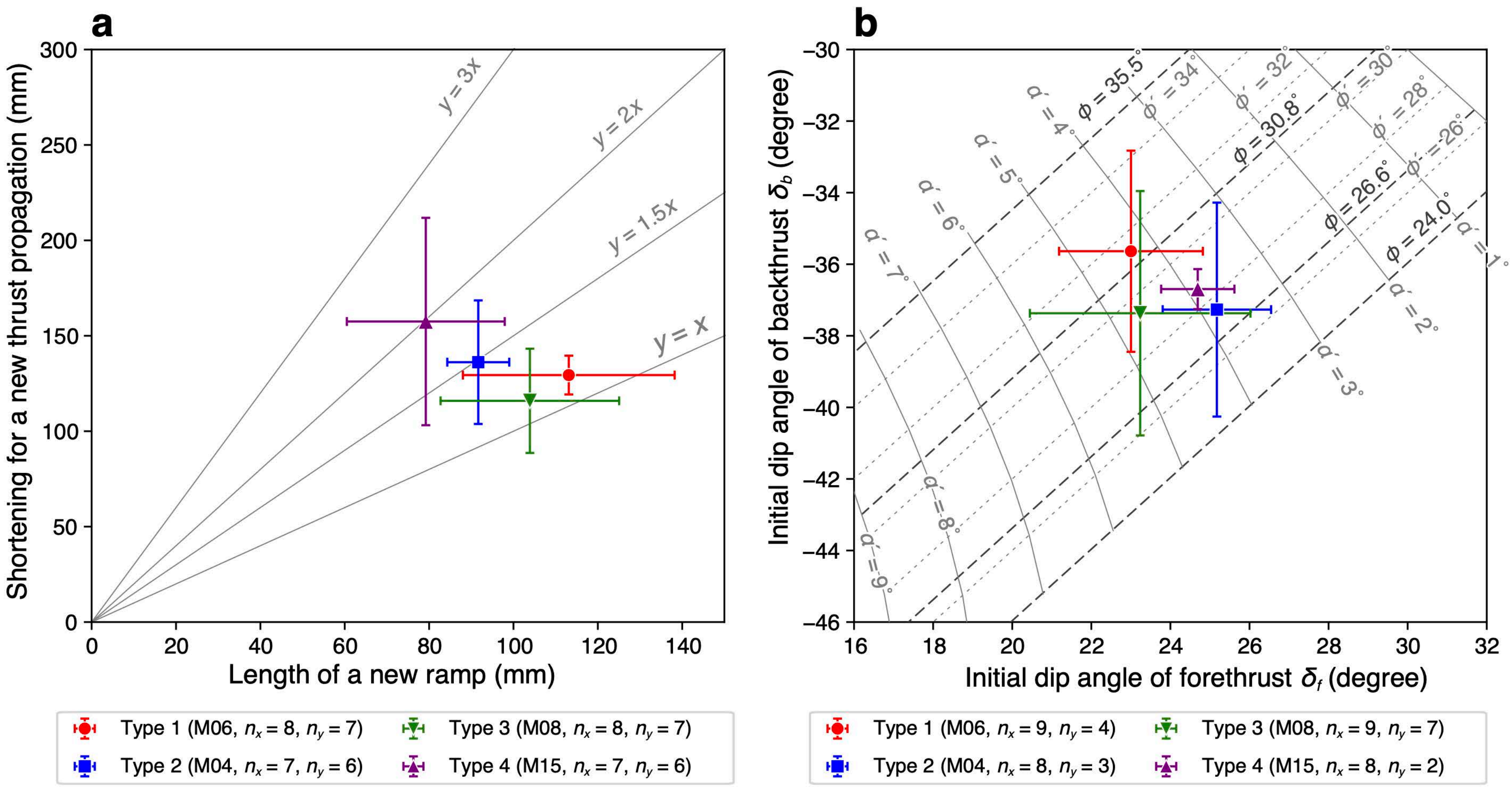

Figure S12. (a) Shortening length required for the propagation of a new deeply rooted frontal forethrust versus the length of a new ramp. (b) Initial dip angles of the forethrust $\delta_{\mathrm{f(init)}}$ and backthrust δ_{b}. Thin gray solid and dotted lines are the effective slope angle α' and the effective internal friction angle ϕ', respectively. Dashed lines (ϕ) indicate the measured friction angles of the sand ($\phi_{\mathrm{dynamic}} = 30.8°$ and $\phi_{\mathrm{peak}} = 35.5°$) and glass microbeads ($\phi_{\mathrm{dynamic}} = 24.0°$ and $\phi_{\mathrm{peak}} = 26.6°$). Results for the other models are shown in Figure S13.

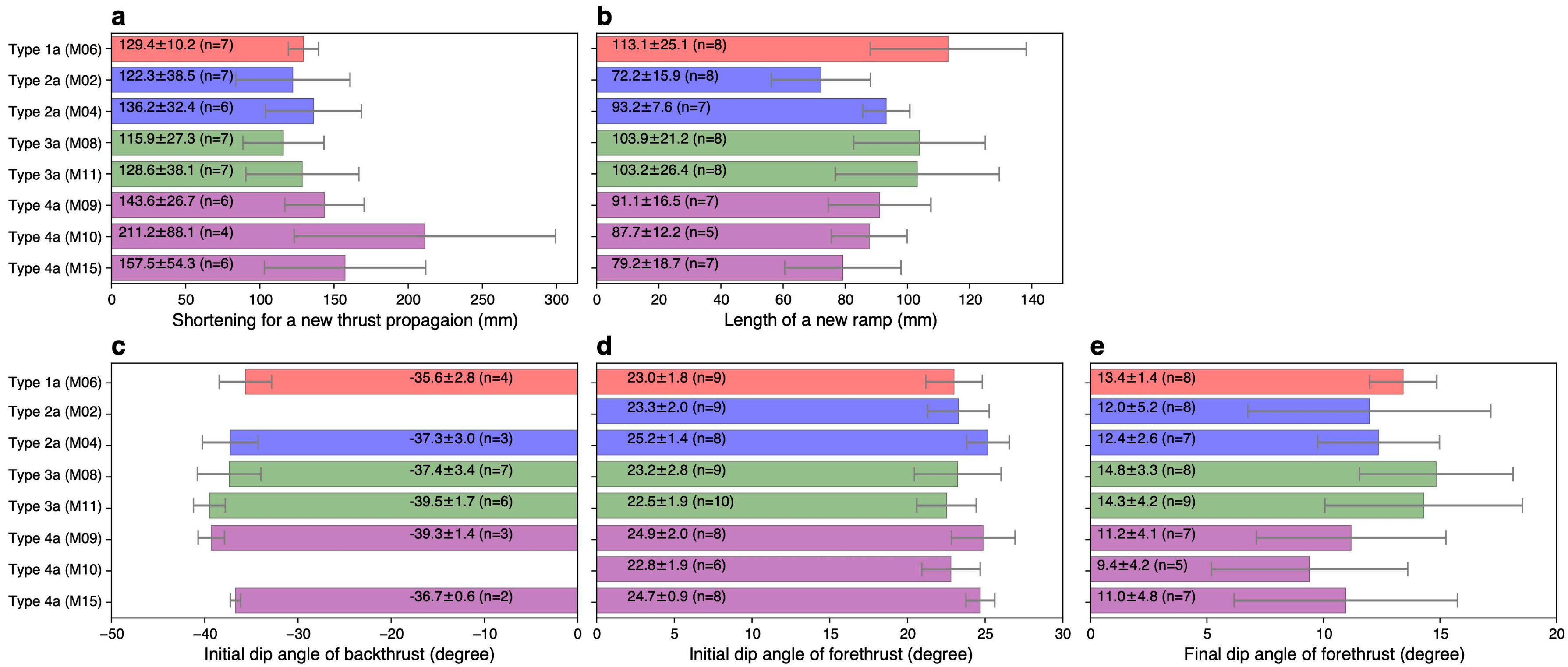

Figure S13. (a) Shortening length for propagation of a new deeply rooted forethrust. (b) Length of a new ramp. (c) Initial dip angles of backthrust δ_{b} when a new frontal forethrust is nucleated. (d) Initial dip angles of a new frontal forethrust $\delta_{\mathrm{f(init)}}$. (e) Dip angles of trailing previous frontal forethrust $\delta_{\mathrm{f(final)}}$ when a new frontal forethrust is nucleated.

Multimedia files

Type_1a_M06.mp4 Images of photos Type 1 (single and continuous model). Model number is M06.

Type_2a_M02.mp4 Images of photos Type 2 (double and continuous model). Model number is M02.

Type_2a_M04.mp4 Images of photos Type 2 (double and continuous model). Model number is M04.

Type_3a_M08.mp4 Images of photos of Type 3 (single and discontinuous model). Model number is M11.

Type_3a_M11.mp4 Images of photos of Type 3 (single and discontinuous model). Model number is M11.

Type_4a_M09.mp4 Images of photos of Type 4 (double and discontinuous model). Model number is M09.

Type_4a_M10.mp4 Images of photos of Type 4 (double and discontinuous model). Model number is M10.

Type_4a_M15.mp4 Images of photos of Type 4 (double and discontinuous model). Model number is M15.

DIC_Type_1a_M06.mp4 Images of results of DIC analysis of Type 1 (single and continuous model). Model number is M06.

DIC_Type_2a_M04.mp4 Images of results of DIC analysis of Type 2 (double and continuous model). Model number is M04.

DIC_Type_3a_M08.mp4 Images of results of DIC analysis of Type 3 (single and discontinuous model). Model number is M08.

DIC_Type_4a_M10.mp4 Images of results of DIC analysis of Type 4 (double and continuous model). Model number is M10.

Figure 01.

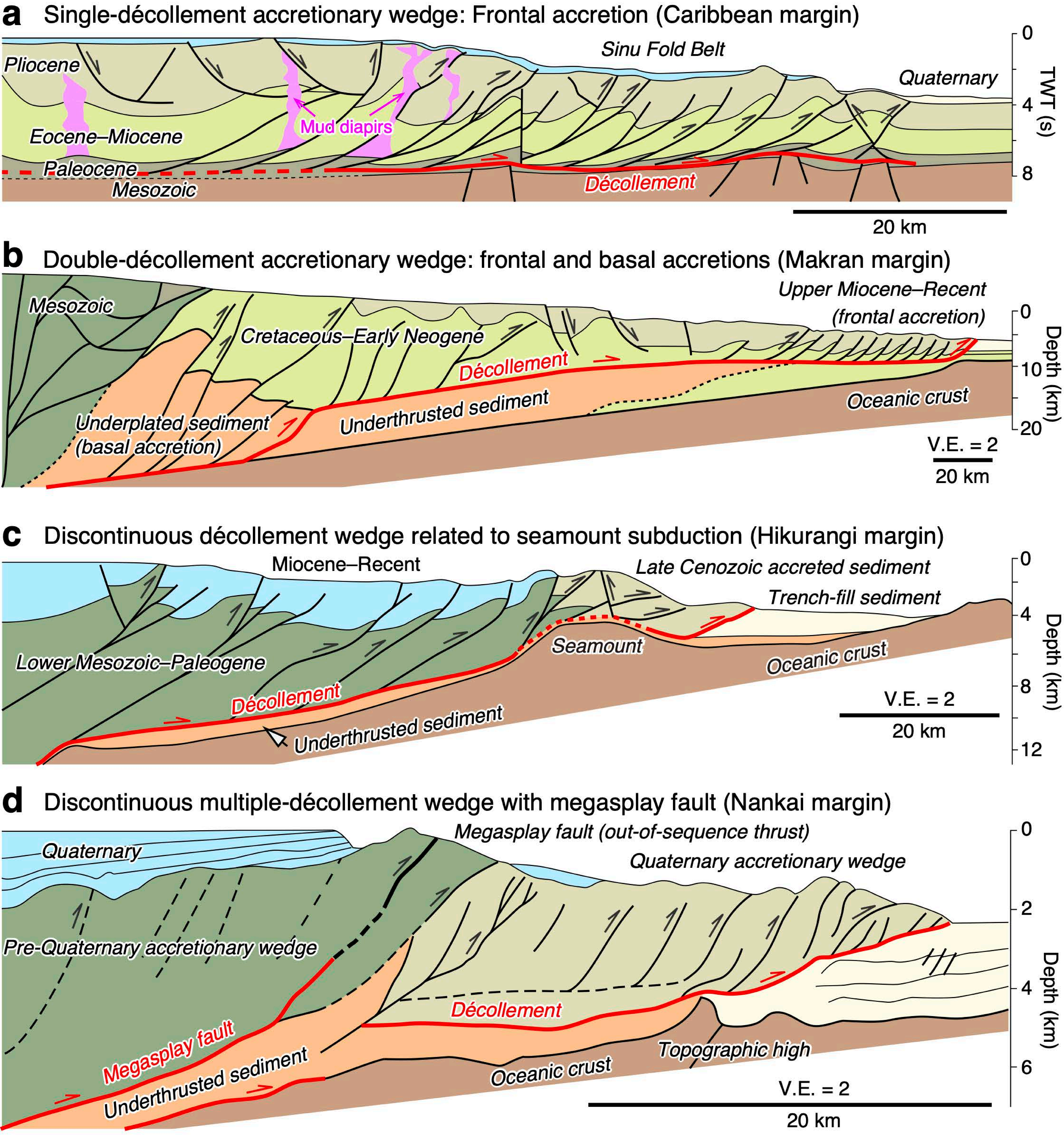
a
Single-décollement accretionary wedge: Frontal accretion (Caribbean margin)
Sinu Fold Belt
Pliocene
Quaternary
Mud diapirs
Eocene–Miocene
Paleocene
Mesozoic
Décollement
TWT (s)
0
4
8
20 km
b
Double-décollement accretionary wedge: frontal and basal accretions (Makran margin)
Upper Miocene–Recent
(frontal accretion)
Mesozoic
Cretaceous–Early Neogene
Décollement
Underthrusted sediment
Underplated sediment
(basal accretion)
Oceanic crust
Depth (km)
0
10
20
V.E. = 2
20 km
c
Discontinuous décollement wedge related to seamount subduction (Hikurangi margin)
Miocene–Recent
Late Cenozoic accreted sediment
Trench-fill sediment
Seamount
Oceanic crust
Lower Mesozoic–Paleogene
Décollement
Underthrusted sediment
Depth (km)
0
4
8
12
V.E. = 2
20 km
d
Discontinuous multiple-décollement wedge with megasplay fault (Nankai margin)
Megasplay fault (out-of-sequence thrust)
Quaternary accretionary wedge
Quaternary
Pre-Quaternary accretionary wedge
Décollement
Megasplay fault
Underthrusted sediment
Oceanic crust
Topographic high
Depth (km)
0
2
4
6
V.E. = 2
20 km

Figure 02.


a
1890 mm
315 mm
Glass sidewall
Direction of shortening
Plastic plate
Pillar
Motor & roller
Plastic sheet
b
~135 mm
Type 1 (M06*)
Proto-wedge
Incoming sediment layer
Sand (GA39)
Glass microbeads
~31˚
25 mm
10 mm
Plastic plate
1890 mm
c
Type 2 (M02, M04*)
Sand (GA39)
Glass microbeads
10 mm
5 mm
10 mm
10 mm
1890 mm
d
Type 3 (M08*, M11)
Sand (GA39)
Glass microbeads
Sand mound
25 mm
10 mm
840 mm
90 mm
960 mm
e
Type 4 (M09, M10*, M15)
Sand (GA39)
Glass microbeads
Sand mound
10 mm
5 mm
10 mm
10 mm
840 mm
90 mm
960 mm

Figure 03.

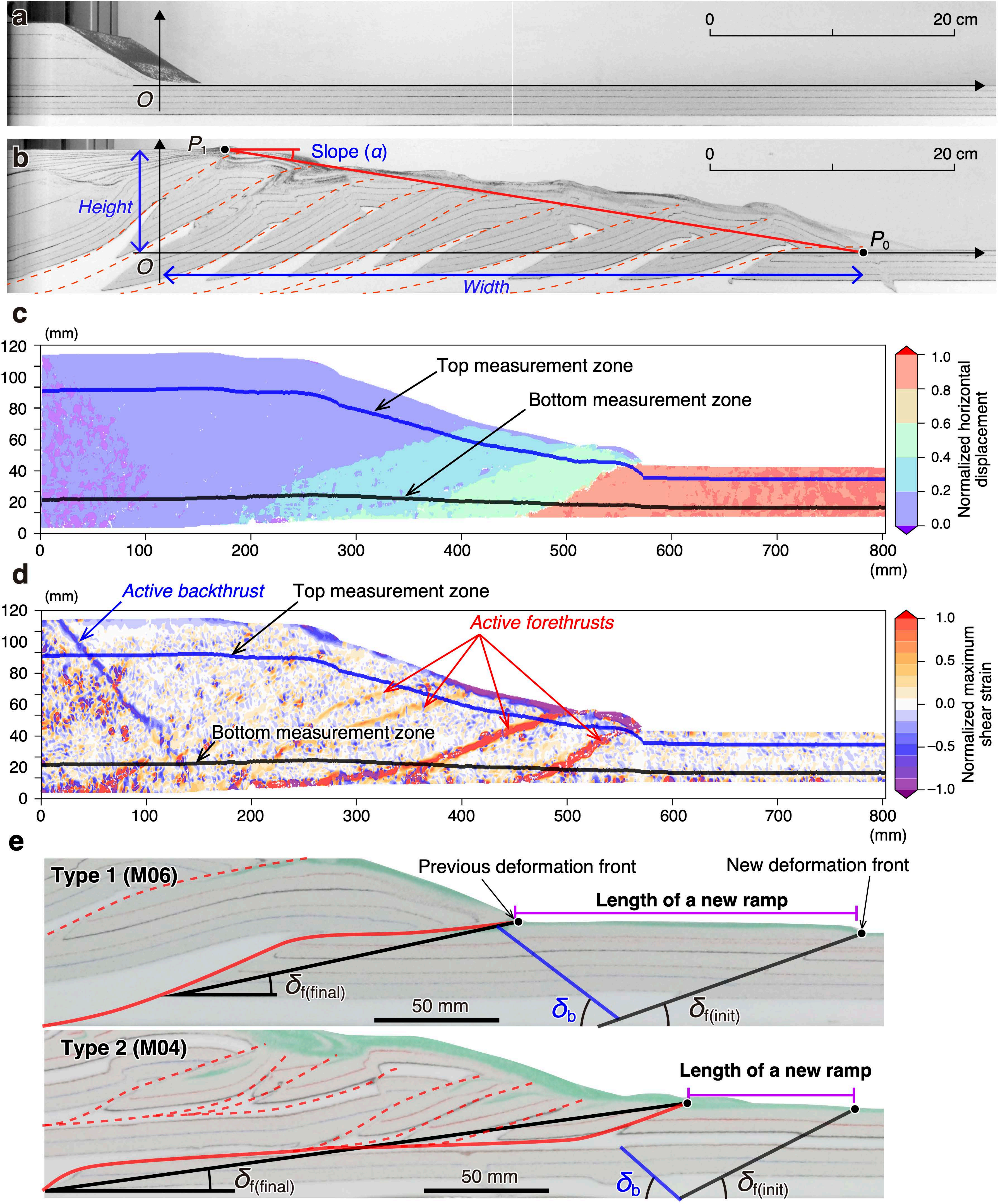
a
O
0
20 cm
b
P1
Slope (α)
0
20 cm
Height
O
P0
Width
c
(mm)
120
100
80
60
40
20
0
0
100
200
300
400
500
600
700
800
(mm)
Top measurement zone
Bottom measurement zone
1.0
0.8
0.6
0.4
0.2
0.0
Normalized horizontal displacement
d
(mm)
Active backthrust
Top measurement zone
Active forethrusts
Bottom measurement zone
120
100
80
60
40
20
0
0
100
200
300
400
500
600
700
800
(mm)
1.0
0.5
0.0
−0.5
−1.0
Normalized maximum shear strain
e
Type 1 (M06)
Previous deformation front
New deformation front
Length of a new ramp
δf(final)
50 mm
δb
δf(init)
Type 2 (M04)
Length of a new ramp
δf(final)
50 mm
δb
δf(init)

Figure 04.


a
Types 1 and 2
Width (mm)
F1 F2 F3 F4 F5 F6 F7 F8 F9
Type 1 (M06)
Type 2 (M04)
Theoretical width
Types 3 and 4
Type 3 (M08)
Type 4 (M10)
Theoretical width
Onset of sand mound subduction
b
Types 1 and 2
Height (mm)
Type 1 (M06)
Type 2 (M04)
Theoretical height
Types 3 and 4
Type 3 (M08)
Type 4 (M10)
Theoretical height
Onset of sand mound subduction
c
Types 1 and 2
Slope α (degree)
Type 1 (M06)
Type 2 (M04)
Critical zone
$y = -0.0022x + 10.7$
$y = -0.0026x + 9.7$
α_{case3}
α_{case2}
α_{case1}
Types 3 and 4
Onset of sand mound subduction
Type 3 (M08)
Type 4 (M10)
Critical zone
Shortening L_s (mm)
0 100 200 300 400 500 600 700 800 900 1000

Figure 05.

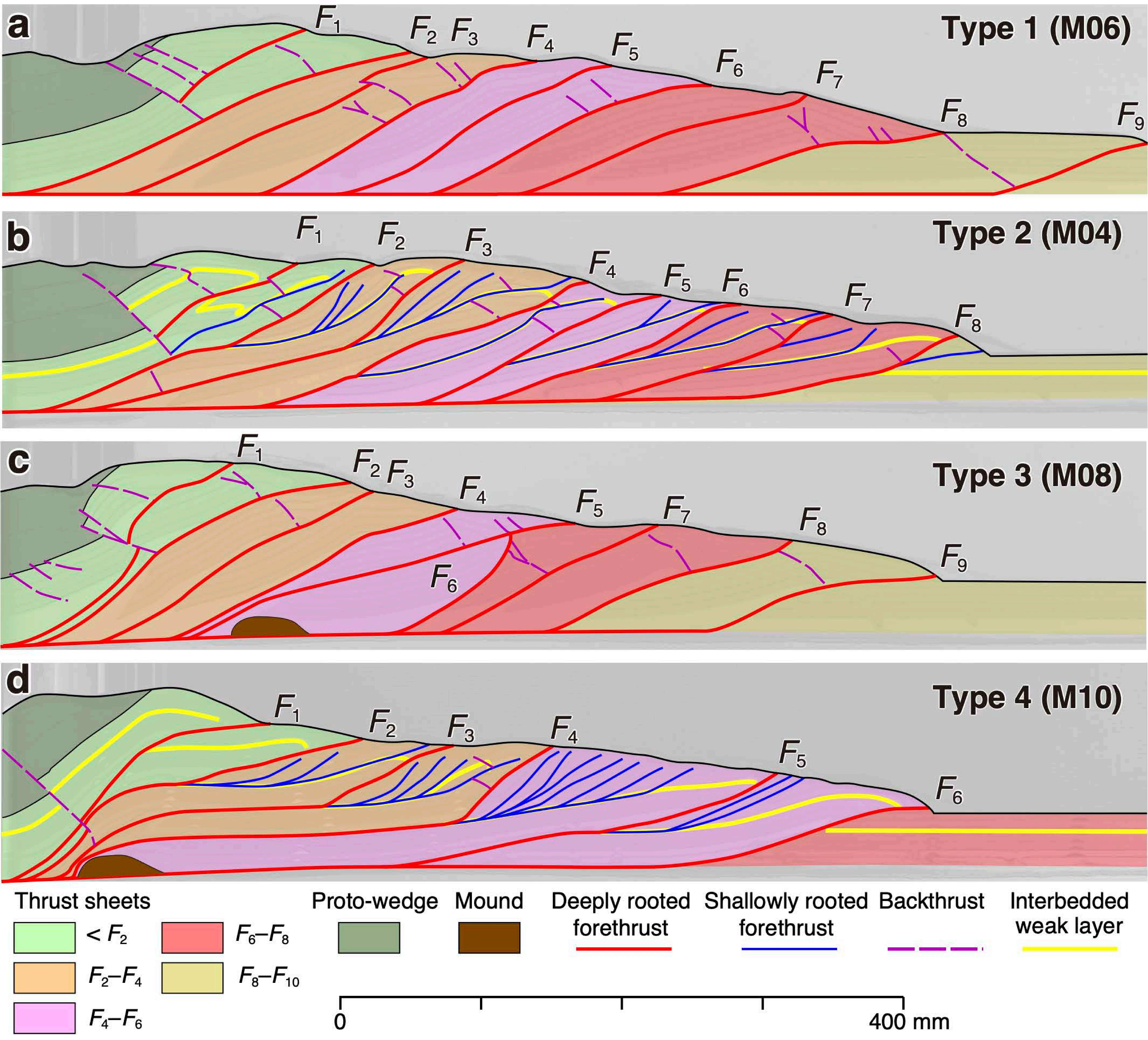
a
Type 1 (M06)
F_1
F_2
F_3
F_4
F_5
F_6
F_7
F_8
F_9
b
Type 2 (M04)
F_1
F_2
F_3
F_4
F_5
F_6
F_7
F_8
c
Type 3 (M08)
F_1
F_2
F_3
F_4
F_5
F_6
F_7
F_8
F_9
d
Type 4 (M10)
F_1
F_2
F_3
F_4
F_5
F_6
Thrust sheets
< F_2
F_2–F_4
F_4–F_6
F_6–F_8
F_8–F_{10}
Proto-wedge
Mound
Deeply rooted forethrust
Shallowly rooted forethrust
Backthrust
Interbedded weak layer
0
400 mm

Figure 06.


a Type 1
Normalized horizontal displacement
Normalized vertical displacement
Shortening = 833.7 mm
Phase 1
Proto-thrust zone
Shortening = 839.3 mm
Phase 2
Shortening = 844.8 mm
Phase 2
Shortening = 889.3 mm
Phase 3
Shortening = 911.5 mm
Phase 4
Shortening = 978.2 mm
Phase 1
Proto-thrust zone
F_4 F_5 F_6 F_7 F_8
400 500 600 700 800
Distance from backstop D_b (mm)
b Type 2
Normalized horizontal displacement
Normalized vertical displacement
Shortening = 667.0 mm
Phase 1
Proto-thrust zone
Shortening = 672.5 mm
Phase 2
Shortening = 678.1 mm
Phase 2
Shortening = 722.5 mm
Phase 3
Shortening = 744.8 mm
Phase 4
Shortening = 778.1 mm
Phase 1
Proto-thrust zone
F_3 F_{3d} F_4 F_{4a} F_5 F_{5a} F_{5b} F_6 F_{6a}
300 400 500 600
Distance from backstop D_b (mm)
0 0.2 0.4 0.6 0.8 1.0
0 0.1 0.2 0.3
Active deeply rooted forethrust
Active shallowly rooted forethrust
Inactive forethrust
Active backthrust
Inactive backthrust

Figure 07.

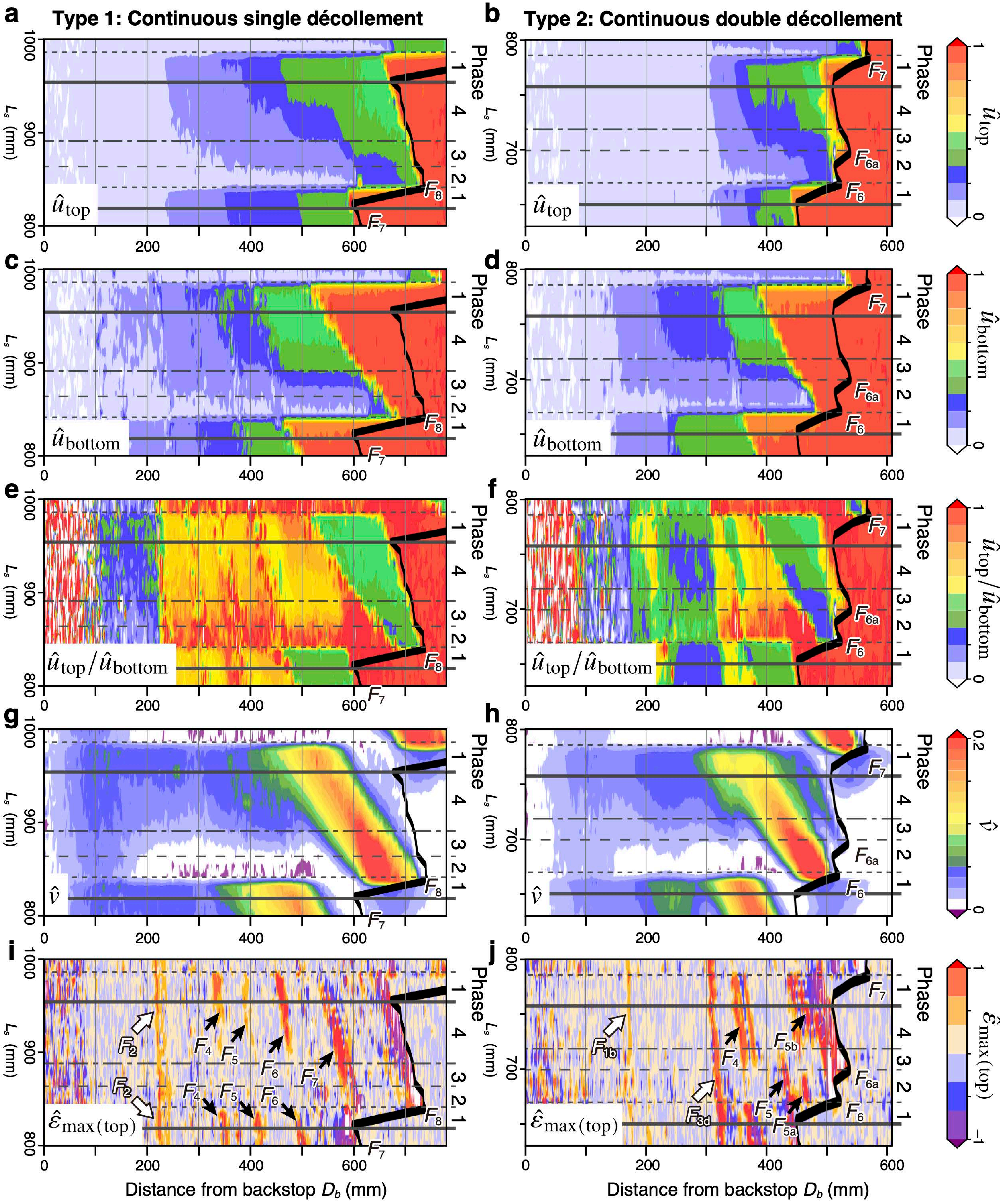
a
Type 1: Continuous single décollement
b
Type 2: Continuous double décollement
L_s (mm)
Phase
1
4
3
2
1
$\hat{u}_{\text{top}}$
$\hat{u}_{\text{bottom}}$
$\hat{u}_{\text{top}}/\hat{u}_{\text{bottom}}$
$\hat{v}$
$\hat{\varepsilon}_{\max(\text{top})}$
c
d
e
f
g
h
i
j
F_7
F_8
F_6
F_{6a}
F_2
F_4
F_5
F_{1b}
F_{3d}
F_{5a}
F_{5b}
1000
900
800
700
0
200
400
600
0
1
0.2
−1
Distance from backstop D_b (mm)

Figure 08.


a
Type 3 (M08)
Normalized horizontal displacement
Normalized vertical displacement
Shortening = 422.4 mm
Phase 2 (F_5)
F_2 F_3 F_4 F_5
Sand mound
Shortening = 500.2 mm
Phase 3 (F_5)
Shortening = 589.1 mm
Phase 2 (F_6)
F_6
Shortening = 644.7 mm
Phase 1 (F_7)
Shortening = 700.3 mm
Phase 2 (F_7)
F_7
Shortening = 744.8 mm
Phase 1 (F_8)
D_b = 100
200
300
400
500
600 mm
b
Type 4 (M10)
Shortening = 411.3 mm
Phase 2 (F_4)
F_2 F_{2c} F_3 F_4
Sand mound
Shortening = 500.2 mm
Phase 3 (F_4)
F_{3c} F_{4a} F_{4b}
Shortening = 589.1 mm
Phase 3 (F_4)
F_{3d} F_{4c} F_{4d}
Shortening = 655.8 mm
Phase 3 (F_4)
F_{4e}
Shortening = 744.8 mm
Phase 4 (F_4)
F_{4f} F_{4g}
Shortening = 767.0 mm
Phase 2 (F_5)
F_5
0
0.2
0.4
0.6
0.8
1.0
0
0.1
0.2
0.3
Active deeply rooted forethrust
Active shallowly rooted forethrust
Active backthrust
Inactive forethrust

Figure 09.

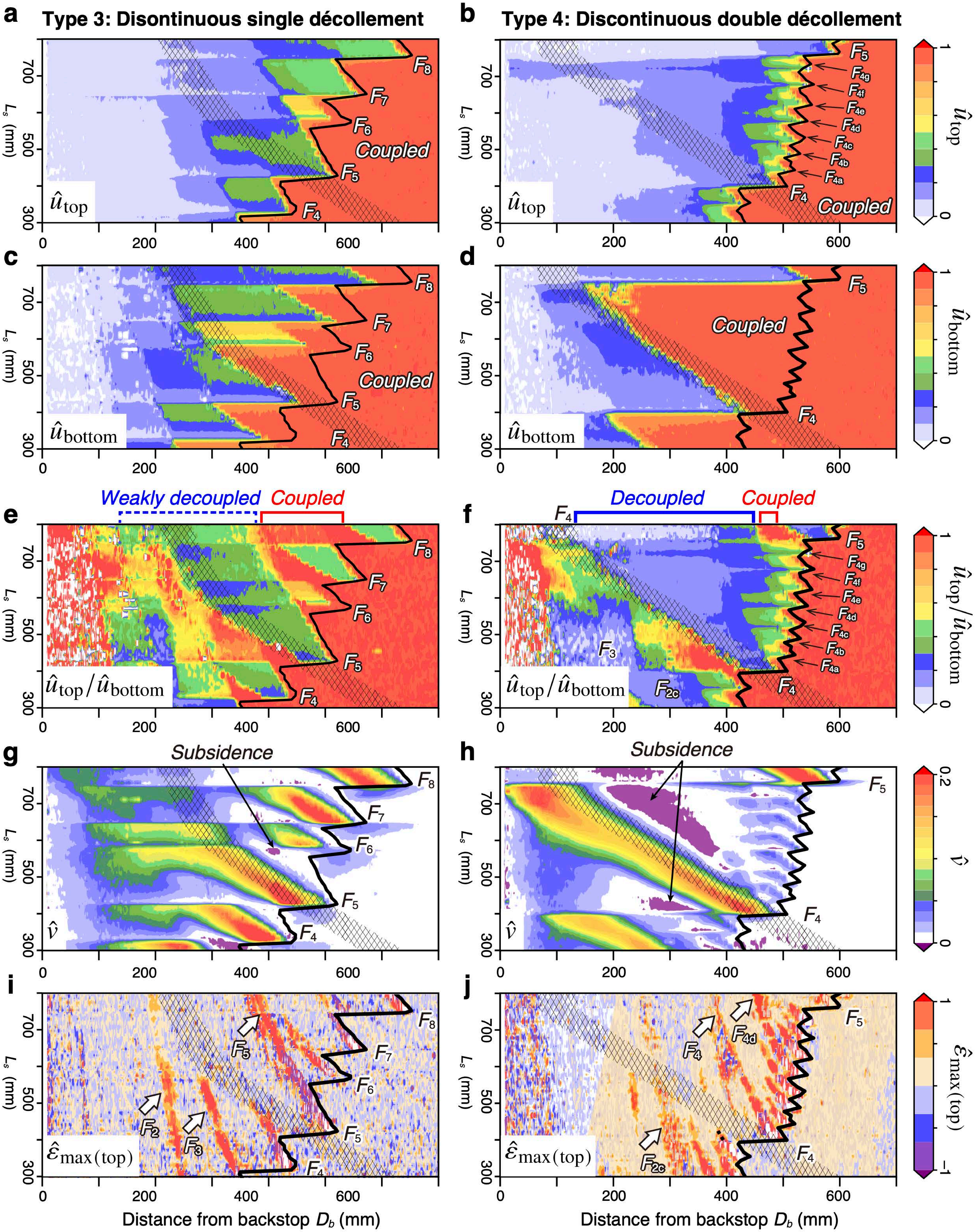
a
Type 3: Discontinuous single décollement
b
Type 4: Discontinuous double décollement
$\hat{u}_{\mathrm{top}}$
Coupled
F_4
F_5
F_6
F_7
F_8
F_{4a}
F_{4b}
F_{4c}
F_{4d}
F_{4e}
F_{4f}
F_{4g}
c
d
$\hat{u}_{\mathrm{bottom}}$
e
f
Weakly decoupled
Decoupled
$\hat{u}_{\mathrm{top}}/\hat{u}_{\mathrm{bottom}}$
F_3
F_{2c}
g
h
Subsidence
$\hat{v}$
i
j
$\hat{\varepsilon}_{\max(\mathrm{top})}$
F_2
F_{2c}
L_s (mm)
300
500
700
0
200
400
600
1
0.2
-1
Distance from backstop D_b (mm)

Figure 10.

Decoupled part
Coupled part
a
Phase 4/1
Inner part
F_1
F_2
Outer part (proto-thrust zone)
$\alpha_{in} \rightarrow \alpha_{\phi_{dynamic}}$
$\phi'_{in} \rightarrow \phi_{peak}$
$\phi'_{out} \rightarrow \phi_{peak}$
Weakly coupled
Partially coupled
Coupled
b
Phase 2
$\alpha_{in} \rightarrow \alpha_{\phi_{peak}}$
0
Basal coupling ratio
1
F_1
F_2
$\alpha_{in} = \alpha_{\phi_{dynamic}}$
α'_{out}
$\phi'_{in} = \phi_{peak}$
$\phi'_{out} = \phi_{peak}$
δ_b
δ_f
Decoupled
Coupled
c
Phase 2
$\alpha_{in} \rightarrow \alpha_{\phi_{peak}}$
F_1
F_2
$\alpha_{in} = \alpha_{\phi_{dynamic}}$
α'_{out}
$\phi'_{in} < \phi_{peak}$
$\phi'_{out} \rightarrow \phi_{dynamic}$
Decoupled
Weakly coupled
Coupled
d
Phase 3
$\alpha_{in} \rightarrow \alpha_{\phi_{dynamic}}$
F_1
F_2
F_3
α'_{out}
$\phi'_{out} \rightarrow \phi_{dynamic}$
$\phi'_{in} \rightarrow \phi_{reactivation}$
Weakly coupled
Partially coupled
Coupled
e
Phase 4
$\alpha_{in} \rightarrow \alpha_{\phi_{dynamic}}$
F_1
F_2
F_3
$\phi'_{out} = \phi_{dynamic}$
$\phi_{in} \rightarrow \phi_{dynamic}$
Weakly coupled
Partially coupled
Coupled
f
Phase 1
$\alpha \approx \alpha_{\phi_{dynamic}}$
Inner part
F_1
F_2
F_3
Outer part
$\phi'_{out} \rightarrow \phi_{peak}$
$\phi'_{in} \rightarrow \phi_{peak}$
Weakly coupledv
Partially coupled
Coupled

Figure 11.


a
α_{in} (Phase 1–3)
Inner part
ψ_0
H_{in}
ϕ'_{in}
x
α_{in} (Phase 0–1)
z
σ_z
σ_x
τ_{xz}
H_{out}
α'_{out}
ϕ'_{out}
Outer part
H_0
σ_3
τ_b
σ_1
ψ_b
σ_1
σ_3
τ_b
δ_b
δ_f
σ_n
L_{in}
L_{out}
σ_n
Assumption
b
Inner part
Outer part
Friction angle (ϕ'_{in})
Friction angle (ϕ'_{out})
ϕ_{peak}
$\phi_{dynamic}$
36
34
32
30
Phase 1
2
3
4
c
$\alpha_{\phi dynamic}$
$\alpha_{\phi peak}$
Slope (α_{in})
Slope (α'_{out})
α'_{out}
α_{out}
10
8
6
4
2
0
0
20
40
60
80
100
Shortening (mm)
Calculation
d
Inner part
Outer part
L_{in} + L_{out} (mm)
750
700
650
600
550
500
H_{in} (mm)
150
140
130
120
L_{out} (mm)
150
100
50
H_{out} (mm)
60
55
50
45
40
e
Differential stress (Pa)
2800
2400
2000
1600
Basal shear stress (Pa)
1000
950
900
850
800
Differential stress (Pa)
900
800
700
600
500
Basal shear stress (Pa)
350
300
250
200
f
Wedge strength W_s
2.8
2.6
2.4
2.2
2.0
Detachment strength F_s
0.50
0.48
0.46
0.44
Shortening (mm)

Figure 12.

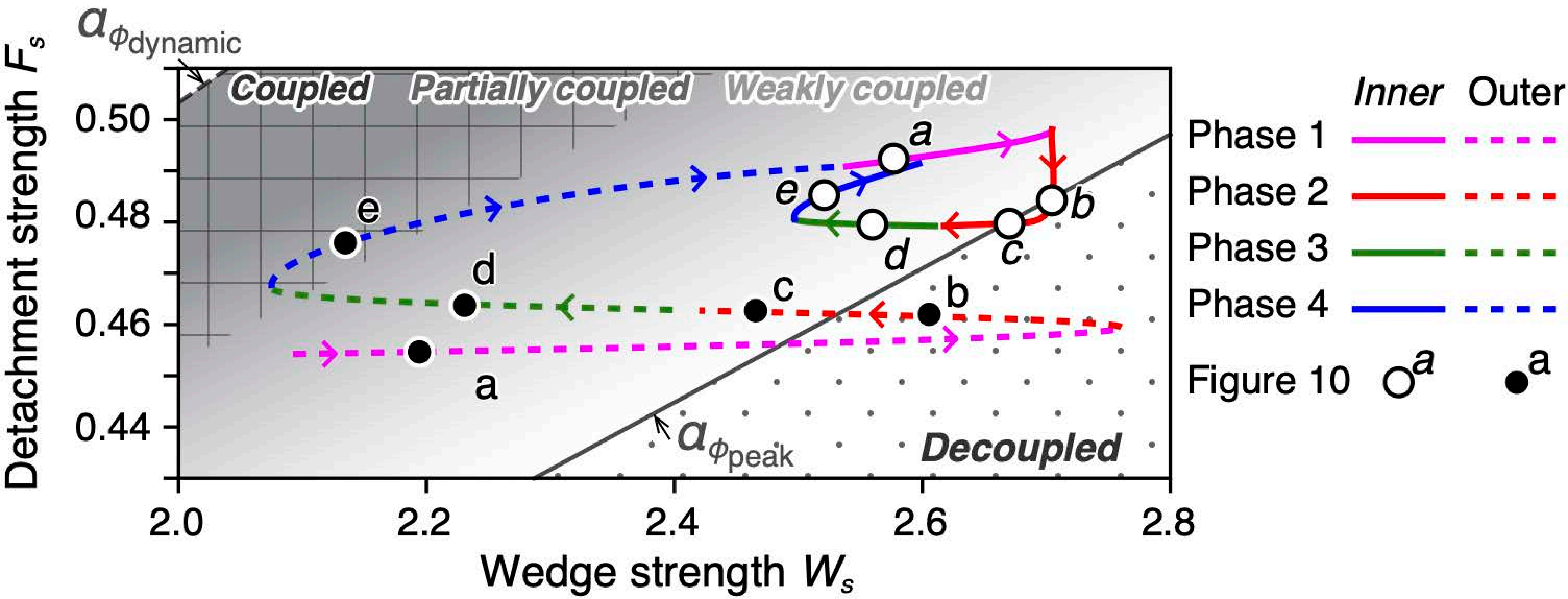
$a_{\phi_{\text{dynamic}}}$
Coupled
Partially coupled
Weakly coupled
Decoupled
$a_{\phi_{\text{peak}}}$
Detachment strength F_s
Wedge strength W_s
0.44
0.46
0.48
0.50
2.0
2.2
2.4
2.6
2.8
a
b
c
d
e
Inner
Outer
Phase 1
Phase 2
Phase 3
Phase 4
Figure 10

Figure 13.

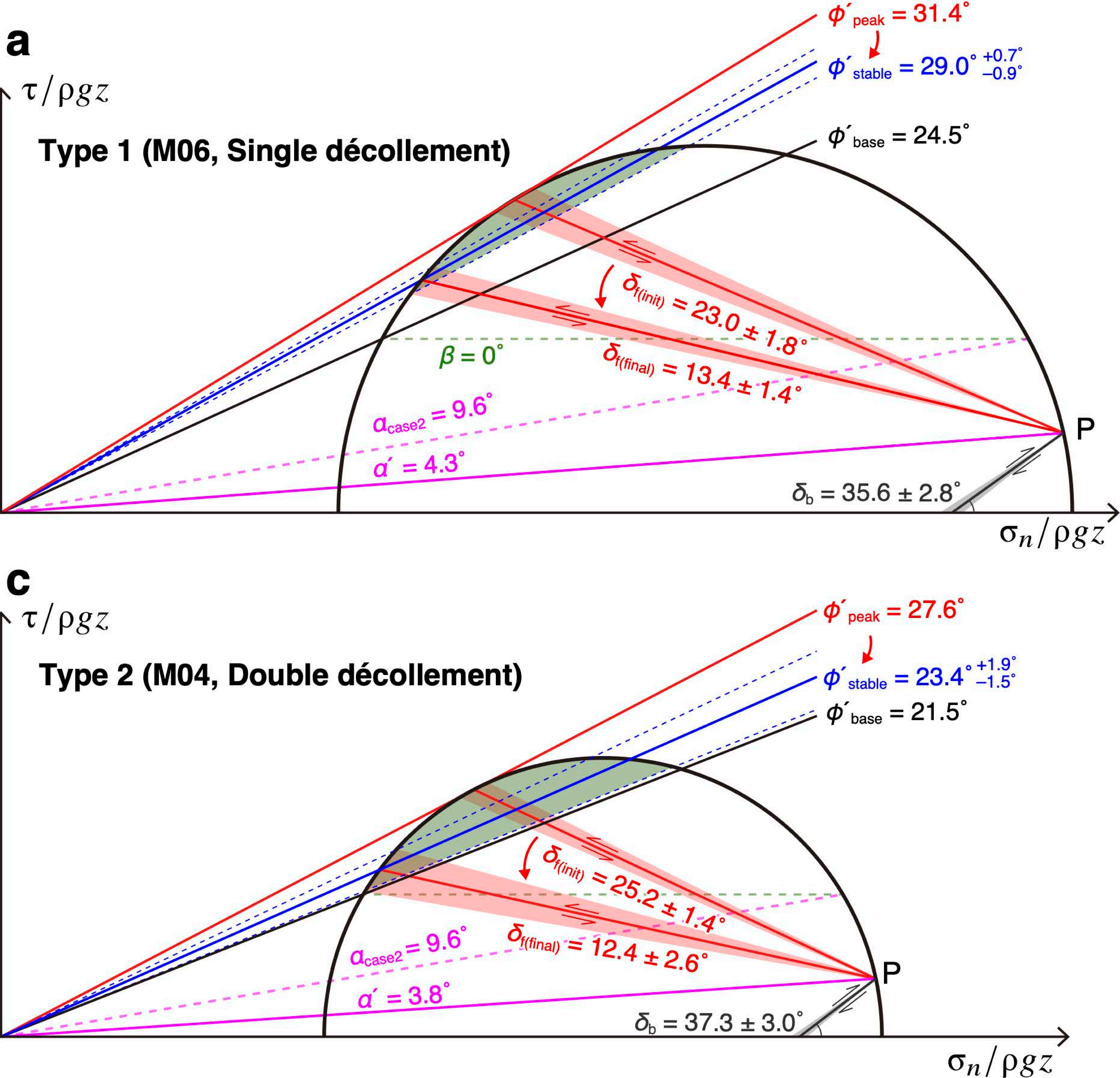
a
τ/ρgz
Type 1 (M06, Single décollement)
φ´peak = 31.4°
φ´stable = 29.0° +0.7° −0.9°
φ´base = 24.5°
δf(init) = 23.0 ± 1.8°
β = 0°
δf(final) = 13.4 ± 1.4°
αcase2 = 9.6°
α´ = 4.3°
P
δb = 35.6 ± 2.8°
σn/ρgz
c
τ/ρgz
Type 2 (M04, Double décollement)
φ´peak = 27.6°
φ´stable = 23.4° +1.9° −1.5°
φ´base = 21.5°
δf(init) = 25.2 ± 1.4°
δf(final) = 12.4 ± 2.6°
αcase2 = 9.6°
α´ = 3.8°
P
δb = 37.3 ± 3.0°
σn/ρgz

Figure 14.

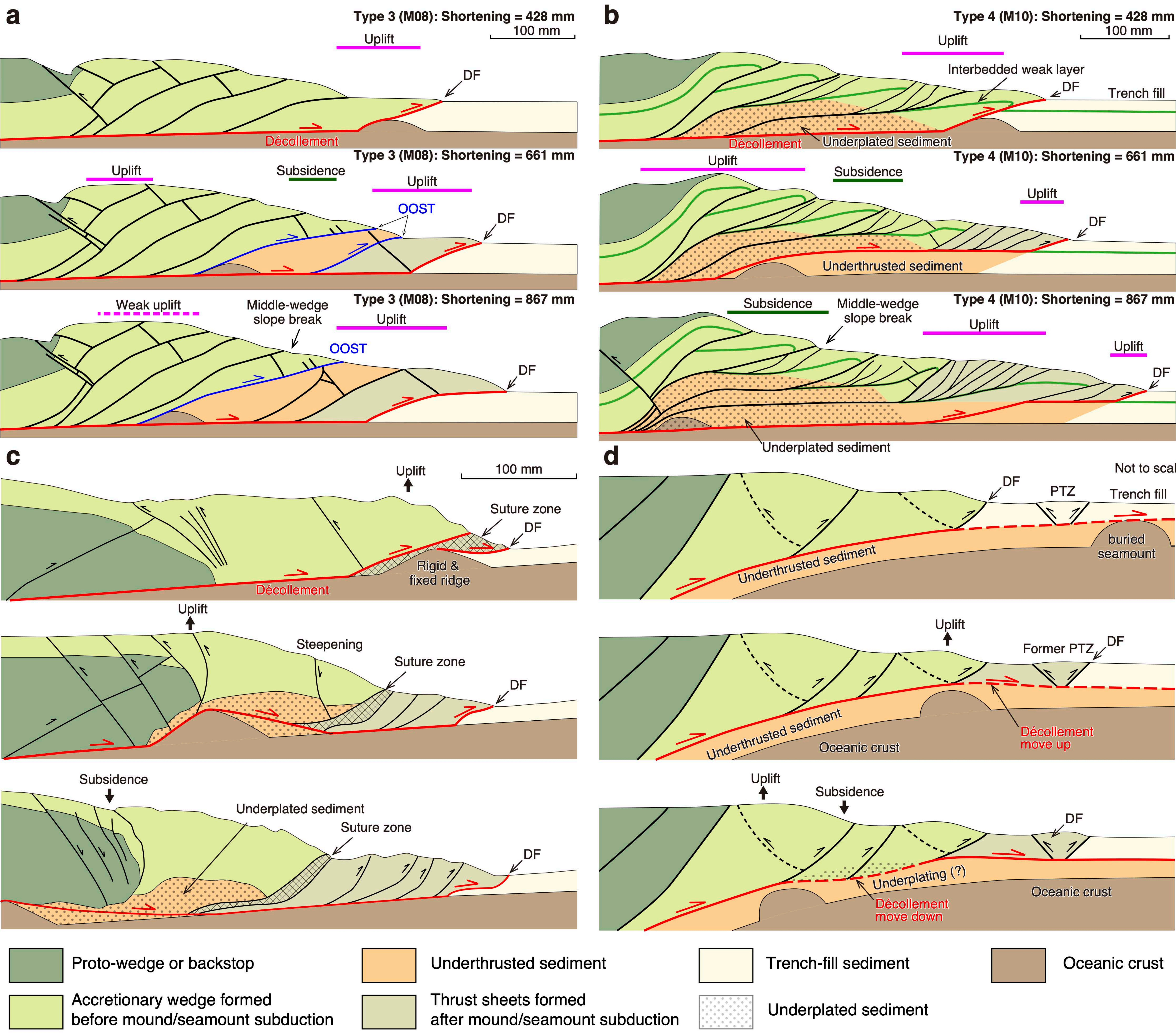
a
Type 3 (M08): Shortening = 428 mm
100 mm
Uplift
DF
Décollement
Type 3 (M08): Shortening = 661 mm
Uplift
Subsidence
Uplift
OOST
DF
Type 3 (M08): Shortening = 867 mm
Weak uplift
Middle-wedge slope break
Uplift
OOST
DF
b
Type 4 (M10): Shortening = 428 mm
100 mm
Uplift
Interbedded weak layer
DF
Trench fill
Décollement
Underplated sediment
Type 4 (M10): Shortening = 661 mm
Uplift
Subsidence
Uplift
DF
Underthrusted sediment
Type 4 (M10): Shortening = 867 mm
Subsidence
Middle-wedge slope break
Uplift
Uplift
DF
Underplated sediment
c
Uplift
100 mm
Suture zone
DF
Rigid & fixed ridge
Décollement
Uplift
Steepening
Suture zone
DF
Subsidence
Underplated sediment
Suture zone
DF
d
Not to scal
DF
PTZ
Trench fill
buried seamount
Underthrusted sediment
Uplift
Former PTZ
DF
Underthrusted sediment
Oceanic crust
Décollement move up
Uplift
Subsidence
DF
Underplating (?)
Décollement move down
Oceanic crust
Proto-wedge or backstop
Accretionary wedge formed before mound/seamount subduction
Underthrusted sediment
Thrust sheets formed after mound/seamount subduction
Trench-fill sediment
Underplated sediment
Oceanic crust